SISSA **ISAS**

SCUOLA INTERNAZIONALE SUPERIORE DI STUDI AVANZATI
INTERNATIONAL SCHOOL FOR ADVANCED STUDIES

Stellar archeology: from first stars to dwarf galaxies

Thesis submitted for the degree of
Doctor Philosophiæ

CANDIDATE
Stefania Salvadori

SUPERVISOR
Prof. Andrea Ferrara

October 2009

Alla nonna Francesca

Contents

0.1 List of acronyms v

1 The first galaxies 1

1.1 Structure formation 3
  1.1.1 Linear regime 3
  1.1.2 Non-linear regime: dark matter haloes 5
  1.1.3 Non-linear regime: protogalaxies formation 8
1.2 Star formation and evolution 9
  1.2.1 Characteristic masses 9
  1.2.2 The final fate 10
1.3 Feedback processes 12
  1.3.1 Radiative feedback 13
  1.3.2 Mechanical feedback 14
  1.3.3 Chemical feedback 15
1.4 Cosmic relics & feedback survivors 16
1.5 Observational imprints in the Milky Way 17
  1.5.1 Galactic halo stars 18
  1.5.2 Dwarf spheroidal galaxies 23
1.6 Thesis purpose and plan 29

2 Modeling the MW formation 31

2.1 Building the merger tree 31
  2.1.1 The N-body simulation 31
  2.1.2 The semi-analytical model 34
2.2 Including baryons 38
  2.2.1 The mass of star-forming haloes 39
  2.2.2 Star formation efficiency 39
  2.2.3 The Initial Mass Function 40
  2.2.4 Instantaneous Recycling Approximation 40
  2.2.5 Nucleosynthetic products 41
  2.2.6 Mechanical Feedback 42
  2.2.7 Metal mixing 43
2.3 Model calibration 44

2.3.1 Close-box vs feedback models 45
2.3.2 Accretion vs Self-Enrichment 47
2.4 The Milky Way environment 50
2.4.1 Metallicity evolution 50
2.4.2 Mass ejection from progenitor haloes 52

3 Stellar relics in the Galactic halo 55
3.1 The Metallicity Distribution Function 56
3.2 Changing the critical metallicity 56
3.3 The lack of $Z = 0$ stars: implications 59
3.4 Second generation stars 59
3.5 Varying the Pop III mass 61
3.6 Summary and discussion 62

4 Searching for metal-poor stars 67
4.1 Model improvements 68
4.2 Testing the model 69
4.2.1 The Age-Metallicity relation 69
4.2.2 The Metallicity Distribution Function 71
4.3 The spatial distribution of metal-poor stars 72
4.4 Discussion 76

5 The puzzling ^{6}Li plateau 79
5.1 Modeling the ^{6}Li production by cosmic rays 80
5.1.1 Star formation rate 80
5.1.2 Lithium production 82
5.2 The ^{6}Li evolution 84
5.3 ^{6}Li abundance in metal-poor halo stars 86
5.4 Summary and discussion 86

6 Feedback imprints in dSphs 89
6.1 New Features of the model 90
6.1.1 Model parameters 92
6.2 Life and times of dSphs 92
6.2.1 The birth environment 93
6.2.2 Feedback regulated evolution 95
6.2.3 Beyond blow-away 96
6.3 Observable properties 97
6.3.1 Metallicity Distribution Function 99
6.3.2 Color-Magnitude Diagram 101
6.3.3 Keys abundance ratios 102
6.3.4 Dark Matter content 104
6.3.5 Gas footprints of feedback 105

6.4 Summary and discussion . . . 106

7 Ultra faint dwarfs **111**
7.1 Including minihaloes . . . 112
7.2 The Fe-Luminosity relation . . . 114
7.3 Metallicity Distribution Functions . . . 115
  7.3.1 Classical vs ultra faint dwarfs . . . 115
  7.3.2 The Ultra Faint candidates . . . 116
7.4 The star formation efficiency . . . 117
7.5 Summary and discussion . . . 120

8 Conclusions **123**

0.1 List of acronyms

Several acronyms will be used in this Thesis. In order to facilitate the reading we provide their complete list in the following.

acronym	**extended name**
AGB	Asymptotic Giant Branch
BBN	Big Bang Nucleosynthesis
BHB	Blue Horizontal Branch
BHs	Black Holes
CDM	Cold Dark Matter
CMB	Cosmic Microwave Background
CMD	Color-Magnitude Diagram
CRs	Cosmic Rays
DM	Dark Matter
dSphs	Dwarf Spheroidal Galaxies
EMP	Extremely Metal-Poor stars: $[\mathrm{Fe/H}] < -3$
EPS	Extended Press & Schechter
GAMETE	GAlaxy MErger Tree & Evolution
GM	Galactic Medium
HMP	Hyper Metal-Poor stars: $[\mathrm{Fe/H}] < -5$
IMF	Initial Mass Function
ISM	Interstellar Medium
IGM	Intergalactic Medium

acronym	**extended name**
IRA	Instantaneous Recycling Approximation
LW	Lyman-Werner
MDF	Metallicity Distribution Function
MP	Metal-Poor stars: $[\mathrm{Fe/H}] < -1$
MW	Milky Way
Pop III	Population III
Pop II/I	Population II/I
RGB	Red Giant Branch
RHB	Red Horizontal Branch
SDSS	Sloan Digital Sky Survey
SFH	Star Formation History
SFR	Star Formation Rate
SN	Supernova
SNR	Supernova Rate
UFs	Ultra-Faint Dwarf Galaxies
UMP	Ultra Metal-Poor stars: $[\mathrm{Fe/H}] < -4$
VMP	Very Metal-Poor stars: $[\mathrm{Fe/H}] < -2$
2G	Second Generation

Chapter 1

The first galaxies

The formation of the first stars within the early protogalaxies marks a fundamental stage on the evolution of the Universe, driving its transition from a simple, early state, to the very complex one we can observe today. According to the fundamental theory for our present understanding of cosmology, the Standard Hot Big Bang Model, the Universe was homogeneous, neutral, and metal-free before the first stellar sources were born. Starting from a discontinuity of virtual infinite density and temperature, the Universe was expanding at the Hubble rate for ~ 13.7 billion years, gradually cooling down its temperature as a result of the expansion. During the early evolutionary stages the radiation was dominating and the matter was thermally coupled to this component through Compton scattering and free-free interactions. At that time the temperature decreased as $T \propto (1+z)$; depending on T the early Universe was populated by different kind of elementary particles, and dominated by different physical processes.

When $T \approx 10^9$K (three minutes after the Big Bang) nuclear reactions occur and light nuclei are synthesized through strong interactions of neutrons and protons. In spite of the higher temperature of the Universe with respect to the stellar interiors ($T_* \approx 1.55 \times 10^7$ K), by the time helium synthesis is accomplished the density and temperature of the Universe is too low for significant production of heavier nuclei to proceed, and only a small fraction of ^{7}Li and ^{7}Be is synthesized (Peacock 1993). The predicted relative abundance of these primordial elements is a function of the single parameter η *i.e.* the baryon-to-photon ratio. Once η is fixed through WMAP3 observations, the standard theory simultaneously accounts for the abundances of deuterium ^{2}D/H$= 2.75 \times 10^{-5}$, tritium ^{3}He/H$= 9.28 \times 10^{-6}$, helium $\mathrm{Y}_p = 0.2484$ observed in “unprocessed” regions.

The transition from radiation to matter domination occurs when $T \approx 10^4$ K; however, the Universe remains hot enough that the gas is ionized and Compton scattering effectively couple matter and radiation. At lower temperatures instead, $T \approx 10^3$ K, protons and electrons start to combine to form neutral hydrogen, and finally photons decouple from matter. The Cosmic Microwave Background (CMB) radiation, incidentally detected by Penzias & Wilson in 1965, is the redshifted fossil radiation from these early times, originated from the "last scattering surface" among photons and matter, occurred at redshift $z \approx 1100$. Its almost isotropic black body spectrum $T_{CMB} = 2.726 \pm 0.01$ K, with temperature anisotropies $\Delta T_{CMB}/T_{CMB} \approx 10^{-5}$ indicates that the Universe was extremely uniform at that time, with spatial perturbations in the energy density and gravitational potential of roughly one part in 10^5. Such a perturbations are directly related to the quantistic density fluctuations originated in the very early Universe, and amplified during the inflation epoch.

After recombination we have a picture of the Universe composed by fully neutral hydrogen and helium, with a residual fraction of free electrons equal to $x_e \approx 10^{-4}$. The matter density is roughly homogeneous, and pervaded by small density perturbations. Gravitational instability allows the gradual growing of these fluctuations, leading to the formation of a filamentary web-like structure. First stars will predominantly originate within the intersection regions of these filaments, probably when $z \approx 20 - 30$.

The birth of the first proto-galaxies dramatically changes this initially simple physical conditions through a series of different *feedback processes*: ionizing photons from the first stars start to reionize and reheat the intergalactic medium (IGM); heavy elements are synthesized inside the first stellar generations and during early supernovae (SN) explosions dust grains are formed. Dust and metals are released in the interstellar medium (ISM) and they eventually enrich the IGM through SN-driven winds. The impact of feedback processes onto the subsequent structure formation is very strong; their efficiencies depend on both the properties of the first stars and on that of the primordial galaxies hosting them.

Given the sensitivity of current telescopes, not allowing to reach redshifts beyond $z \approx 8$, we are actually lacking of direct observational data from these remote epochs, deserving the name of "Dark Ages" $8 \lesssim z \lesssim 1100$. A possible way to overcome the problem is to exploit the imprints of feedback processes left in today living galaxies, therefore indirectly investigating these epochs. In particular "stellar archeology" of the most metal-poor stars in the Galactic halo and in nearby dwarf galaxies represents one of the most promising tools to investigate the features of the first stars and primeval galaxies.

In this Chapter I will first describe the physical ingredients governing the growth of primordial density fluctuations along with their modeling. Then I will analyze how and where first stars form pointing out their main features. Next I will review the three main feedback processes acting during early cosmic structure formation (radiative, mechanical and chemical) after which the crucial role of today living metal-poor stars and dwarf galaxies will clearly emerge. Finally, I will present the state-of-the-art of the observations of the most metal-poor stars and of the dwarf spheroidal galaxies in the Milky Way system. In particular, I will highlight the puzzling open questions arising from them.

1.1 Structure formation

The commonly adopted theory for structure formation, the *gravitational instability scenario*, is presented in this Section. Hereafter we will implicitly assume the popular ΛCDM model, according to which dark matter (DM) is composed by cold, weakly interacting, massive particles. The cosmological parameters adopted are consistent with the 3-years WMAP data (Spergel et al. 2007): $h = 0.73$, $\Omega_m = 0.24$, $\Omega_\Lambda = 0.72$, $\Omega_b h^2 = 0.02$, $n = 0.95$, $\sigma_8 = 0.74$.

1.1.1 Linear regime

In studying how matter responds to its own gravitational field in an expanding Universe, a linear perturbation theory can be adopted as long as the density fluctuations are small; the CMB properties ensure that this condition is fully satisfied at $z \approx 1100$. Let's describe the Universe in terms of a fluid made of collision-less dark matter and collisional baryons, with an average mass density $\overline{\rho}$; at any time and location the mass density can be expanded in terms of a dimensionless density perturbation $\delta(\mathbf{x}, t)$ as $\rho(\mathbf{x}, t) = \overline{\rho}(t)[1 + \delta(\mathbf{x}, t)]$, where $\mathbf{x}$ indicates the comoving spatial density. During the linear regime ($\delta \ll 1$), the time evolution equation for δ reads (Peebles 1993):

$$\ddot{\delta}(\mathbf{x}, t) + 2H(t)\dot{\delta}(\mathbf{x}, t) = 4\pi G\overline{\rho}(t)\delta(\mathbf{x}, t) + \frac{{c_s}^2}{a(t)^2}\nabla^2\delta(\mathbf{x}, t) \quad , \tag{1.1}$$

where c_s is the sound speed, $a \equiv (1+z)^{-1}$ is the scale factor describing the expansion of the Universe and $H(t) = H_0[\Omega_m(1+z)^3 + \Omega_\Lambda]^{1/2}$. The growth of the perturbations due to gravitational collapse (first term on the right hand side) is counteracted by both the cosmological expansion (second term on the left hand side) and the pressure support (second term on the right hand side). The latter is essentially provided by collisions in the baryonic gas, while in the collision-less dark matter component it arises from the readjustment of the particles orbits. The total density contrast at any spatial location can be described in the Fourier space as a superposition of modes with different wavelength:

$$\delta(\mathbf{x}, t) = \int \frac{d^3\mathbf{k}}{(2\pi)^3}\delta_{\mathbf{k}}(t) exp(i\mathbf{k} \cdot \mathbf{x}) \quad , \tag{1.2}$$

where $\mathbf{k}$ is the comoving wave number. Hence, the single Fourier component evolution is given by:

$$\ddot{\delta}_{\mathbf{k}} + 2H(t)\dot{\delta}_{\mathbf{k}} = \Big(4\pi G\overline{\rho} - \frac{k^2 c_s^2}{a^2}\Big)\delta_{\mathbf{k}} \quad . \tag{1.3}$$

The above equation implicitly defines a critical scale, the Jeans length (Jeans 1928), at which the competitive pressure and gravitational forces cancel:

$$\lambda_J = \frac{2\pi a}{k_J} = \left(\frac{\pi c_s^2}{G\overline{\rho}}\right)^{1/2} \quad . \tag{1.4}$$

For $\lambda < \lambda_J$ the pressure force counteract gravity and the density contrast oscillates as a sound wave. For $\lambda \gg \lambda_J$ instead, the time-scale associated to the pressure force is much longer than the gravitational one, and a zero pressure solution can be applied. The Jeans mass, defined as the mass within a sphere of radius $\lambda_J/2$, is usually introduced to reformulate the instability criterion in terms of a critical mass:

$$M_J = \frac{4\pi}{3}\overline{\rho}\left(\frac{\lambda_J}{2}\right)^3 \quad . \tag{1.5}$$

Similarly, in a perturbation with mass $\gg M_J$ the pressure force is not counteracted by gravity and the structure collapses. This sets a limit on the scales that are able to collapse at each epoch and has a different value according to the perturbed component (baryonic or dark matter) under consideration, reflecting their different velocity.

After recombination the $\lambda \gg \lambda_J$ modes in the non-relativistic regime grow as the scale factor a, both in the DM and in the baryonic component (Padmanabhan 1993). For the adopted cosmological parameters a good approximation of the linear growth factor $D(z)$, between redshift z and the present, is given by (Carroll, Press & Turner 1992):

$$D(z) = \frac{5\Omega_m(z)}{2(1+z)}\left(\frac{1}{70} + \frac{209}{140}\Omega_m(z) - \frac{\Omega_m^2(z)}{140} + \Omega_m^{4/7}(z)\right)^{-1} \tag{1.6}$$

where

$$\Omega_m(z) = \frac{\Omega_m(1+z)^3}{\Omega_m(1+z)^3 + \Omega_\Lambda} \quad . \tag{1.7}$$

More generally given an initial power spectrum of the perturbations, $P_{in}(k) \equiv \langle|\delta_{\mathbf{k}}^2|\rangle$, the evolution of each mode including those with short wavelengths, can be followed through eq. 1.3 and then integrated to recover the global spectrum at any time. The properties of the perturbations growth on different scales and at different times are encapsulated in the transfer function, $T(k)$, providing the ratio of the today amplitude of a mode to its initial value. Inflationary theories predict $P_{in}(k) \propto k^n$, with $n \sim 1$, and perturbations given by a Gaussian random field. Therefore $P(k)$, *i.e.* the variance, describes the statistical properties of the fluctuations. The today power spectrum is given by:

$$P(k) = P_{in}(k)T(k)^2 = Ak^nT(k)^2 \quad , \tag{1.8}$$

where A is a normalization parameter that has to be fixed through observations. A good fit for the transfer function is given by (Bardeen et al. 1986):

$$T(k) = \frac{\ln(1+2.34q)}{2.34q}\left[1 + 3.89q + (16.1q)^2 + (5.46q)^3 + (6.71q)^4\right]^{-1/4}, \tag{1.9}$$

where $q \equiv (k/h\Gamma)\mathrm{Mpc}^{-1}$. The shape parameter Γ, later introduced by Sugiyama (1995), accounts for the effects of the non-zero baryonic density:

$$\Gamma = \Omega_0 h \exp[-\Omega_b(1 + \sqrt{2h}/\Omega_0)] \quad . \tag{1.10}$$

In order to determine the formation of objects of a given size and mass, it is useful to consider the statistical distribution of the smoothed density field. Using a normalized window function $W(\mathbf{y})$ so that $\int d^3\mathbf{y}W(\mathbf{y}) = 1$, the smoothed density perturbation field $\int d^3\mathbf{y}\delta(\mathbf{x}+\mathbf{y})W(\mathbf{y})$ follows itself a gaussian distribution with zero mean. For the particular choice of a spherical top-hat window function, $W(kR) = 4\pi R^3[(\sin(kR) - kR\cos(kR))/(kR)^3]$, in which $W = 1$ in a sphere of radius R and it is zero outside, the smoothed perturbation field measures the mass fluctuation, δ_M, in a sphere of radius R (Barkana & Loeb 2001). The mass variance is defined as the root-mean square of the density fluctuation:

$$\sigma^2(M) = \delta_M^2 = \frac{1}{2\pi}\int_0^\infty P(k)W^2(kR)k^2dk, \tag{1.11}$$

This function plays a crucial role in estimating the abundance of collapsed objects, as it will be described in the following Section. The normalization constant of the initial power spectrum, A, is specified by the value of $\sigma_8 \equiv \sigma(R = 8h^{-1}\mathrm{Mpc})$ derived from the CMB analysis. Note that most of the power of the fluctuation spectrum is on small scales, implying that in standard CDM models low mass objects are those predicted to collapse first.

1.1.2 Non-linear regime: dark matter haloes

Since DM is made of collision-less particles that interact very weakly with the rest of the matter and with the radiation field, density perturbations in this component start growing at early epochs. However, as soon as $\delta \approx 1$, the linear perturbation theory does not apply anymore, and the full non-linear gravitational problem must be considered. The dynamical collapse of a dark matter halo can be analytically solved in the simplest case of spherical symmetry, with an initial overdensity δ uniformly distributed inside a sphere of radius R (top hat). In this case the enclosed δ initially grow according to the linear theory; then it reaches its maximum radius of expansion, turns around and starts to contract, ideally collapsing into a point. However, long before this happens, the DM experience a violent relaxation process, quickly reaching the virial equilibrium. A dark matter halo of mass M virializing at redshift z, can be fully described in terms of its virial (physical) radius r_{vir}, circular velocity $v_c = \sqrt{GM/r_{vir}}$, and virial temperature $T_{vir} = \mu m_p v_c^2/2k_B$, whose expressions are (Barkana & Loeb 2001):

$$r_{vir} = 0.784 \left(\frac{M}{10^8 h^{-1} M_\odot}\right)^{1/3} \left[\frac{\Omega_m}{\Omega_m(z)} \frac{\Delta_c}{18\pi^2}\right]^{-1/3} \left(\frac{1+z}{10}\right)^{-1} h^{-1}\mathrm{kpc} \quad , \tag{1.12}$$

$$v_c = 23.4 \left(\frac{M}{10^8 h^{-1} M_\odot}\right)^{1/3} \left[\frac{\Omega_m}{\Omega_m(z)} \frac{\Delta_c}{18\pi^2}\right]^{1/6} \left(\frac{1+z}{10}\right)^{1/2} \mathrm{km\ s^{-1}} \quad , \tag{1.13}$$

$$T_{vir} = 2 \times 10^4 \left(\frac{\mu}{0.6}\right) \left(\frac{M}{10^8 h^{-1} M_\odot}\right)^{2/3} \left[\frac{\Omega_m}{\Omega_m(z)} \frac{\Delta_c}{18\pi^2}\right]^{1/3} \left(\frac{1+z}{10}\right) \mathrm{K} \quad , \tag{1.14}$$

where m_p is the proton mass, μ the mean molecular weight and (Bryan & Norman 1998)

$$\Delta_c = 18\pi^2 + 82(\Omega_m(z) - 1) - 39(\Omega_m(z) - 1)^2 \quad . \tag{1.15}$$

Other than characterizing the properties of individual haloes, a crucial prediction of the structure formation theory is the halo abundance *i.e.* the number density of haloes as a function of mass at any redshift. Such information can be derived both numerically, by solving the equation of gravitational collapse, or analytically, by approximating the equations with one-dimensional functions. A simple analytical model which successfully matches most of the numerical simulations, was developed by Press & Schechter in 1974. The density field smoothed on a mass scale M, δ_M, (eq. 1.11) is the key ingredient used to determine the haloes abundance. At the moment in which the top-hat collapse to a point the today overdensity predicted by both the linear and the non-linear theory gives roughly the same value ≈ 1.686. Therefore one can assert that a top-hat fluctuation collapses at redshift z if δ_M is higher than the critical value:

$$\delta_c(z) = \frac{1.686}{D(z)} \tag{1.16}$$

where $D(z=0) = 1$. The fundamental *Ansatz* of the Press & Schechter theory is to identify the probability that $\delta_M > \delta_c(z)$ with the fraction of DM particles which are part of collapsed haloes with mass grater than M at redshift z. According to this, the comoving number density of haloes, dn, with mass between M and $M + dM$ at a given redshift z is given by (Barkana & Loeb 2001):

$$\frac{dn}{dM} = \sqrt{\frac{2}{\pi}} \frac{\rho_m}{M} \frac{-d(\ln \sigma_M)}{dM} \nu_c \exp(-\nu_c^2/2) \quad , \tag{1.17}$$

where ρ_m is the present mean mass density ($\Omega_m \rho_c$) and $\nu_c = \delta_c(z)/\sigma(M)$ is the number of standard deviation which $\delta_c(z)$ represents on mass scale M. The abundance of haloes critically depends on this quantity: haloes corresponding to high-σ density fluctuations, *i.e.* high ν_c, are extremely rare in the Universe. Given that $\delta_c(z)$ decreases with z, while according to CDM models $\sigma(M)$ increases at decreasing masses (see Fig. 5 of Barkana & Loeb 2001), the typical mass associated to low-σ density fluctuations is higher at lower z; in other words, massive haloes become more and more abundant at decreasing redshifts. This is a peculiar feature of CDM models in which the growth of structures proceeds *hierarchically* through the continuous merging processes of smaller dark matter haloes.

Such a hierarchical growth substantially complicates the physics governing the inner structure of the haloes, to investigate which numerical simulations are needed. Navarro, Frenk & White (1996, 1997) simulated the formation of DM haloes with different masses, finding that their density profile (NFW profile) has a universal shape, independent of the halo mass, initial density perturbation spectrum and cosmological parameters:

$$\rho(r) = \frac{\rho_s}{(r/r_s)(1 + r/r_s)^2} \quad , \tag{1.18}$$

where ρ_s and r_s are the characteristic density and radius. By introducing the concentration parameter $c \equiv r_{vir}/r_s$ and writing ρ_s in terms of c, the above equation becomes a one-parameter form. The halo mass and ρ_s are strongly correlated: low-mass haloes are denser than more massive systems, reflecting the higher collapse redshift of smaller haloes. However there is still a lack of a general consensus about the idea of a universal shape of the halo density profile (see Ciardi & Ferrara 2005 for a complete review). Similarly, the cuspy density profile predicted by the eq. 1.18 is not confirmed by kinematics observations in galaxies, which favor a cored profile (Salucci & Burkert 2000), nor by recent numerical simulation including gas (Stoehr 2006).

In conclusion, our present understanding of the perturbation growth through the cosmic time allows to describe the abundance and general properties of virialized DM haloes, achieving a good match between simulations and semi-analytical models. Nevertheless cosmological simulations of increasingly higher resolution demonstrated that virialized regions of CDM haloes are filled with a multitude of DM subhaloes, which survived the hierarchical sequence of merging and accretion (Kravtsov 2009). As we will discuss in Sec. 1.5.2, a comparison with the observations revealed an apparent discrepancy between the abundance of subhaloes and the luminous MW satellite, usually known as the “missing satellites” problem. On the other hand, the internal structure of the haloes is still quite debated, and a definitive answer reconciling all the theoretical studies is lacking.

1.1.3 Non-linear regime: protogalaxies formation

In contrast to dark matter, as long as the gas is fully ionized the radiation drag on free electrons prevents the formation of gravitationally bound systems. After the decoupling instead, perturbations in the baryonic component are finally able to grow in the pre-existing dark matter halo potential wells, eventually leading to the formation of the first bound objects. The virialization process of the gas component is similar to the dark matter one; in this case however the gas develops shocks during the contraction that follows the turnaround, and gets reheated to a temperature at which pressure support can prevent further collapse.

The minimum mass of the first bound objects, *i.e.* the Jeans mass, can be derived using the eqs. 1.4-1.5 where c_s is the sound velocity of the baryonic gas $c_s^2 = dp/d\rho = RT/\mu$. Since the residual ionization of the cosmic gas keeps its temperature locked to that of the CMB through different physical processes, down to a redshift $1 + z_t \approx 1000(\Omega_b h^2)^{2/5}$ (Peebles 1993), *i.e.* $T \propto (1 + z)$, the Jeans mass results time-independent for $z > z_t$ as $\rho_m \propto (1 + z)^3$. When $z < z_t$ instead, the gas temperature declines adiabatically ($T \propto (1 + z)^2$), and M_J decreases with decreasing redshift:

$$M_J = 3.08 \times 10^3 \left(\frac{\Omega_m h^2}{0.13}\right)^{-1/2} \left(\frac{\Omega_b h^2}{0.022}\right)^{-3/5} \left(\frac{1+z}{10}\right)^{3/2} \mathrm{M}_\odot. \qquad (1.19)$$

Again, as the determination of the Jeans mass is based on a perturbative approach, it can only describe the initial phase of the collapse. Moreover we have to stress that M_J only represents a *necessary but not sufficient* condition for collapse: the gas cooling time, t_{cool}, has to be shorter than the Hubble time, t_H, in order to allow the gas to condense. Therefore, the efficiency of gas cooling is crucial in determining the minimum mass of protogalaxies.

As already pointed out, in standard ΛCDM models the first collapsing objects are predicted to be the least massive ones, *i.e.* those with the lowest virial temperatures (eq. 1.14). For $T_{vir} < 10^4$ K and in gas of primordial composition, molecular hydrogen, H_2, represents the main available coolant (see Fig. 12 of Barkana & Loeb 2001). The first stars are predicted to be formed in such a H_2 cooling haloes, which are usually called *minihaloes*. The cooling ability of these objects essentially depends on the abundance of molecular hydrogen: the gas cool for radiative de-exitation if the H_2 molecule gets rotationally or vibrationally excited through a collision with an H atom of another H_2 molecule. Primordial H_2 forms with a fractional abundance of $\approx 10^7$ at $z > 400$ via the H_2^+ formation channel. At $z < 110$, when the CMB radiation intensity becomes weak enough to allow for a significant formation of H^- ions, more H_2 molecules can be formed:

$$\begin{aligned} \mathrm{H} + \mathrm{e}^- &\rightarrow \mathrm{H}^- + \mathrm{h}\nu \\ \mathrm{H}^- + H &\rightarrow \mathrm{H}_2 + \mathrm{e}^- \end{aligned}$$

By assuming that H^- is the dominant formation channel for H_2, we get to a typical primordial H_2 fraction of $f_{H_2} \approx 2 \times 10^{-6}$ (Anninos & Norman 1996), which is lower than that required to efficiently cool the gas and trigger the SF process $f_{H_2} \approx 5 \times 10^{-4}$ (Tegmark et al. 1997). However, during the collapse, the H_2 content can be significantly enhanced; the fate of a virialized clump conclusively depends on its ability to rapidly increase its H_2 content during such a collapse phase. Tegmark et al. (1997) investigated the evolution of the H_2 abundance for different halo masses and initial conditions finding that only the larger haloes reaches the critical molecular hydrogen fraction for the collapse. This implies that for each virialization redshift there exist a critical mass, $M_{sf}(z)$, so that $M > M_{sf}(z)$ haloes will be able to collapse and form stars while those with $M < M_{sf}(z)$ will fail. However, the value and evolution of $M_{sf}(z)$ is highly debated as it strongly depends on the H_2 cooling functions used and chemical reactions included (Fuller & Couchman 2000) other than on radiative feedback effects once the first stellar generation formed (see Sec. 1.3). Nevertheless, many of the most recent and complete studies (Abel, Brian & Norman 2000; Machacek, Brian & Abel 2001; Reed et al. 2005; O'Shea & Norman 2007) agree that the absolute minimum mass allowed to collapse is as low as $10^5 M_\odot$. Note that as soon as more massive haloes with $T_{vir} > 10^4$ K become non-linear, the gas cooling proceed unimpeded in these hot objects through atomic line cooling.

1.2 Star formation and evolution

Once having clarified which are the physical conditions to be satisfied in order to form a protogalaxy, we can analyze the key ingredients governing the primordial star formation process.

1.2.1 Characteristic masses

Although the very first generation of stars formed out of a pure H/He gas which was probably very weakly magnetized, leading to a significant simplification of the relevant physics involved in the problem, the primordial star formation process and its final products are still quite unknown. This largely depends on our persisting ignorance of the fragmentation process and on its connection with the thermodynamical conditions of the gas.

The evolution of a proto-stellar gas cloud crucially depends on the relationship between the cooling time-scale, $t_{\rm cool} = 3nkT/2\Lambda(n,T)$, and the free-fall time, $t_{\rm ff} = (3\pi/32G\rho)^{1/2}$ where n (ρ) is the gas number (mass) density and $\Lambda(n,T)$ is net radiative cooling rate (in units of erg cm^{-3}s^{-1}). In general (Schneider et al. 2002), cooling is efficient when $t_{\rm cool} \ll t_{\rm ff}$. When this condition is satisfied the energy deposited by gravitational contraction cannot balance the radiative losses; as a consequence temperature decreases with increasing density and, during the cooling, the gas cloud fragments. At any given time fragments form on typical length-scale small enough to ensure equilibrium between gravitational forces and pressure, *i.e.* $R_F \sim \lambda_J \propto c_s t_{ff}$. Since $c_s \propto T^{1/2}$ varies on the cooling time-scale the corresponding R_F becomes smaller as T decreases, and the fragmentation proceeds hierarchically. The necessary condition to stop fragmentation and start the gravitational contraction within each fragment, is that the Jeans lenght (mass) does not decrease any further. When this condition is satisfied the star formation begins.

Several authors have investigated such a fragmentation process (Abel et al. 1998; Abel, Brian & Norman 2000; Nakamura & Umemura 2001, 2002; Bromm, Coppi & Larson 2002; Schneider et al. 2002; Ripamonti et al. 2002; Bromm & Loeb 2004; Yoshida et al. 2006; O'Shea & Norman 2007) tackling the problem both numerically and analytically, and converging on the idea that the collapsing gas clouds fragment in clumps of mass $\approx 10^2 - 10^3 M_\odot$. The latter are the progenitors of the stars which will later form in their interiors, accreting gas on the central protostellar core. Since gas accretion is very efficient at low metallicities (Omukai & Palla 2003) given such initial conditions a massive star is very likely to form. However, the late phases of accretion are complicated by protostellar feedback and the final stellar mass is still largely uncertain but likely in the range $(30 - 300) M_\odot$ (Tan & McKee 2004, McKee & Tan 2008).

It is pointless to note that the distribution of masses with which first stars are formed, the so-called Initial Mass Function (IMF), is still completely unknown given the large theoretical uncertainties in the fragmentation and accretion processes underlined so far. Nevertheless it is very likely that the IMF should be naturally biased toward massive stars at high redshifts, given the temperature dependence of the Jeans mass and the gradual cooling of the Universe (Larson 1998).

1.2.2 The final fate

The major difference in the evolution of metal poor stars with respect to those with $Z > 10^{-4} Z_\odot$, lies in the mechanism of nuclear energy generation. Indeed, given the lack of CNO nuclei, during the pre-main sequence phase gravitational contraction must be counteracted by the energy budget provided by the p-p chain. The latter, being a poor thermostat, is never sufficient to power massive stars which therefore contract until the central temperature is $T \approx 10^8$ K (Marigo et al. 2001) and CNO seed isotopes are produced by triple-α reaction.

Several numerical investigations of the evolution and final fate of metal-free stars, extensible to all $Z \lesssim 10^{-4} Z_\odot$ stars, have been developed (Woosley & Weaver 1995; Heger & Woosley 2002; Fryer et al. 2001; Umeda & Nomoto 2002). The complete picture, for the case of *non-rotating stars*[1] is summarized in Fig. 1.1 by Heger & Woosley (2002). Three main regimes of initial mass can be distinguished:

---

[1] In rotating stars the mass loss should be strongly increased due to mixing processes (Meynet et al. 2006) affecting the subsequent stellar evolution.

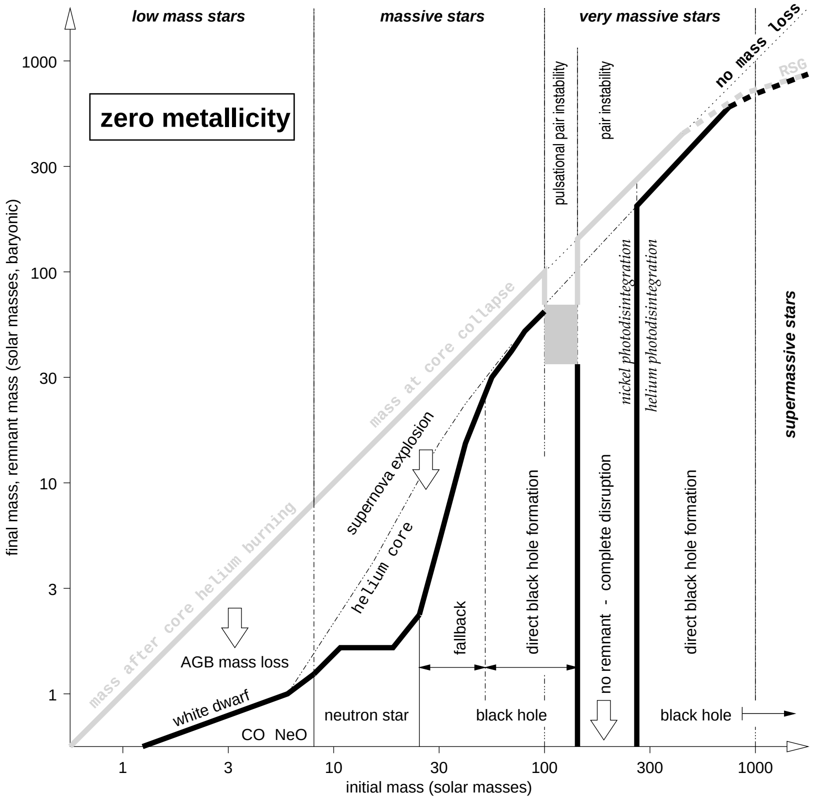

Figure 1.1: Initial-final mass function of Pop III stars by Heger & Woosley 2002. The horizontal axis gives the initial stellar mass. The y-axis gives the final mass of the collapsed remnant (thick black curve) and the mass of the star at the beginning of the event producing that remnant (thick gray curve). Since no mass loss is expected from metal-poor stars before the final stage, the gray curve is approximately the same as the line of no mass loss (dotted). Exceptions are $\approx 100 - 140$ $\mathrm{M}_\odot$ where the pulsational pair-instability ejects the outer layers of the star before it collapses.

- *low mass stars* $m \lesssim 10M_\odot$: they develop a electron-degenerate core and loose their envelope during AGB phase becoming CO or NeO white dwarfs. The AGB phase is characterized by thermal pulses and dredge-up events, though the mechanism and thus the resulting initial-final mass function may differ from solar composition stars.

- *massive stars* $10M_\odot \lesssim m \lesssim 100M_\odot$: they are defined as those that ignite carbon and oxygen burning non-degenerately and do not leave white dwarfs. The hydrogen-rich envelope and parts of the helium core are ejected in a supernova explosion. Below an initial mass of $\sim 25M_\odot$ neutron stars are formed. Above that black holes (BHs) form, either by fall back of the ejecta or directly during iron core collapse for $m \gtrsim 40M_\odot$.

- *very massive stars* $m > 100M_\odot$: they are characterized by electron-positron

> pair instability. After the central He burning these massive stars have high enough central entropy to enter in a temperature density regime in which electron-positron pairs are created in abundance, converting internal energy into rest mass of the pairs without contributing much to the pressure (Barkat, Rakavy & Sack 1967; Bond et al. 1984). Hence the star contract rapidly until implosive oxygen and silicon burning produce enough energy, depending on m, to reverse the collapse. This occurs in the mass range of the *pair instability supernovae*, SN$_{\gamma\gamma}$: $140 M_\odot \leq m \leq 260 M_\odot$. These stars are completely disrupted in a nuclear-powered explosions, that lives no remnants and releases *all* the initial stellar mass into the ISM. The explosion energy of a $m = 200 M_\odot$ star is $\sim 2.7 \times 10^{52}$ erg. *i.e.* more than one order of magnitude higher than that of supernovae type II, $\sim 1.2 \times 10^{51}$ erg. Outside the SN$_{\gamma\gamma}$ mass range the star collapse into a BH. For $m > 260$ M$_\odot$ this occurs because the star encounters a photodisintegration instability before explosive burning reverses the implosion.

From this picture emerges that the dominant contribution to the metal enrichment by metal-free stars originate from SN$_{\gamma\gamma}$, this conclusion being even more robust given the predicted mass range for these primordial stars $m = (30-300) M_\odot$. In their study Heger & Woolsey (2002) extensively investigated such evolutionary channel finding that SN$_{\gamma\gamma}$ produce a huge amount of metals, equal to the 45% of the progenitor mass in the whole mass range. In primordial composition stars the neutron excess is very low, only coming from the conversion of ^{14}N into ^{14}O at the end of the He burning, when traces of CNO elements have been produced. As a consequence nuclei that require a neutron excess for their production, *i.e.* all nuclei with odd charge above ^{14}N, are under-produced with respect to normal stars. This yields the so-called odd-even effect which provide a distinctive signature of the nucleosynthetic pattern of $Z \lesssim 10^{-4} Z_\odot$ SN$_{\gamma\gamma}$. Moreover, no elements heavier than Zn are produced by these stars, owing to the lack of r- and s- processes.

Schneider, Ferrara & Salvaterra (2004), investigated the dust production by SN$_{\gamma\gamma}$, finding that the $\sim (30-70)\%$ of the metals released by these stars is depleted into dust grains, with a depletion factor, $f_{dep} = M_{dust}/M_Z$, that increases with m. As we will discuss in the next Section, dust grains are crucial in driving the transition from very massive to low-mass stars.

1.3 Feedback processes

As soon as the first stellar generations form, feedback processes from these sources dramatically change the simple picture described above, affecting the subsequent formation of structures in the entire mass range: from protogalactic haloes to second generation stars. Feedback processes are usually divided into three broad classes, though they frequently interplay: radiative, mechanical and chemical feedback.

1.3.1 Radiative feedback

Radiative feedback is related to the dissociating/ionizing radiation produced by massive stars (or quasars). This radiation can have both local effects, inside the same galaxy producing it, and long-range effects, either affecting the formation and evolution of nearby objects, or joining the radiation produced by other galaxies to form a background.

Before reionization, radiative feedback predominantly affects the physics of minihaloes. Hydrogen molecules indeed can be easily photodissociated by UV photons in the Lyman-Werner (LW) band. The formation of the first stars acts on the star forming clouds as both internal (Omukai & Nishi 1999; Glover & Brand 2001; Oh & Haiman 2002) and external (Haiman, Rees & Loeb 1997; Ciardi, Ferrara & Abel 2000; Ciardi et al. 2000; Haiman, Abel & Rees 2000; Ricotti, Gnedin & Shull 2002; Mackey, Bromm & Hernquist 2003; Yoshida et al. 2003; Wise & Abel 2008) negative feedback, reducing the gas cooling and hence the SF efficiency in minihaloes. It is extremely hard to estimate the net effect of this negative feedback, which depends on the intensity of the LW flux (Machaceck, Brian & Abel 2001), on the self-shielding of the baryons (Susa & Umemura 2004; Ahn & Shapiro 2007), on the presence of metals (Nishi & Tashiro 2000), and on the existence of a positive feedback, possibly allowing the H_2 re-formation in recombining ionized regions (Ricotti, Gnedin & Shull 2001, 2002; Johnson, Grief & Bromm 2007), and in cooling gas behind shocks produced during gas ejection (Ferrara 1998). Nevertheless several authors (Madau, Ferrara & Rees 2001; Ricotti & Gnedin 2005; Okamoto, Gao & Theuns 2008) agree in finding that radiative feedback effects cause a decrease of the minihaloes SF efficiency $\propto T_{vir}^3$.

On the other hand, the UV radiation field from the first stellar generations can inhibit the formation of the smallest mass objects, hence increasing M_{sf}, by heating their gas above the virial temperature and photoevaporating it (Ciardi, Ferrara & Abel 2000; Kitayama et al. 2000; Machacek, Bryan & Abel 2001). According to Dijkstra et al. (2004) such feedback effect is only marginal at high redshift, and at $z \approx 10$ low-mass objects with $v_c \geq 10$ kms^{-1} ($M_{vir} \approx 8 \times 10^6 M_{\odot}$) can self-shield and collapse. As this feedback is related with the physics of the H_2, its effects are altered by the afore-mentioned photodissociating LW background. During reionization the interplay between these two feedback types is quite complicated and no consensus is found on the evolution of $M_{sf}(z)$ (see for example Fig. 25 of Ciardi & Ferrara 2005).

Finally, the heating associated with photoionization raises the temperature of progressively ionized cosmic regions increasing the Jeans mass; as a consequence (eqs. 1.4-1.5) the infall of gas in haloes below a given circular velocity, v_c^*, is quenched meaning that M_{sf} increases further on. The evolution of $v_c^*(z)$ depends on the details of the *overall* reionization history (Gnedin 2000, Schneider et al. 2008) which is still quite debated (see Ciardi & Ferrara 2005). At the moment theoretical calculations combined with the available observations predict that the end of reionization has been occurred somewhere between $5.5 < z < 10$ (Choudhury & Ferrara 2006). When reionization is complete $v_c^* \approx 30$ kms^{-1} (Kitayama et al. 2000). Note that this value corresponds virial temperature $T_{vir} > 10^4$ K (eqs. 1.13-1.14), meaning that this kind of feedback is also affecting Lyα cooling haloes. Still, at any given redshift, radiative feedback controls the properties of the least massive haloes.

1.3.2 Mechanical feedback

In addition to radiative feedback, the SF process can be strongly affected by mechanical feedback associated with mass and energy deposition from the first stars. Indeed, depending on the binding energy of the galaxies, SN and multi-SN events might induce partial (*blowout*) on total (*blowaway*) gas removal from the galaxy itself, thus subtracting the fuel to power the SF and hence regulating it (MacLow & Ferrara 1999; Nishi & Susa 1999; Springel & Hernquist 2003; Wada & Venkatesan 2003). In general, mechanical feedback effects are found to be dramatic in galaxies with a low DM content, because of their shallow potential wells (Ferrara & Tolstoy 2000; Mori, Ferrara & Madau 2002), and in those hosting metal-free SN$_{\gamma\gamma}$ (Bromm, Yoshida & Hernquist 2003), because of the higher explosion energy of these primordial stellar generations (see Sec. 1.2.2).

Other than locally, mechanical feedback can affect the SF process in nearby objects as the effect of SN shocks can cause the heating, evaporation and/or stripping of the baryonic matter (Scannapieco, Ferrara & Broadhurst 2000). In the first scenarios the gas in a forming galaxy is heated above its T_{vir} by the shocks; hence the thermal pressure of the gas overcomes the DM potential and, depending on the cooling time, the gas eventually expands out of the halo preventing the formation of the galaxy. In the latter scenario the gas may be stripped from a collapsing perturbation by a shock from a nearby source.

Finally, mechanical feedback plays a crucial role in changing the chemical composition of the environment out of which subsequent galaxy formation occurs. In fact, the heavy elements produced during SN explosions can be easily ejected outside of the star-forming galaxies together with the gas (Vader 1986; Mac Low & Ferrara, 1999; Fujita et al. 2004). As a consequence the average metallicity of the IGM gradually increases, changing the cooling properties of the gas, hence eventually affecting both the $M_{sf}(z)$ evolution and the typical mass of the subsequent stellar generations.

In Fig. 1.2 we report the result of an extremely high-resolution numerical simulation (Mori & Umemura 2006), following the early evolutionary stages of a protogalaxy with total mass $10^{11} M_{\odot}$. In the first 100 Myr stars form in high-density peaks; the gas in the vicinity of SN is quickly enriched with ejected metals (oxygen), and the metallicity distribution of the galaxy environment becomes highly inhomogeneous on kpc scales. After 300 Myr SN-driven shocks collide with each other to

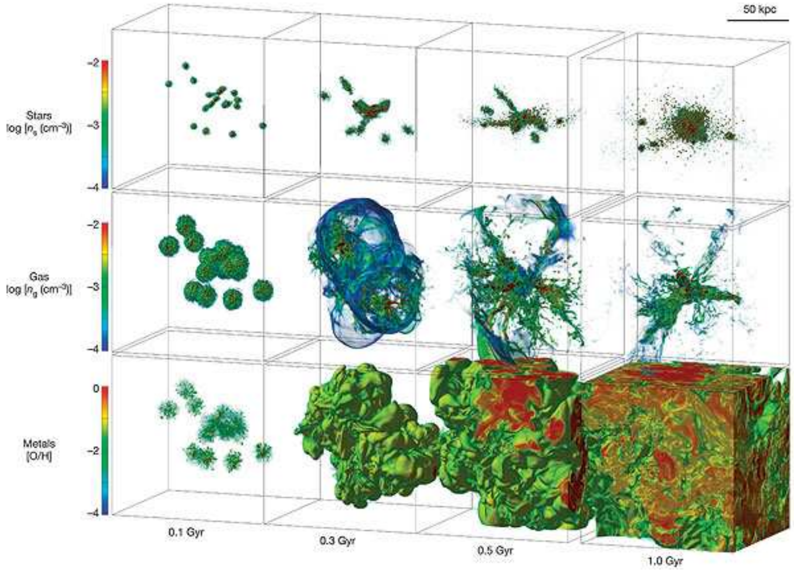

Figure 1.2: Spatial distribution of the stellar density, gas density and oxygen abundance of a protogalaxy with total mass $\sim 10^{11} M_\odot$ by Mori & Umemura 2006. The results are shown at different times: $(0.1, 0.3, 0.5, 1)$ Gyr. Each simulation box has a physical size of 134 kpc and a spatial resolution of 0.131 kpc.

generate super-bubbles which finally blow out into the IGM after 500 Myr. At this stage the oxygen abundance converge to an average value with very small dispersions, which decreases further on after 1 Gyr. Again such effects are even more extreme in less massive protogalactic haloes.

1.3.3 Chemical feedback

The concept of chemical feedback has been recently introduced (Bromm et al. 2001; Schneider et al. 2002, 2003; Mackey, Bromm & Hernquist 2003) in order to account for the transition from massive metal-free stars to "normal" stars. Indeed, since the characteristic mass of locally observed stars is $\sim 1 M_\odot$ while metal-free stars are predicted to be very massive, some transformation in the properties of star-forming regions must have been occurred through the cosmic times.

Recent theoretical studies suggest that the initial metallicity of the star-forming gas represents the key element controlling this transition (Bromm et al. 2001; Omukai 2000; Omukai et al. 2005; Schneider et al. 2002, 2003, 2006; Bromm & Loeb 2004). Following the evolution of protostellar gas clouds with different values of the initial metallicity and including dust and molecules as cooling agents, Schneider et al. (2002-2006) and Omukai et al. (2005) find that when the metallicity is in the critical range $10^{-6} < Z_{cr}/Z_\odot < 10^{-4}$, the typical fragmentation scales move from $\sim 10^3 M_\odot$ to solar or sub-solar values. Given that gas accretion is less efficient at high metallicities (Omukai & Palla 2003) such result implies the occurrence of a transition in the characteristic stellar masses. The critical metallicity value depends on the fraction of metals locked in dust grains, which provide an additional cooling channel at high densities enabling fragmentation to solar and sub-solar clumps (Schneider et al. 2003, 2006; Omukai et al. 2005; Tsuribe & Omukai 2006). Thus, the onset of low-mass star formation in the Universe is triggered by the presence of metals and dust in the parent clouds to levels exceeding Z_{cr}.

In the following of this Thesis we will refer to Population III stars (Pop III) as those formed out of a $Z \leq Z_{cr}$ gas and hence characterized by high stellar masses. Since the results by Heger & Woosley (2002) can be applied to metal-poor stars up to metallicities $Z \sim 10^{-4} Z_{\odot} \geq Z_{cr}$ the evolution and final fate of Pop III stars will follow their picture. Instead, we will dub as Population II/I stars (Pop II/I) those formed out of a $Z > Z_{cr}$ gas, according to the present-day Salpeter IMF $\Phi(m) = dN/dm \propto m^{-2.35}$.

In a recent paper Tornatore, Ferrara & Schneider (2007) used a cosmological simulation to investigate the Pop III to Pop II/I transition induced by chemical feedback. According to their findings long-living Pop II stars can form at very high redshifts in haloes self-enriched by Pop III stars. Therefore the contribution of Pop III stars to the global SF rate (SFR) is always sub-dominant, being $\sim 10^{-4}$ that of Pop II/I stars. The SFR density of Pop III stars reaches its maximum value at $z \approx 6$, gradually decreasing at decreasing z and finally dropping to negligible values at $z \approx 2.5$. At that time Pop III stars disappear.

1.4 Cosmic relics & feedback survivors

From this picture, delineating our *poor* actual understanding about the formation and evolution of the first galaxies, emerges the crucial role played by feedback processes, quickly starting in regulating (and complicating) the overall structure formation process, leaving their imprint on the properties of the subsequent generations of stars and galaxies. We know that the first stars are expected to form at $z = (20-30)$ within the primeval low-mass protogalactic haloes, corresponding to high-σ density fluctuations. Although the next generation of telescope with exceptional new sensitivity in the Infrared and radio bands (as JWST and LOFAR) will hopefully open a new observational window on this high redshift Universe, at the moment the most distant sources known is a $z = 8.2$ gamma ray burst, that has been observed few months ago (Salvaterra et al. 2009, Tanvir et al. 2009). Hence we are actually very far away from observing the early phases of galaxies formation. However, feedback imprints in the Local Universe offer an alternative way to overcome such observational barrier.

At the moment, stellar archeology of the most metal-poor stars probably represent one the most promising methods to indirectly investigate the properties of the first stellar generations. Low-mass stars, in fact, can live for much longer than the present age of the Universe, retaining in their atmospheres a record of the chemical abundances of the environment out of which they formed (Helmi 2008). If a top-heavy primordial IMF could prevent the existence of today living metal-free stars, the chemical feedback by the first stellar generations might allow long-living stars to be formed as soon as the gas metallicity $\geq Z_{cr}$. Therefore the most metal-poor stars represent the cosmic fossils of the early epochs, and their distribution in metallicity and abundance pattern may provide fundamental insight about the properties of the first stars.

On the other hand today living dwarf galaxies may provide an indirect observational window on the early phases of galaxies formation as they are the stellar systems with the lowest total mass content $M \sim (10^7 - 10^9)M_{\odot}$. According to ΛCMD models indeed, low-mass haloes are predicted to be the first virializing objects; hence, if the gas is able to cool and collapse (Sec. 1.1.3), the onset of the star formation might be occurred in these galaxies a very high redshifts. As low-mass haloes are highly affected by both radiative and mechanical feedback, the properties and observed number of dwarf galaxies may be strongly shaped by such a early physical mechanisms.

1.5 Observational imprints in the Milky Way

The halo of our own Galaxy represents an excellent ambient to search for such a early feedback imprints, as is represents the oldest Milky Way (MW) component. Stars in the Galactic halo are rotation-less and diffuse, with an average metallicity $\sim 10^{-2}Z_{\odot}$. During the past years this stellar component has been greatly surveyed, leading to the detection of the most metal-poor stars today known, whose ages are consistent with 14 ± 3 Gyr (Cayrel et al. 2001; Hill et al. 2002), and 13.2 Gyr (Frebel et al. 2007).

Other than made by field stars the Galactic halo is composed by approximately 150 globular clusters and more that 30 dwarf satellite galaxies. Among the latter the so-called dwarf spheroidal galaxies (dSphs) are the most interesting cosmological systems; indeed they are usually dominated by old stars, and they lack of gas and recent star formation, meaning that their baryonic content probably suffered strong feedback processes along their evolution. As they are nearby MW companion, typically residing at distances $\lesssim 130$ kpc from the Galactic center (Tolstoy, Hill & Tosi 2009), they have been studied in great detail, and a huge amount of different data are nowadays available. During the past years a new class of dSphs, the ultra faint dwarfs (UFs), has been discovered by the Sloan Digital Sky Survey (SDSS). Their extremely low luminosity, $L_{tot} < 10^5 L_{\odot}$, makes these galaxies the most promising candidates to be the "survivors" of radiative feedback processes.

In this Section I will review the main observational results concerning the stellar halo, the dSph and the UF galaxies, along with the most puzzling questions arose from them.

1.5.1 Galactic halo stars

The Metallicity Distribution Function

One of the most important observational constraints that can be derived by surveying the stellar halo is provided by the distribution of the stellar metallicities, the so-called Metallicity Distribution Function (MDF). Traditionally, the iron-abundance is taken as a reference element to enable comparison of the metallicity of one star with another, quantified as [Fe/H]= $\text{Log}(N_{Fe}/N_H)_* - \text{Log}(N_{Fe}/N_H)_\odot$[2]. In the following we will assume the nomenclature introduced by Beers & Christlieb (2005, Table 1) that classified the stars on the basis of their iron content: [Fe/H]< -1 metal-poor (MP), [Fe/H]< -2 very metal-poor (VMP), [Fe/H]< -3 extremely metal-poor (EMP), [Fe/H]< -4 ultra metal-poor (UMP), and [Fe/H]< -5 hyper metal-poor (HMP).

An intrinsic problem that observers have to face in searching for very metal-poor stars pertain to their rarity. In the solar neighborhood indeed, [Fe/H]< -2 stars comprising no more that the $\sim 0.1\%$ of the stars within a few kpc of the Sun (Beers et al. 2005). Therefore an important feature of the surveys is an efficient procedure to select metal-poor candidates. Wide-angle, low-resolution, spectroscopic surveys, actually provide the most efficient means to identify metal-poor stars. The *HK survey* by Beers and colleagues (Beers, Preston & Shectman 1985, 1992) and the *Hamburg/ESO survey* (HES, Wisotzki et al. 2000, Christlieb 2003) are the two most important objective-prism surveys that have been used to select and collect large samples of such a precious stellar relics.

The HK cover an area of 2800deg^2 in the northern and 4100deg^2 in the southern hemisphere. Metal-poor candidates are identified in this survey on the basis of the observed strengths of their CaII K lines. As this screening is performed without knowledge of the stellar colors (*i.e.* temperatures), a large number of "mistakes" [Fe/H]> -1.5 stars are selected. This leads to the bi-modal character of the metal-poor candidates MDF, which is presented in Fig. 1.3 (left panel). The HK sample counts ~ 1200 stars with [Fe/H]< -2 and ~ 140 with [Fe/H]< -3.

The HES survey, which covers a region of the southern sky not sampled by the HK, offers the opportunity to greatly increase the number of EMP stars reaching about two magnitude deeper ($10.0 \lesssim B \lesssim 17.5$) than the HK survey ($11.0 \lesssim B \lesssim 15.5$), and selecting metal-poor candidates by using quantitative criteria including automatic spectral classification (Christlieb, Wisotzki & Grasshoff 2002). In this survey the strength of the CaII K line is determined by using the measured KP line index

---

[2] Where N_{Fe} (N_H) is the number of iron (hydrogen) atoms and $\text{Log}(N_{Fe}/N_H)_\odot$ is the solar abundance by Anders & Grevesse (1989).

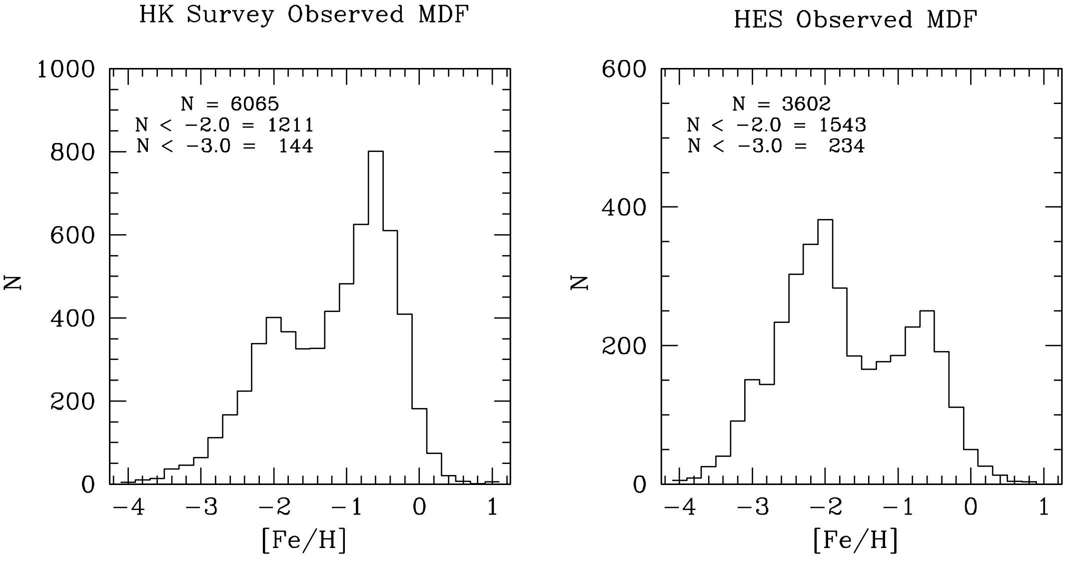

Figure 1.3: Metallicity distribution function for the selected metal-poor candidates in the HK survey (*left panel*) and the HES survey (*right panel*) by Beers & Christlieb (2005).

(Beers et al. 1999). Stars are selected as metal-poor candidates if their CaII K lines are weaker than expected from the measured $(B-V)$ colors, and their estimated metallicities are [Fe/H] $\lesssim -2.5$ (Beers & Christlieb 2005). The latter criteria may introduce a bias above [Fe/H]> -2.5. The HES sample counts 1543 stars with [Fe/H]< -2 and 234 with [Fe/H]< -3 (Fig. 1.3 right panel).

Thanks to its highly selective criteria, the HES survey has recently revealed the existence of the three most iron-poor stars already known with [Fe/H]$= -4.8$ (HE0557-4840, Christlieb 2008), [Fe/H]$= -5.7 \pm 0.2$ (HE0107-5240, Christlieb et al. 2002, 2004, 2008) and [Fe/H]$= -5.4$ (HE1327-2326, Frebel et al. 2005). As we will discuss later all of these ultra iron-poor stars exhibit a large overabundance of carbon, nitrogen and oxygen with respect to iron and other heavy elements.

With the inclusion of the latter, the joint HK and HES sample consist of 2757 stars with [Fe/H]≤ -2; higher metallicity stars are excluded from the sample because of the bias introduced by the adopted selection criteria and because of the possible contamination by disk stars. This function, which is shown in Fig. 1.4, has represented up to now the “official” MDF; in the following we will refer to this whenever talking about Galactic halo MDF. The huge amount of stars in the sample unable to clearly define the MDF shape, which is hopefully related with the properties of the first stellar generations. The function exhibits a maximum at [Fe/H]≈ -2, as also pointed out in the early studies by Ryan & Norris (1991) and Carney et al. (1996), it rapidly declines at lower iron-abundances, finally crowning

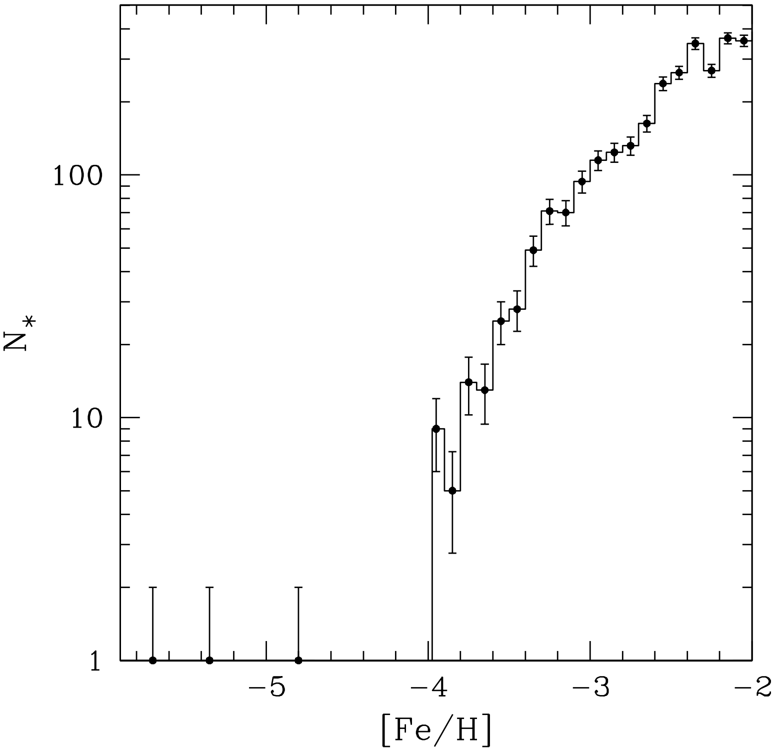

Figure 1.4: Metallicity distribution function of the joint HK and HES survey. Error bars are computed assuming a Poissonian distribution.

in a sharp cutoff at [Fe/H]~ -4. A low-[Fe/H] tail, made by three isolated stars, extends down to [Fe/H]≈ -5.7 but no stars are found in the "metallicity desert", $-4.8 <$[Fe/H]< -4. Does the sharp cut-off put constraints on the primordial IMF or/and on the Z_{cr} value? What are the implications of the low-metallicity tail? We have to note that the stars collected in this sample only cover a small region of the Galactic halo, located within $\lesssim 20$ kpc of the Sun (Beers et al 2005). One can ask himself if this sample is representative of the Galactic halo and if the MDF shape changes at increasing galactocentric radii.

Very recently Schörck et al. (2009) have revised the HES sample for the minor biases introduced by the selection strategy. The most important correction pertains to the rejection of carbon-enhanced stars on the basis of their GP index. According to Cohen et al. (2005) indeed, the CH lines present in the continuum bands lead to a systematic underestimation of the KP index, and hence of the inferred [Fe/H] values. Although the three UMP/HMP stars are not excluded by this correction, this entails a strong reduction in the number of [Fe/H]< -3 stars. As we will see in the next Section indeed, the fraction of carbon-enhanced stars strongly increases at decreasing [Fe/H] (Cohen et al. 2005; Lucatello et al. 2006). As a consequence the sharp cutoff is shifted toward [Fe/H]$= -3.6$, and except for the three UMP/HMP stars only 2 stars with [Fe/H]$= -4.1$ "survive" below such a threshold (see Fig. 12 of Schörck and collaborators).

Finally, though not originally planned as a stellar survey, the publicly available database of stellar spectra and photometry from the Sloan Digital Sky Survey (SDSS[3], York et al. 2000) contains more than 100 million stars (and galaxies), many of which are metal-poor. This survey covers about one-quarter of the celestial sphere in the northern Galactic hemisphere (Ivezic et al. 2008), including stars located up to 100 kpc from the Galactic center. SDSS stellar spectra are of sufficiently high quality to provide kinematic informations and robust stellar parameters. Recently Carollo et al. (2007) performed an accurate kinematic study of ~ 10.000 calibration stars, finding that the Galactic halo can be divided in two structural components, exhibiting different spatial density profiles, stellar orbits, and metallicity: an "outer" halo, located at $r \geq 15-20$ kpc, and an "inner" halo, $r < 10-15$ kpc. In particular they found that the outer halo includes a larger fraction of [Fe/H]< -2 stars and peaks at lower metallicity than the "inner" halo does. This evidence poses new challenging questions about the physical origin of this segregation along with the variation of the MDF with galactocentric radius.

The first extension of the SDSS, which includes the program SEGUE (Sloan Extension for Galactic Exploration and Understanding) specifically targeted to collect very metal-poor stars, has now been completed (Beers et al. 2009). Hopefully in the very near future the data analysis will be published, eventually revealing new interesting results.

Stellar abundances

Different kind of questions and possible theoretical constraints arise from the the observed chemical abundances of metal-poor halo stars.

One of the most puzzling concern the abundance of lithium isotopes (^{7}Li and ^{6}Li). Since the first detection by Spite & Spite (1982), later confirmed by subsequent works (Spite & Spite 1984; Ryan, Norris & Beers 1999; Asplund et al. 2006; Bonifacio et al. 2007), a $^7\mathrm{Li/H} = (1-2)\times 10^{-10}$ abundance was deduced, *independent* of stellar [Fe/H]. The presence of such a ^{7}Li plateau supports the idea that ^{7}Li is a primary element, synthesized by Big Bang Nucleosynthesis (BBN) as predicted by the standard model (Sec. 1). The measured value, however, results of a factor $2-4$ lower than what expected from the BBN $^7\mathrm{Li/H} = 4.27^{+1.02}_{-0.83}\times 10^{-10}$ (Cyburt 2004), $^7\mathrm{Li/H} = 4.9^{+1.4}_{-1.2}\times 10^{-10}$ (Cuoco et al. 2004), or $^7\mathrm{Li/H} = 4.15^{+0.49}_{-0.45}\times 10^{-10}$ (Coc et al. 2004) whose predictions provide a perfect match of the data for *all* the lighter elements (Fields & Olive 2006). Why there exists such a discrepancy?

A more serious problem arose with ^{6}Li, for which the BBN predicts a value of $(^6\mathrm{Li/H})_{\mathrm{BBN}} \sim 10^{-14}$. Owing to the small difference in mass between ^{6}Li and ^{7}Li

---

[3] http://www.sdss.org.

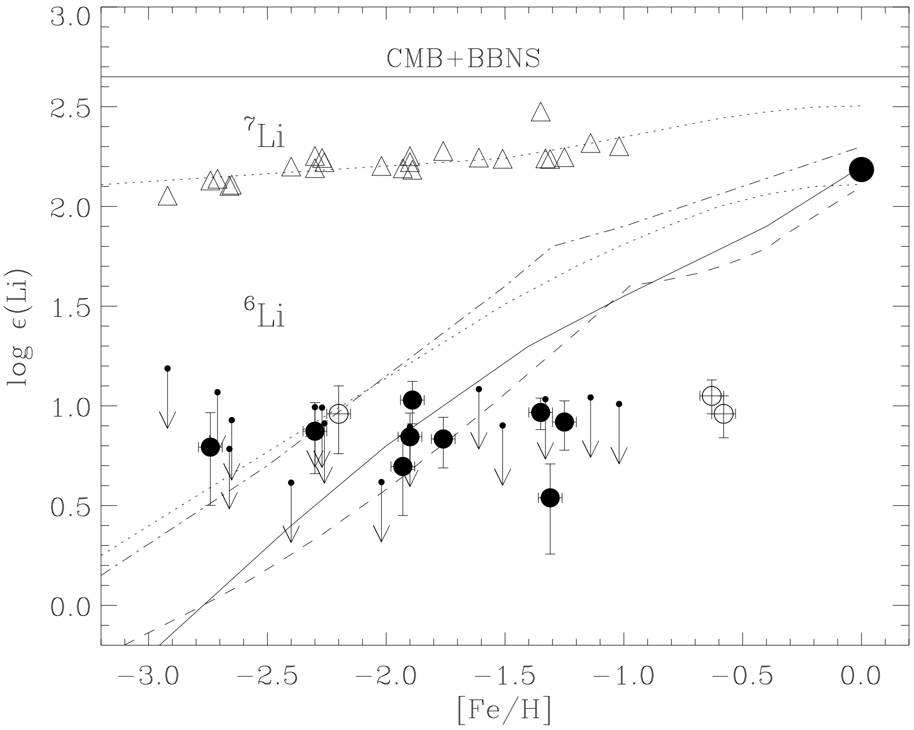

Figure 1.5: Observed logarithmic abundances of ^{7}Li (open triangles) and ^{6}Li (filled circles) as a function of [Fe/H] by Asplund et al. (2006); arrows denote 3σ upper limits to the ^{6}Li abundances. Also shown by open circles are the ^{6}Li detections in the halo turnoff star HD 84937 (Smith et al. 1993, 1998; Cayrel et al. 1999) and in two Galactic disk stars (Nissen et al. 1999). The large circle corresponds to the solar system meteoritic ^{6}Li abundance (Asplund et al. 2005). The horizontal solid line is the predicted ^{7}Li abundance from BBN. The curves are the abundance values by different theoretical models. See Asplund et al. 2006 for details.

lines, these two isotopes blend easily and the detection of ^{6}Li results quite difficult since the predominance of ^{7}Li. Recently, high-resolution spectroscopic observations measured the ^{6}Li abundance in 24 MP Galactic halo stars (Asplund et al. 2006, Fig. 1.5), revealing the presence of a plateau with abundances $^{6}\text{Li/H}= 6\times10^{-12}$, *i.e.* 2 orders of magnitude higher than what expected by the BBN. Again, a primordial origin of ^{6}Li is favored by the presence of the plateau while the high observed value cannot be reconciled with this hypothesis. What is the origin of the ^{6}Li? Was it synthesized in the early Universe or later, during the formation of the Galaxy?

Different kind of questions have been opened by measuring the abundances and scatter of heavy elements in Galactic halo MP stars. Cayrel et al. (2004) analyzed 35 giant stars with [Fe/H]< -2.5, founding that the scatter of several element ratios (e.g. [Mg/Fe], [Ca/Fe], [Cr/Fe] and [Ni/Fe]) is extremely small. The result is particularly impressive for the case of [Cr/Fe] in which the spread is consistent with zero, given the likely errors associated with the observations and analysis. These features has been confirmed by Cohen et al. (2004) which analyzed 28 dwarfs. A possible implication of these results is that the abundance pattern of VMP stars do not reflects the nucleosynthesis products of only few or even a single SN, but rather the integrated yields of many of them. In other words, VMPs probably formed in a well-mixed ISM enriched by *several* stellar generations.

On the other hand, VMP stars exhibit a large scatter in the carbon abundance. The HK and HES surveys have revealed that $\sim 20\%$ of the stars with [Fe/H]< -2 have a carbon excess of [C/Fe]$> +1.0$ (Beers & Christlieb 2005). Interesting, this percentage increases up to $\sim 40\%$ for [Fe/H]< -3.5, implying that the probability of a MP star to be carbon-enhanced is higher at decreasing [Fe/H]. Both the high carbon excess and the [Fe/H] anti-correlation are quite difficult to be explained and to be reconciled with the extremely small scatter of heavy element abundances. Does the carbon reflects the chemistry of the ISM from which stars formed or was it later produced and/or acquired?

Finally in the two HMP stars the carbon (and nitrogen) excess with respect to iron and to other heavy elements becomes really huge, both of them having [C/Fe]$\sim +4$ (Christlieb et al. 2002,2004; Bessel, Christlieb & Grasshoff 2004; Frebel et al. 2005; Aoki et al. 2006). Apart from their C, Ca and Fe values, which are quite similar, these stars exhibit very different abundances of heavy elements (see Fig. 8 by Beers & Christlieb 2005); however none of them show the strong odd-even effect predicted for the yields of SN$\gamma\gamma$. What's the origin of these stars? Answering this question will first require to understand if their low iron-abundance value reflects that of the ISM from which they were formed.

1.5.2 Dwarf spheroidal galaxies

Different kind of physical processes, mainly related with the role of feedback and the progressively evolution of our own Galaxy, can be explored by using the observations of the dSph galaxies, satellites of the MW. Today available data are discussed in the following by dividing those collected for the "classical", $L_{tot} > 10^5 L_\odot$, and ultra faint dSphs, $L_{tot} \leq 10^5 L_\odot$ (UFs).

Classical dwarfs

Nearby classical dSphs have been studied since many decades. However, only during the past years a huge amount of high-quality data have been collected, thanks to instrumentation and telescope improvements: the advent of new generation of wide-field multi-fibre spectrographs on 6-8m-class telescopes (VLT/FLAMES and Magellan/MIKE) has allowed to determine high-quality kinematic *and* metallicity data for a large number of stars but also high-resolution spectra of individual stars;

the new generation of telescopes (particularly the Hubble Space Telescope HST) and detectors, have provided accurate photometry of individual stars in crowded fields of external galaxies, allowing detailed Color-Magnitude Diagrams (CMD) to be derived (Tostoy, Hill & Tosi 2009). Such a profusion of data strongly contrast with the lack of a comprehensive scenario explaining the formation and evolution of these puzzling galaxies.

DSphs represent the most dark matter-dominated systems known in the Universe. Observationally, the mass content of dSph galaxies is derived by measuring the velocity dispersion profile of their stellar populations and comparing it with the predictions from different kinematic models. Nowadays, samples of hundred of stars out of the tidal radius are available for several dSphs (Wilkinson et al. 2004; Tolstoy et al. 2004; Munõz et al. 2005; Kleyna et al. 2005; Walker et al. 2006a,b; Battaglia et al. 2006,2008a) revealing high stellar velocity dispersions $\sim 8-15$ km s^{-1} (Tolstoy, Hill & Tosi 2009), that remain approximately constant at increasing distances from the dSph center (Walker et al 2007). If it can be assumed that this velocity dispersion is not caused by tidal processes, this result implies that dSphs contain a significant amount of dark matter (Mateo 1994; Olszewski 1998; Gilmore et al. 2007) with mass-to-light ratios ranging between $M/L \sim 10-300$.

Recently Walker et al. (2007) have presented velocity dispersion profiles for seven dSph satellites. According to this study the mass enclosed within 0.6 kpc, *i.e.* the region common to all data sets, is $M_{0.6} = (2-7)\times 10^7 M_\odot$. Does this result suggests that dSphs might have a common mass scale as claimed by other studies (Gilmore et al. 2007; Wilkinson et al. 2006; Strigari et al. 2008)? Battaglia et al. (2008b) pointed out that $M_{0.6}$ is very insensitive to the *total* mass of dSphs (see their Fig. 3, right panel). Once assumed a NFW density profile, for example, the extrapolated virial mass resides in the broader range $M_{vir} \sim (1-40)\times 10^8 M_\odot$ (Walker et al. 2007; Battaglia et al. 2008b), which is consistent with the DM mass enclosed within the last-measured point ($r_{least} = 1.8$ kpc) in Sculptor $M = 3.7\pm 0.7\times 10^8 M_\odot$ (Battaglia et al. 2008a).

Observations of gas content in dSph galaxies are much more solid. In none of them HII, and diffuse X-ray emission have been observed (Mateo et al. 1998), and Sculptor is the only one with detectable HI (Knapp et al. 1978; Carignan et al. 1998). If the HI emission can be really associated with this galaxy (doubts about a possible external origin still persist), a neutral hydrogen mass of $M_{\rm HI} \geq 3\times 10^4 M_\odot$ is inferred (Carignan et al. 1998) which is quite small given the total stellar mass content of this galaxy, $M_* = 5\times 10^6 M_\odot$. What is the cause of gas exhaustion? Which kind of feedback process drives it?

More puzzling questions pertaining the dSphs star formation histories (SFHs). These are inferred by measuring their detailed stellar CMD, as they preserve the imprint of fundamental stellar evolutionary parameters such as age, metallicity and IMF (Tolstoy, Hill & Tosi 2009). According with the measured CMD and related analysis dSphs appear to be characterized by very different SFHs. All of them

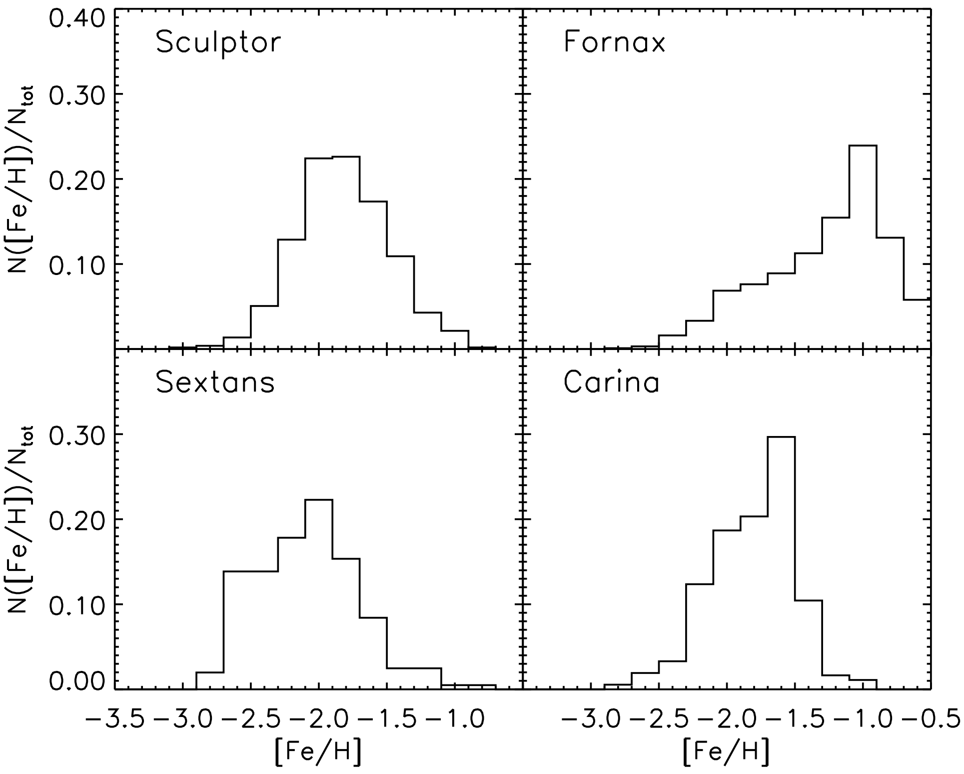

Figure 1.6: MDF observed in four nearby dSphs by the DART survey. See Helmi et al. (2006) for details.

exhibit an old stellar population, the majority being dominated by ancient stars (> 10 Gyr old), with a star formation activity concentrated during the first Gyrs (Dolphin et al. 2005). However Fornax, LeoII and Sagittarius show very different features: in these objects the bulk of the stars was formed much less than 10 Gyr ago and their star formation activity proceeds until $z \sim 1$, or even to lower redshifts (Grebel & Gallagher 2004). Carina exhibits a clearly episodic SFH, with a pause of several Gyrs after the old population formed and a massive formation of stars younger than 10 Gyr (Smecker-Hane et al. 1994, Hurley-Keller, Mateo & Nemec 1998). Can photoionization help in explaining such a variety of SFHs or do we need to invoke local processes, such as mechanical feedback, tidal stripping and gas infall? If reionization cannot play the game (Grebel & Gallagher 2004), how local feedback processes can act so differently in galaxies embedded in (apparently) so similar DM haloes?

The most challenging observational results has been obtained by the VLT/FLAMES DART survey (Tolstoy et al. 2006). This has determined for the first time the MDF in four nearby dSphs by using the empirical relation (Tolstoy et al. 2001) between

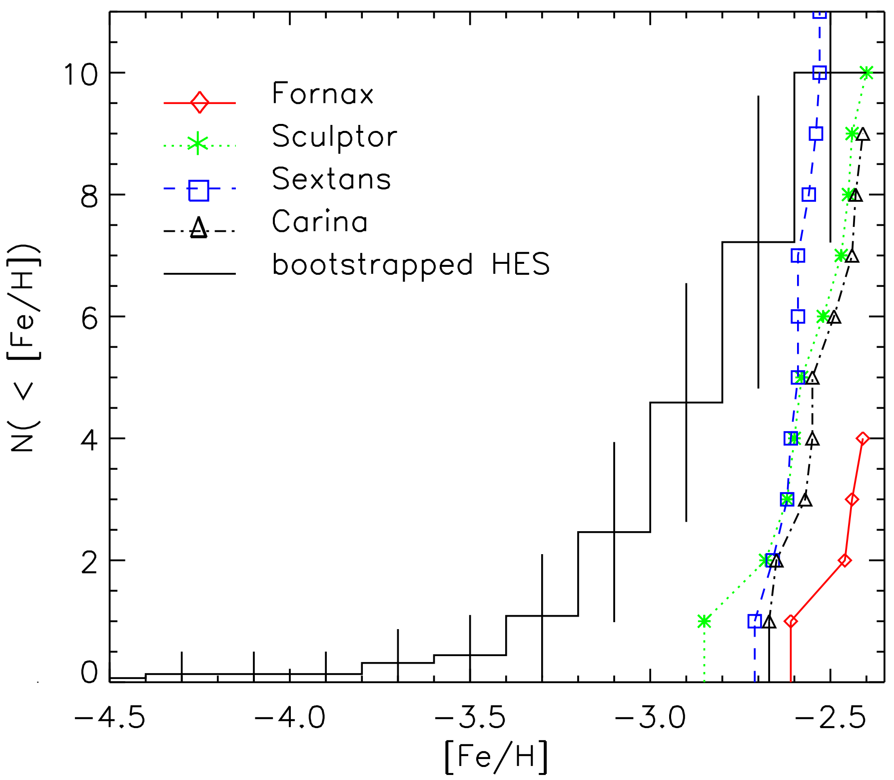

Figure 1.7: Comparison of the cumulative stellar MDFs: in the mean bootstrapped HES survey sample (histogram with error bars) and in the 4 dSphs from the DART survey (colored lines with points). The halo and dSphs MDF have been normalized at [Fe/H]$= -2.5$ where the HES survey is most likely to be complete. See Helmi et al. 2006 for details.

the equivalent width of the CaII triplet lines and [Fe/H] (Battaglia et al. 2006; Helmi et al. 2006). The MDFs tell us that dSphs are *lacking* of [Fe/H]< -3 stars (see Fig. 1.6). Such a result is particularly puzzling because dSphs are generally thought to be the today-living progenitors of the Galactic halo, which instead shows a well populated MDF below [Fe/H]< -3 (Sec. 1.5.1). An intrinsic problem of this observation is that the number of [Fe/H]< -2.5 stars observed in each dSphs is very low, typically of the order of 10, meaning that the lack of EMP stars should be an artifact of the sample size. The analysis performed by Helmi and collaborators excludes this possibility: by randomly selecting subsets of 10 stars among those with [Fe/H]< -2.5 in the HES sample[4], they derive the mean MDF (bootstrapped HES in Fig. 1.7) and compare it with the dSph ones. The discrepancies persist also when

---

[4] Because of the selection criteria the survey is most likely to be complete below such a [Fe/H] value, see Sec. 1.5.1.

the revised HES sample is used (Tolstoy, Hill & Tosi 2009). Finally, the validity of the empirical relation used to determine the stellar [Fe/H] has been tested in the low iron-abundance limit, [Fe/H]< -2.5 (Starkenburg et al. 2008), hence washing out the remaining possible observational error source. Where do Galactic halo EMP stars come from? Is the dSph birth environment pre-enriched or does the IMF behaves differently in Galactic building blocks and in dSphs at earliest times?

Finally, currently available observations of VMP stars in dSphs show that their chemical abundance is quite different with respect to Galactic halo stars (Venn et al. 2004; Tolstoy, Hill & Tosi 2009), implying that probably dSphs and Galactic halo progenitors are not the same. In particular the abundance of α-elements with respect to iron is challenging as dSphs stars have [α/Fe] ratios similar to those in the MW halo at low [Fe/H], but they gradually become [α/Fe] deficient at increasing iron-abundances, typically for [Fe/H]> -2 (Sbordone et al. 2007; Monaco et al. 2005; Shetrone et al. 2003; Geisler et al. 2005; Koch et al. 2008a). Can mechanical feedback and metal-enhanced winds help in explaining this observation?

Ultra faint dwarfs

Such entangled puzzle, made by a huge amount of observational pieces so far escaping any global theoretical interpretation, is now further complicated by the discovery of a new class of dwarf satellite galaxies: the Ultra Faint dSphs (UFs).

UFs are the least luminous galaxies known, with a total luminosity $L \approx 10^{3-5} L_\odot$; spectroscopic follow-up has revealed that they are highly dark matter dominated systems $M/L > 100$ (Simon & Geha 2007; Geha et al. 2009). Their average iron-abundance is $\langle[\mathrm{Fe/H}]\rangle < -2$ (Kirby et al. 2008) *i.e.* they represent the most metal-poor stellar systems ever known; although more data are required to solidly constrain stellar populations in these systems, at the moment *all* of them appear to be dominated by an old stellar population (Walsh, Willman & Jerjen 2008), with the only exception of LeoT (de Jong et al. 2008). In addition, UFs are relatively common in the MW system, representing more than 50% of the total number of dSph companions discovered so far ($N \approx 23$); hence, they are not peculiar objects. When and how did UFs form?

The [Fe/H]-Luminosity relation derived for UFs (Kirby et al. 2008) constitutes an extension toward lower metallicity of that of “classical” dSphs (Fig. 1.8). Such a continuous trend seems to exclude that processes (e.g. tidal stripping) different from those shaping the relation for classical dSphs become dominant in these objects. However, while dSphs and UFs together span more than four orders of magnitude in luminosity, their total mass is roughly the same $M \approx 10^7 M_\odot$ within the innermost 300 pc (Strigari et al. 2008, Li et al. 2009). Why is the star formation so inefficient in UF satellites? Does radiative feedback play a crucial role in determining the properties of these objects? The extremely low stellar mass content of UFs makes them the best objects to investigate the early cosmic star formation.

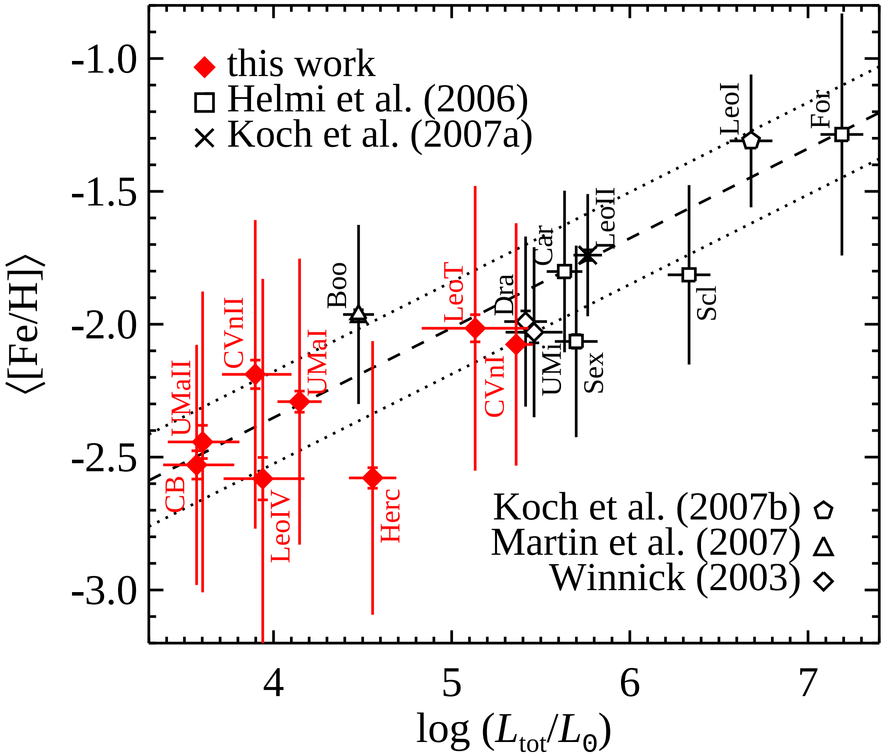

Figure 1.8: Mean [Fe/H] of MW dSphs as a function of their total luminosity by Kirby et al. (2008). The sources of [Fe/H] measurements are indicate in the figure. The full vertical lines error bars are the rms dispersion of [Fe/H] within a single galaxy, while the horizontal ones are the errors on ⟨[Fe/H]⟩. The luminosity are by Mateo et al. (1998) for all the classical dSphs and by Kirby et al. (2008) for the UFs (red points), with the exception of Boo (Martin et al. 2008).

In principle their observed features can be used to constraints the minimum halo mass to become luminous galaxies, $M_{sf}(z)$, along with the early SF efficiency, thus eventually reconciling the missing satellites problem.

However the global puzzle is made even more intriguing by the observation of metal-poor stars in UFs. In Fig. 1.9 we report the total MDF by Kirby et al. (2008) for the 8 ultra faint dSphs they analyzed. This observation shows the existence of a [Fe/H]< -3 stellar population in UFs, in contrast with the results for classical dSphs, that are lacking of extremely iron-poor stars. We also note that the ultra faint MDF is shifted toward lower [Fe/H] value with respect to that of classical dSphs, the effect being particularly evident when the most luminous ultra faint (CVnI) is excluded from the sample. What these features imply? Do they reflect a different origin of UF and classical dSphs?

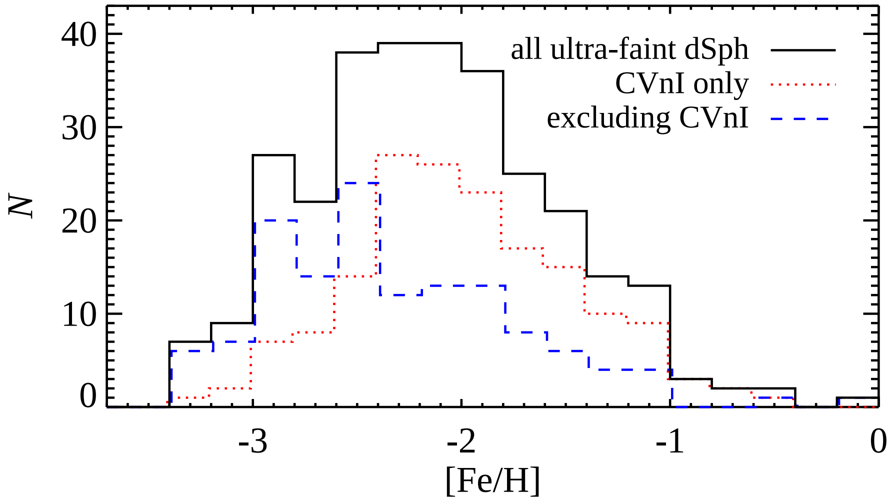

Figure 1.9: Combined MDF for all the 8 ultra faint dSphs observed (black histogram), for the most luminous one *i.e.* CVnI (red dotted histogram), and for all the UFs except CVnI (dashed blue histogram). See Kirby et al. (2008) for details.

The abundance pattern of (very) few stars in 3 UF dSphs has been derived only very recently (Koch et al. 2008b; Frebel et al. 2009). Noticeably, the elemental ratios of EMP stars in the two fainter dwarfs, UMa II and Coma, are remarkably similar to those observed in Galactic halo EMP stars. Are UFs the "true" progenitors of the MW halo?

1.6 Thesis purpose and plan

The properties of the first stars and the early galaxy formation processes are the main topic of this Thesis. Their investigation will be carried out through a systematic comparison of the Local observations with results of a Monte Carlo code, GAMETE (GAlaxy MErger Tree & Evolution), which I have developed during my PhD studies. It represents a cosmological bridge to connect the physical processes acting at high redshifts with observations in our Galaxy. After having reconstructed the hierarchical merger history of a MW-size dark matter halo, the code will allow us to follow the stellar populations history and the chemical evolution of the gas along the hierarchical trees, with the inclusion of some of the most relevant feedback effects. The features of the early Universe will be explored by comparing the Local observations with our results at $z = 0$.

In Chapter 2 the model will be presented. First I will describe two possible methods for the reconstruction of the hierarchical merger history of the Milky Way

(Sec. 2.1): the N-body approach by Scannapieco et al. (2006), which provides the informations about the spatial distribution of dark matter haloes (and particles); our semi-analytical approach based on the Press & Schechter theory (Sec. 1.1.2), which allows to build-up a statistically significant sample of possible hierarchical merger histories. Then, Sec. 2.2, I will describe how we model the star formation and chemical enrichment history of the MW along its hierarchical tree, exploring in details the assumptions we made and the procedure used to calibrate the model (Sec. 2.3). Finally I will present our results on the role of mechanical feedback during the MW formation and the consequent metal-enrichment of the MW environment (Sec 2.4). The subsequent Chapters are devoted to investigate the implications of the observational results presented in Sec. 1.5.

In Chapter 3 the impact of second generation stars in the Galactic halo MDF is analyzed, and some of the properties of Pop III stars are investigated by matching the observed sample. In Chapter 4 the age and metallicity distribution of MW halo metal-poor stars is explored as a function of Galactocentric distance. This will constraint the regions where VMP stars are more likely to be observed. In Chapter 5 we focus on the ^{6}Li problem within the context of the MW formation. One of the most promising solutions, *i.e.* the ^{6}Li production via high-energy cosmic rays accelerated by SN shocks, will be studied. The same cosmological approach, that is exploring the gradual formation of protogalactic haloes embedded in their own birth environment (the MW environment), will be particularly fruitful in the next two chapters, entirely devoted to dSphs. In Chapter 6 the formation and evolution of a prototypical dSph (Sculptor) is explored and most of the observed properties reproduced. In Chapter 7 the origin and main features of the newly discovered UFs are inferred by matching the observed Fe-luminosity relation along with the observed MDF. Finally (Chapter 8) I will summarize the results of this study and discuss their impact/implications on the present theoretical framework.

Chapter 2

Modeling the MW formation

2.1 Building the merger tree

We have seen that the most popular model for structure formation, the ΛCDM, predicts that galaxies form through a series of merging processes involving low mass fragments, in a hierarchical tree picture. In this Section we will focus on the dark matter component *only* and reconstruct the hierarchical history of the MW progenitor haloes, first by using the N-body simulation of Scannapieco et al. (2006), and then our semi-analytical model.

2.1.1 The N-body simulation

N-body simulations solve the evolution of the matter density field from first principles, without invoking either the linear perturbation theory nor the spherical top-hat model for the non-linear collapse. In these models indeed the density field is represented by the sum of a set of fictitious discrete particles, and its evolution is computed by solving the equations of motion of each one of them. This operation requires quite a lot of computational work. First, for each particle, the gravitational field due to all the others is solved; then the changes in particle positions and velocities over some small time step are computed and, according with these findings, particles are moved and accelerated; finally the gravitational field is re-calculated, and a new iteration starts.

Although there exist several methods allowing an efficient way of performing these operations, the number of particles that can be used is obviously limited by the computational cost. Therefore, the larger is the size of the simulation box, the bigger is the mass associated to each particle. Close encounters of spuriously massive particles can lead to wide-angle scattering, whereas the true physical systems are completely collisionless. To prevent collisions the gravitational force is usually *softened*, *i.e.* it is set to a constant value below some critical separation, ϵ. In other words N-body simulations are severely limited by mass resolution, which in turn limits the spatial resolution that can be achieved while modeling the evolution of the true collisionless fluid (Peacock 1993).

It is worth to point out that a complete description of the physical processes involved in the growth of the density field would require the inclusion of the dissipative baryonic component *i.e.* the combination of numerical hydrodynamics with N-body gravity. Clearly, the extra computational demands of treating fluids implies that the resolution achieved is inferior to a pure N-body code.

The main features of the N-body simulation that we will use in the 4-th Chapter of this Thesis are briefly summarize in the following. For a more detailed description we remind the reader to Scannapieco et al. (2006) and references therein.

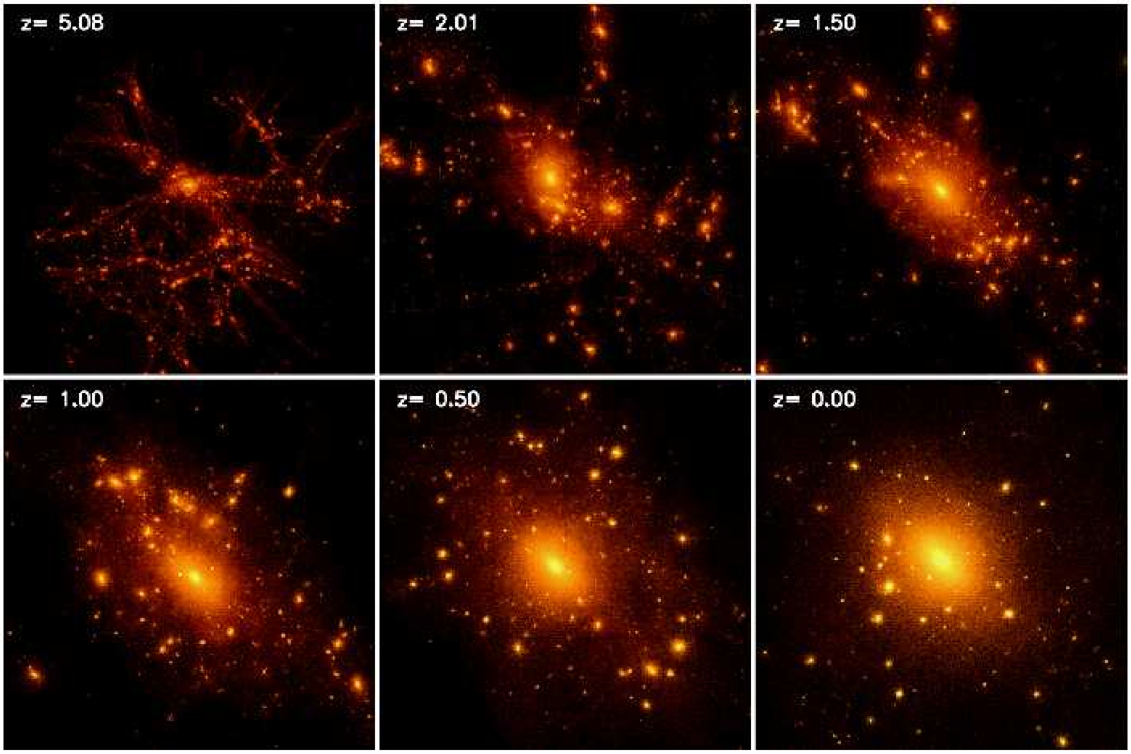

Figure 2.1: Formation of the MW-sized dark matter halo in the N-body simulation by Scannapieco et al. 2006. The panels show the evolutionary sequence of the dark matter particles at six different redshifts (gradually decreasing from left to right and from top to bottom), with intensity indicating the local matter density in logaritmic scale. Each box has a physical size of 500 kpc.

First of all, the initial conditions for the MW-size galaxy are fixed at $z = 56$, and constructed by using the public software GRAFIC2 (Bertschinger 2001). The simulation[1] is carried out with the GCD+ code (Kawata & Gibson 2003a), which uses

---

[1] A ΛCDM cosmological model with $h = 0.71$, $\Omega_0 h^2 = 0.135$, $\Omega_\Lambda = 1 - \Omega_0$, $\Omega_b h^2 = 0.0224$, $n = 1$ and $\sigma_8 = 0.9$ is adopted.

the tree algorithm by Barnes & Hut (1986) for the computation of the gravitational forces. This technique is based on the fact that, when computing the gravitational force acting on a given particle, one can ignore the detailed internal structure of distant groups of many of them. The volume of the simulation is recursively subdivided in cubic subcells and the force calculated by descending the hierarchical tree, achieving significant computational savings. In addition a "multi-resolution technique" (Kawata & Gibson 2003b) is used to reach high resolution in the regions of interest.

The low-resolution region is a $20h^{-1}$ Mpc diameter sphere selected from a low-resolution cosmological simulation, for which an isolated boundary condition is applied. The highest resolution region is a sphere with a radius four times the virial radius of the MW at $z = 0$. In this high-resolution region the dark matter particles mass and softening length are respectively $7.8 \times 10^5 M_\odot$ and 540 pc. The system consists on about 10^6 particles within r_{vir}; its virial mass and radius are respectively $M_{vir} = 7.7 \times 10^{11} M_\odot$ and $r_{vir} = 239$ kpc, roughly consistent with the observational estimates ($M_{vir} = 10^{12} M_\odot$, $r_{vir} = 258$ kpc) of the MW (Battaglia et al. 2005). The simulation data is output every 22 Myr between $z = 8 - 17$ and every 110 Myr for $z < 8$. At each output a *friend-of-friend* group finder (Davis et al. 1985) is used to identify the virialized DM haloes. This methods links recursively pairs of particles residing at distances lower than a fraction of the mean particle spacing, the linking parameter b. In this simulation $b = 0.15$; the threshold number required to identify linked particles as virialized haloes (groups) is fixed to 50. Once the virialized haloes have been identified their mass distribution can be derived for each redshift. Hence, by connecting the merging haloes, the hierarchical history is reconstructed. A low-resolution simulation including gas physics and star formation (SF) has been used in order to confirm that the initial conditions will lead to a disk formation. While gas physics is essential to reproduce the spatial distribution of disk stars, an N-body approach is suitable to investigate the halo (and bulge) population on which we will focus.

The panels in Fig. 2.1 show the evolutionary sequence for the formation of the MW-size dark matter halo provided by the N-body simulation. The filamentary structure of the growing dark matter perturbations is evident, especially at the highest redshifts $z > 3$. Within the intersection of these filaments we can observe the formation of DM haloes, the more massive ones residing within the connection regions of many of them. The build-up of the halo proceeds through a series of merging processes, particularly frequent during the early stages of the evolution. We note that many of the merging clumps survive until the present epoch in the form of "substructure". However, how many of them will actually become visible satellites crucially depends on the minimum halo mass to form stars and on the assumed star formation efficiency. We will come back to this point in Chapter 4 and Chapter 7.

2.1.2 The semi-analytical model

Conversely to N-body simulations semi-analytical models reconstruct the hierarchical merger tree by using the Press & Schechter formalism (Sec. 1.1.2), which combines the linear perturbation theory with the spherical top-hat model for the non-linear collapse. As highlighted in the Introduction indeed, the DM halo mass distribution drawn from this approximated approach shows an excellent agreement with those derived from N-body simulations, its main drawback consisting in the lack of spatial informations. The algorithms reconstructing hierarchical merger trees generically use semi-analytical approaches based on the so-called Extended Press & Schechter (EPS) theory (Bond et al. 1991; Lacey & Cole 1993). The latter revisits the Press & Schechter formalism by describing the DM halo formation in terms of trajectories of the linear density field. Such a different approach provide a key formula, allowing to describe the halo merging:

$$f(M, M_0)\, dM = \frac{1}{\sqrt{2\pi}} \frac{(\delta_c - \delta_{c0})}{(\sigma_M^2 - \sigma_{M_0}^2)^{3/2}} \exp\left(-\frac{(\delta_c - \delta_{c0})^2}{2(\sigma_M^2 - \sigma_{M_0}^2)}\right) \left|\frac{d\sigma_M^2}{dM}\right| \, dM. \qquad (2.1)$$

This equation gives the mass fraction within a halo of mass M_0 at redshift z_0 which, at an earlier time $z > z_0$, belongs to less massive progenitors having mass between M and $M + dM$ (see also Cole et al. 2000). The quantity $\delta_c = \delta_c(z)$ ($\delta_{c0} = \delta_c(z_0)$) is the critical linear overdensity threshold for collapse at redshift z (z_0); σ_M^2 ($\sigma_{M_0}^2$) is the linear r.m.s. density fluctuation smoothed with a top-hat filter of mass M (M_0). By construction, the integral of eq. (2.1) from $M = 0$ to $M = M_0$ must give unity, *i.e.* all haloes were in less massive fragments at earlier epochs. Multiplying $f(M, M_0)$ by M_0/M, the mass fraction can be translated into the number of haloes per unit mass:

$$\frac{dN}{dM}(M, M_0)\, dM = \frac{M_0}{M}\, f(M, M_0)\, dM. \qquad (2.2)$$

This equation represents the building block of all the algorithms that reconstruct the hierarchical merger history of a given DM halo[2]. Several alternative methods exist to develop the codes starting from this basic formula (see Somerville & Kolatt 1999 for a critical review). Following Cole et al. (2000) and Volonteri, Hardt & Madau (2003), we have developed a *binary* Monte Carlo algorithm with *mass accretion*.

The key equation representing the core of our code, is obtained by taking the limit $z \rightarrow z_0$ of eq. (2.2). This provides an expression for the average number of progenitors in the mass range M, $M + dM$, into which a halo of mass M_0 fragments considering a step dz back in time (Cole et al. 2000):

$$\frac{dN}{dM}\, dM = \frac{1}{\sqrt{2\pi}} \frac{1}{(\sigma_M^2 - \sigma_{M_0}^2)^{3/2}} \frac{M_0}{M} \frac{d\delta_c}{dz} \left|\frac{d\sigma_M^2}{dM}\right| \, dM\, dz, \qquad (2.3)$$

---

[2] Hereafter we will drop the argument (M, M_0) to simplify the notation.

where $M < M_0$ and $z = z_0 + dz$. Hierarchical trees are reconstructed by recursively using this equation to decompose any given DM halo (at any initial redshift) into its progenitors. Given the shape of the matter power spectrum in ΛCDM models, the number of haloes in the eq. 2.3 diverges as the mass M goes to zero. For this reason a cutoff, or resolution mass M_{res}, has to be defined. This quantity marks the transition between *progenitors* and *mass accretion*. At any given time-step, in fact, haloes can either (i) lose part of their mass, corresponding to the cumulative fragmentation into haloes with $M < M_{res}$, or (ii) fragment into two progenitor haloes and lose mass. At each redshift, the mass below the resolution limit accounts for the MW environment, or Galactic Medium (GM), which represents the ambient into which haloes are embedded. We will come back to it several times as it is one of the key ingredients of our model. Note that we are referring to *mass accretion* as the process of mass loss in the backward stepping merger algorithm since physically, *i.e.* going into the correct temporal way, this is what it really represents.

Once fixed M_{res}, one can compute the mean number of progenitors between $M_{res} < M < M_0/2$ that a halo of mass M_0 at z_0 is fragmented into during a time-step dz

$$N_p = \int_{M_{res}}^{M_0/2} \frac{dN}{dM}\, dM, \tag{2.4}$$

as well as the accreted mass fraction

$$F_a = \int_0^{M_{res}} \frac{dN}{dM} \frac{M}{M_0}\, dM. \tag{2.5}$$

Both these quantities depend on dz (see eq. 2.3) that has to be suitably chosen in order to prevent multiple fragmentations ($N_p < 1$) hence ensuring the binarity of the code. Since the number of progenitors decreases with dz, binary algorithms generally require a high temporal (redshift) resolution.

More practically our Monte Carlo code works as follow: at each time step and for each progenitor mass M_0, a random number $0 < R < 1$ is generated and compared with the value N_p derived by eq. (2.4). If $N_p < R$, the halo does not fragment at this step. However, a new halo with mass $M_0(1-F_a)$ is produced, to account for the accreted matter. On the contrary, if $N_p \geq R$ fragmentation occurs: a new random value in the range $M_{res} < M < M_0/2$ is drawn from the distribution in eq. (2.3) to produce a progenitor of mass M; mass conservation sets the mass of the second progenitor to $M_0(1 - F_a) - M$. This procedure, iterated on each progenitor halo and at each redshift, provides the whole hierarchical tree of the Milky Way, from the present-day up to $z = 20$[3]. Note that at every time and for each progenitor halo, the GM mass increases by a factor $M_0 \times F_a$, hence becoming more massive at higher z (see also the upper panel of Fig. 2.2).

---

[3] The developed algorithm is universal, meaning that it can be used to reconstruct the hierarchical tree of any given DM halo, from an initial redshift up to a final one.

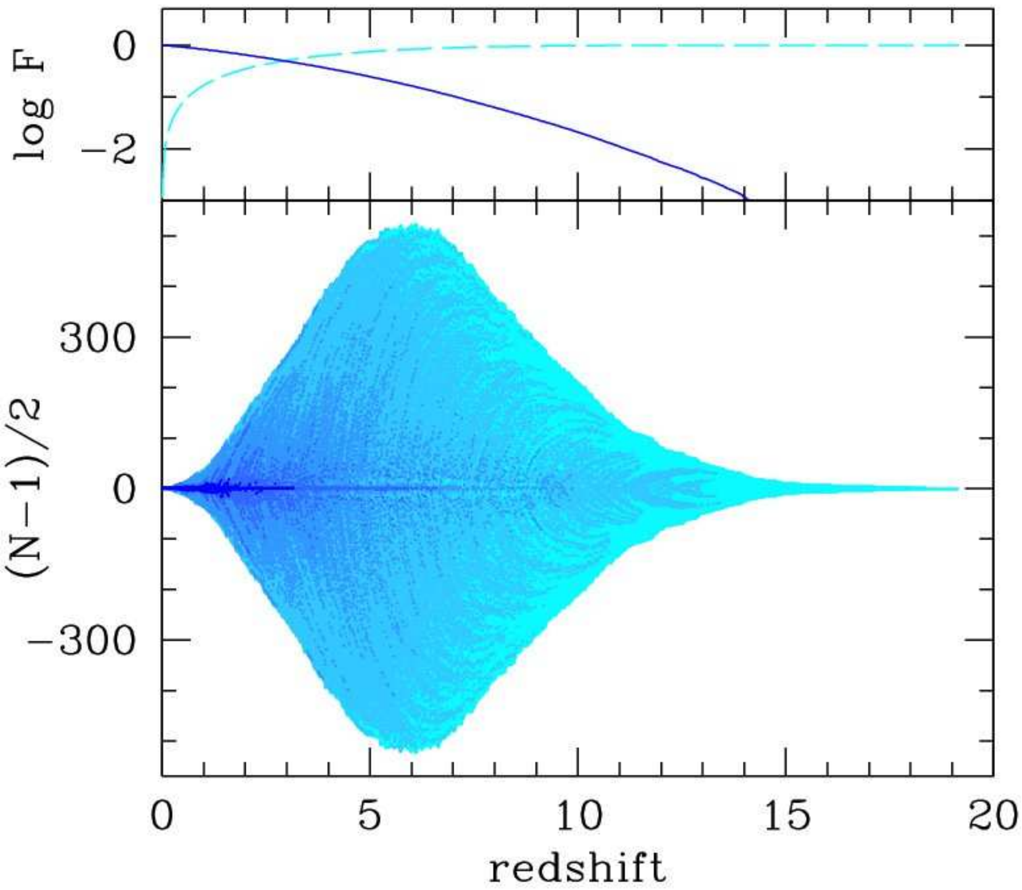

Figure 2.2: *Upper panel:* fraction of the total mass of the system contained in virialized haloes (solid blue line), and in the MW environment (dashed cyan line), as a function of redshift. *Lower panel:* evolution of the number of progenitor haloes in a typical merger history. The colors, from the lightest $10^7 M_\odot < M \leq 10^8 M_\odot$ to the darkest $10^{11} M_\odot < M \leq 10^{12} M_\odot$, identify haloes in different mass ranges logarithmically spaced.

We now need to specify the free parameters of the model, M_{res} and dz. A high value of M_{res} would be required to preserve the binarity of the code (eq. 2.4) and to control the computational cost implied by a very high time resolution. However, we need M_{res} to be small enough to resolve the low mass haloes that are presumably hosting the first stars. In addition, M_{res} must be redshift dependent, decreasing with increasing redshift, to better reproduce the EPS predictions at high z (Volonteri et al. 2003). The halo mass, corresponding to a virial equilibrium temperature T_{vir} at redshift z, can be derived from eq. 1.14:

$$M(T_{vir}, z) \sim 10^8 M_\odot \left(\frac{10}{1+z}\right)^{3/2} \left(\frac{T_{vir}}{10^4 \mathrm{K}}\right)^{3/2} . \tag{2.6}$$

where $\left[\frac{\Omega_m}{\Omega_m(z)} \frac{\Delta_c}{18\pi^2}\right] \approx 1$ in the analyzed redshift range. Given the above redshift dependence, taking $M_{res} \propto M(T_{vir}, z)$ appears physically motivated. In addition, for reasons that will be extensively discussed and motivated in the next Section, our analysis will predominantly focus on haloes with mass $M \geq M(T_{vir} = 10^4\mathrm{K}, z) \equiv M_4(z)$. Thus, we have chosen a resolution mass $M_{res}(z) = M_4(z)/10$ which enables to accurately follow the history of all MW progenitors having $M \geq M_4(z)$ up to $z = 20$. The time-step dz is empirically selected in order to obtain a good agreement between the EPS predictions and numerical results. We started by considering 820 time-steps logarithmically spaced in expansion factor between $z = 0$ and $z = 20$. However, since the number of haloes in the high mass range was found to exceed the EPS predictions, we have reduced the time-step by a factor 5 within the redshift interval $8 < z < 12$. Finally, we assume a MW dark matter halo mass of $M_{MW} = 10^{12}M_{\odot}$ (Binney & Merrifield 1998; Battaglia et al. 2005), consistent with the value adopted in the N-body simulation. The estimate by Battaglia et al. (2005) has been derived by using a sample of 240 distant halo objects, the 10% of which reside beyond 50 kpc, making this value robust.

The lower panel of Fig. 2.2 shows the evolution of the number, N, and typical masses (colors in the Figure) of the MW progenitors along the hierarchical tree. Two competitive processes regulate the evolution of N: the virialization of new haloes, which dominates at $z > 6$, and the halo merging, dominating at $z < 6$. When $z \approx 6$ the two processes balance themselves, and the number of progenitors reaches its maximum value $N \approx 1000$. The progenitors mass, instead, monotonically grows at decreasing redshifts as a result of (i) the merging processes, allowing the gradual build-up of more massive progenitors, (ii) the evolution of M_{res}, raising the minimum mass of newly virializing haloes. When $z > 15$, only few, small progenitors ($N < 50$, $M < 10^8 M_{\odot}$) have been already virialized, and about all the mass of the system is diffused into the GM (see the upper panel). When $z \lesssim 3$ the major branch of the hierarchical tree is formed ($M \lesssim 10^{11}M_{\odot}$), and the total mass collected in virialized haloes overcomes the diffused one. Minor merging will regulate the subsequent growth of such a most massive halo which, at $z = 0$, will contain all the mass of the system.

A comparison between the semi-analytical code results, the EPS predictions and the N-body simulation is provided in Fig. 2.3, where the expected number of Milky Way progenitors is plotted at different redshifts as a function of their dark matter mass. For the semi-analytical model the results have been obtained by averaging over 200 different hierarchical merger histories. At each redshift, the agreement among different model predictions is satisfactory down to the lowest halo masses $M \approx M_4(z)$, *i.e.* for all the objects of interest in our study. We observe again that the typical mass of the halo population decreases at increasing redshifts and only few collapsed haloes exist at $z = 15$, most of the mass being below the resolution limit and therefore diffused in the GM (upper panel of Fig. 2.2). It is important to note that the spread among distinct realizations of the semi-analytical model strongly increases with z, implying that at the higher redshifts the hierarchical histories are very different from each others. Indeed, the main advantage of semi-analytical models resides in providing a statistically significant sample of possible hierarchical merger histories, instead of a single, particular one.

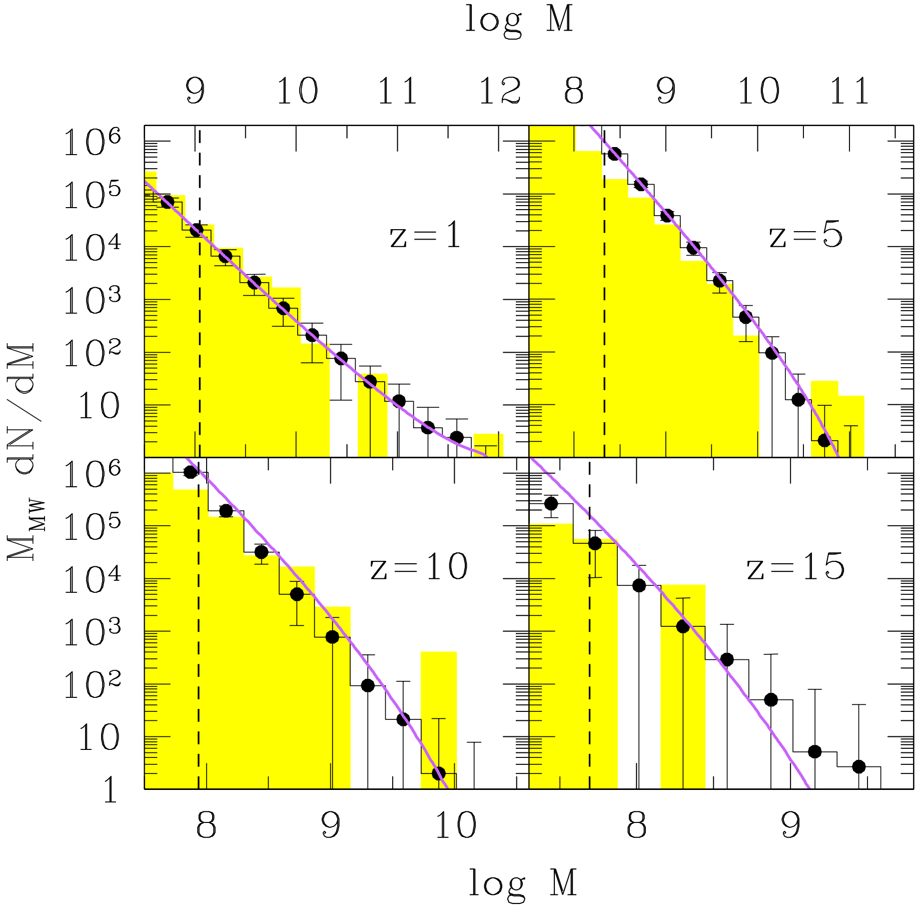

Figure 2.3: Number of progenitors of a MW parent halo of mass $M_{MW} = 10^{12} M_\odot$ as a function of mass at different redshifts. Black histograms with points and errorbars represent the results of the semi-analytical model and have been obtained by averaging over 200 realizations of the merger tree. Errorbars indicate Poissonian error on the counts in each mass bin. Shaded yellow histograms are the results of the N-body simulation. Solid lines show the predictions of EPS theory; dashed lines indicate the values of $M_4(z)$ at the corresponding redshift.

2.2 Including baryons

In order to finalize our theoretical model, GAMETE (GAlaxy MErger Tree & Evolution), we have to include baryons in the hierarchical picture we have just described. Such improvement is accomplished through the modeling of the star formation (SF) and feedback processes. In this Section the corresponding physical prescriptions/approximations are presented and motivated. Note that some of them will be relaxed or modified through the Thesis, and adopted thereafter, to capture more physical processes.

2.2.1 The mass of star-forming haloes

First of all we need to specify the minimum halo mass to trigger the SF, *i.e.* $M_{sf}(z)$. We pointed out that in ΛCDM models first stars are predicted to form in $T_{vir} < 10^4$ K *minihaloes*, collapsing at redshift $z \sim 20 - 30$. However, we recall that in these objects the gas cooling relies on the presence of molecular hydrogen, which is intrinsically poorly effective and can be easily photodissociated by radiative feedback (Sec. 1.3.1). As a consequence the minihalo SF activity is strongly reduced with respect to $T_{vir} > 10^4$ K galaxies, and it can be promptly suppressed, eventually helped by mechanical feedback (Sec. 1.3.2). It follows that the impact of minihaloes in the overall cosmic star formation history is very small.

Consistent with these findings, we have tracked the star formation history and chemical enrichment of the Galaxy down to progenitor haloes with masses $M(T_{vir} = 10^4\ \mathrm{K},\ z) = M_4(z) = 10^8 M_\odot[(1+z)/10]^{-3/2}$, *i.e.* we adopted $M_{sf}(z) = M_4(z)$. We have also assumed that at the initial redshift of $z \sim 20$ the gas in these haloes is still of primordial composition. This is the result of the effect that any given source photodissociates molecular hydrogen on scales much larger than those affected by its metal enrichment (Scannapieco et al. 2006).

2.2.2 Star formation efficiency

The initial gas content of all newly virialized dark matter haloes is assumed equal to the universal ratio, $M_g = (\Omega_b/\Omega_m)M$; such a quantity obviously decreases after each star formation event according to eq. 2.16. In any star-forming halo and at each time-step, stars are assumed to form in a single burst, and with a mass, M_*, proportional to the available gas mass, M_g, with a redshift-dependent global efficiency $M_* = f_*(z)M_g$. Star formation in gas clouds occurs in a free-fall time $t_{ff} = (3\pi/32G\rho)^{1/2}$ where G is the gravitational constant and ρ the total (dark+baryonic) mass density inside the halo (assumed to be 200 times denser than the background). Since, at each redshift, the Monte Carlo time step Δt (corresponding to dz) is $\Delta t \ll t_{ff}(z)$, it is possible to accurately sample time variations of the global star formation efficiency using the following approximation:

$$f_*(z) = \epsilon_* \frac{\Delta t(z)}{t_{ff}(z)}, \tag{2.7}$$

where ϵ_*, physically corresponding to the "local" star formation efficiency, represents a free parameter of the model.

2.2.3 The Initial Mass Function

According to the critical metallicity scenario (Sec. 1.2.3) we have assumed that the stellar IMF depends on the initial metallicity of the star forming clouds. Therefore, an halo with an initial gas metallicity $Z \leq Z_{cr}$, will be referred to as a Pop III halo[4] and it will host Pop III stars with masses within the range of $\mathrm{SN}_{\gamma\gamma}$, namely $140 M_{\odot} \leq m \leq 260 M_{\odot}$. As pointed out in the Introduction indeed, $\mathrm{SN}_{\gamma\gamma}$ provide the dominant contribution to metal enrichment at the lowest metallicities, releasing roughly half of their progenitor mass in heavy elements and leaving no remnants. As the Pop III IMF is completely unknown but metal-poor stars are expected to be very massive, $(30-300) M_{\odot}$, we simply assume a reference mass value equal to the mean $\mathrm{SN}_{\gamma\gamma}$ mass range, $m_{PopIII} = 200 M_{\odot}$. Nevertheless, the implications of adopting the two extreme values of $140 M_{\odot}$ and $260 M_{\odot}$, along with a universal Larson IMF will be also explored (see the next Chapter).

Conversely, if the initial metallicity exceeds the critical value, $Z > Z_{cr}$, the host halo is referred to as a Pop II/I halo and the stars are assumed to form according to a Larson IMF:

$$\Phi(m) = \frac{dN}{dm} \propto m^{-1+x} \exp(-m_{cut}/m), \tag{2.8}$$

with $x = -1.35$, $m_{cut} = 0.35 M_{\odot}$ and m in the range $[0.1 - 100] M_{\odot}$ (Larson 1998). Note that this function represents a modification of the Salpeter law defined in Sec. (1.3.3), which reproduces the observed present-day stellar population only for $m > 1\ M_{\odot}$; in the low-mass limit, in fact, the IMF behavior is still very uncertain because of the unknown mass-luminosity relation for the faintest stars. The Larson IMF matches the Salpeter law for $m > 1\ M_{\odot}$ while the cutoff at $m \sim 0.35 M_{\odot}$ can explain the absence of brown dwarfs in the observed stellar population, making it a better representation of today forming stars.

2.2.4 Instantaneous Recycling Approximation

Very massive Pop III stars are characterized by a fast evolution, reaching the end of their main sequence phase in $3-5$ Myr. Conversely, the broad mass range which characterizes Pop II/I stars implies a wide range of stellar lifetimes, $\tau_m \sim 10\ \mathrm{Gyr}/m^2$, which vary from a few Myr to several Gyr. In our model, we have initially[5] assumed the *Instantaneous Recycling Approximation* (IRA, Tinsley 1980), according to which stars are divided in two classes: those which live forever, if their lifetime is longer than the time since their formation $\tau_m > t(0) - t(z_{form})$; and those which die instantaneously, eventually leaving a remnant, if $\tau_m < t(0) - t(z_{form})$. The transition

---

[4] We define Pop III as all the stars with $Z \leq Z_{cr}$. In addition, Pop III stars are assumed to be massive if $Z_{cr} > 0$, and distributed according to a Larson IMF if $Z_{cr} = 0$.

[5] This is one of the assumptions that will be relaxed in Chapter 6

mass between the two possible evolutions, or turn-off mass $m_1(z)$, has been computed at any considered redshift. All stars having mass $m < m_1(z)$ represent stellar fossils which can be observed today. The turn-off mass is an increasing function of time since $[t(0) - t(z_{form})] \rightarrow 0$ when $z_{form} \rightarrow 0$; in this limit of course $m_1 \rightarrow 100 M_\odot$ *i.e.* all the stars are still alive. Using the IRA approximation at each time-step, we can compute the number of stellar relics per unit stellar mass formed:

$$N_* = \frac{\int_{0.1M_\odot}^{m_1(z)} \Phi(m)dm}{\int_{0.1M_\odot}^{100M_\odot} m\ \Phi(m)dm}, \tag{2.9}$$

and the equivalent mass fraction in these stars

$$f_{m*} = \frac{\int_{0.1M_\odot}^{m_1(z)} m\ \Phi(m)dm}{\int_{0.1M_\odot}^{100M_\odot} m\ \Phi(m)dm}. \tag{2.10}$$

By definition, there are no stellar fossils of Pop III stars in the $\mathrm{SN}_{\gamma\gamma}$ progenitor mass range.

2.2.5 Nucleosynthetic products

Massive stars can lose mass and heavy elements through stellar winds and supernova explosions. Using the IRA approximation, we can compute the *yield*, *i.e.* the mass fraction of metals produced per unit stellar mass formed,

$$Y = \frac{\int_{m_1(z)}^{100M_\odot} m_Z(m, Z)\, \Phi(m)\, \mathrm{d}m}{\int_{0.1M_\odot}^{100M_\odot} m\ \Phi(m)\mathrm{d}m}, \tag{2.11}$$

as well as the *returned fraction*, or the stellar mass fraction returned to the gas through winds and SN explosions:

$$R = \frac{\int_{m_1(z)}^{100M_\odot} (m - w_m(m))\, \Phi(m)\, \mathrm{d}m}{\int_{0.1M_\odot}^{100M_\odot} \Phi(m)\, m\ \mathrm{d}m}. \tag{2.12}$$

The quantity $m_Z(m, Z)$ represents the mass of metals produced by a star with initial mass m and metallicity Z, and $w(m)$ is the mass of the stellar remnant. Non-rotating Pop III stars in the $\mathrm{SN}_{\gamma\gamma}$ domain return all their gas and metals to the surrounding medium, *i.e.* $R = 1$. We have used for these stars the results of Heger & Woosley (2002) which have been described in Sec. 1.2.2. It is interesting to note that although the total metal yield is independent of the progenitor mass and equal to $Y = 0.45$, the iron yield strongly depends on that, being $Y_{Fe} = (2.8 \times 10^{-15}, 0.022, 0.45)$ for $m_* = (140, 200, 260)M_\odot$.

For Pop II/I stars we have used the grid of models by van den Hoek & Groenewegen (1997) for intermediate ($0.9M_\odot < m_* < 8M_\odot$) mass stars, and Woosley & Weaver (1995) for SNII ($8M_\odot < m_* < 40M_\odot$), linearly interpolating among grids of different initial metallicity when necessary. We have also followed the evolution of individual elements relevant to the present study, Fe and O.

2.2.6 Mechanical Feedback

As discussed in Sec. 1.3.2 supernova explosions may power a wind which, if sufficiently energetic, may overcome the gravitational pull of the host halo leading to expulsion of gas and metals into the surrounding GM. This mechanical feedback has important implications for the chemical evolution along the merger tree: the nucleosynthetic products of the first stellar generations can be efficiently ejected out of the shallower potential wells of the primordial star forming objects; then they can be accreted by neighboring haloes, and finally incorporated into the subsequent stellar populations. To model mechanical feedback, we compare the kinetic energy injected by SN-driven winds

$$E_{SN} = \epsilon_w N_{SN} \langle E_{SN} \rangle, \tag{2.13}$$

with the the hosting halo binding energy derived from eq. 1.12:

$$E_b = \frac{1}{2}\frac{GM^2}{r_{vir}} \sim 5.45 \times 10^{53} \mathrm{erg} \left(\frac{M_8}{h^{-1}}\right)^{5/3} \left(\frac{1+z}{10}\right) h^{-1} \tag{2.14}$$

where M is the total halo mass and $M_8 = M/10^8 M_\odot$. In the first equation, ϵ_w is the wind efficiency (*i.e.* the fraction of explosion energy converted into kinetic form); this represents the second free parameter of the model, the first being ϵ_* (see eq. 2.7). In the above equation N_{SN} is the number of SN in the burst and $\langle E_{SN} \rangle$ the average explosion energy, which we take to be equal to 2.7×10^{52} erg for $\mathrm{SN}_{\gamma\gamma}$ and to 1.2×10^{51} erg for SNII. We assume that ejection takes place when $E_{SN} > E_b$, and the gas is retained otherwise. The ejected fraction of gas and metals is computed as

$$\alpha_{ej} = (E_{SN} - E_b)/(E_{SN} + E_b) \tag{2.15}$$

meaning that it is directly proportional to the SN energy, provided it is larger than the binding energy. Note that, according to this simple prescription, gas and metals are ejected with the same efficiency. This might not necessarily be the case (Mac Low & Ferrara 1999; Fujita et al. 2004) as we will extensively discuss in Chapter 6; for the moment, however, we neglect this complication.

Due to mechanical feedback, the mass of gas and metals in a halo can decrease substantially. Following a star formation burst the mass of gas left in the halo, M_g, which represents the reservoir for subsequent star formation events, is related to the initial gas mass, M_g^{in}, and the stellar mass, M_*, by the following equation

$$M_g = [M_{gas}^{in} - M_* + RM_*](1-\alpha_{ej}) = M_{gas}^{in}(1 - f_* + Rf_*)(1-\alpha_{ej}) \ . \qquad (2.16)$$

Similarly, the final mass of metals can be computed as,

$$M_Z = [M_Z^{in}(1-f_*) + YM_*](1-\alpha_{ej}) = M_{gas}^{in}(Z_{in}(1-f_*) + Yf_*)(1-\alpha_{ej}). \ (2.17)$$

2.2.7 Metal mixing

The star formation and chemical enrichment history of our Galaxy is reconstructed by applying iteratively eqs. (2.16)-(2.17), together with eqs. (2.9)-(2.15), along the hierarchical tree. It is assumed that during a merger event the metal and gas content of two distinct progenitor haloes are perfectly mixed in the ISM of the new recipient halo. Similarly, metals and gas ejected into the GM are assumed to be instantaneously and homogeneously mixed (we refer to this approximation as "perfect mixing") with the gas residing in that component. The filling factor Q of the metal bubbles inside the volume corresponding to the size of the MW halo today, gives an estimate of the validity of the latter assumption, which is verified if $Q > 1$. A rough estimate of Q is given by:

$$Q(z) = (\frac{R_b(z)}{\langle\lambda(z)\rangle})^3 \qquad (2.18)$$

where R_b is the bubble radius and

$$\langle\lambda(z)\rangle = [\frac{V_{MW}(z)}{\frac{4}{3}\pi N(z)}]^{1/3} = [\frac{V_{MW}(0)(1+z)^{-3}}{\frac{4}{3}\pi N(z)}]^{1/3} \qquad (2.19)$$

is the average mean halo separation within the proper MW volume $V_{MW}(z)$, having assumed $V_{MW}(0) \sim 30$ Mpc^3; $N(z)$ is the total number of haloes at redshift z, averaged over 200 realizations of the merger tree. The value of R_b can be estimated from a Sedov-Taylor blastwave solution:

$$R_b(z) = [\frac{E(z)}{\langle\rho_b(z)\rangle}]^{1/5} t_H^{2/5}(z)$$

where $E(z)$ is the energy released by SN explosions within each halo, $\langle\rho_b(z)\rangle$ is the mean GM density and $t_H(z)$ is the Hubble time. If we assume that i) star forming haloes have $M_h(z) = M_4(z)$ and ii) $E(z) = E_0 f_*(z)\Omega_b/\Omega_m M_4(z)$ where $E_0 = 1.636 \times 10^{49} erg/M_\odot$ is the Pop II explosion energy per unit stellar mass formed, we find that $Q > 1$ when $z < 11$. Such limit implies that regions with $Z = 0$ are no longer present beyond that epoch. Additional discussion on this issue will be provided in Sec. 2.4.1.

2.3 Model calibration

Although we have kept our model to describe the star formation history and the chemical enrichment of the Milky Way along the hierarchical tree as simple as possible, it includes a number of relatively poorly known (albeit important) physical processes, that need to be empirically calibrated. To this aim we have used the observed properties of the Milky Way as a benchmark to fix the best values of the two model free parameters, ϵ_* and ϵ_w. In particular, we have compared the results of the simulations at redshift $z = 0$ with the following observations:

- *Gas metallicity.* The Galactic disk has a mean metallicity $Z_g \simeq Z_\odot$. As this component contains the majority of the MW gas, we use this value as representative of the whole system.
- *Stellar metallicity.* The typical mean value quoted for this quantity is $Z_* \simeq Z_\odot$. This value has been derived by weighting the mean metallicity of each galactic stellar component with its corresponding mass.
- *Stellar mass.* Contributions to the stellar mass come from the disk ($M_*^{disk} \approx (4-6)\times 10^{10} M_\odot$), the bulge ($M_*^{bulge} \approx (0.4-1)\ 10^{10} M_\odot$) and the halo ($M_*^{halo} \approx (0.2-1)\ 10^{10} M_\odot$) components (Dehennen & Binney, 1998; Brown et al. 2005), summing up in a total mass of $M_* \approx 6 \times 10^{10} M_\odot$.
- *Gas-to-stellar mass ratio*, $M_g/M_* = 0.1$. The mass of gas has been derived using the observed mass of HI and HII regions of the Galaxy, $M_g = M_{HI} + M_{HII} \sim (6+2) \times 10^9 M_\odot \sim 8 \times 10^9 M_\odot$ (Stahler & Palla 2004).

Moreover, if *mechanical feedback* is considered, two additional quantities become meaningful:

- *Baryon to dark matter ratio*, $f_b = (M_* + M_g)/M_{MW} = 0.07$. This number has been computed by adopting the afore mentioned values for M_* and M_g, and by taking $M_{MW} = 10^{12} M_\odot$ (Battaglia et al. 2005).
- *GM metallicity.* Although the exact value for this quantity is somewhat uncertain, high-velocity clouds (supposedly constituted by leftover gas from the Galactic collapse, and currently accreting onto the disk) may be used as a reasonable template. For these objects, Ganguly et al. (2005) derive [O/H]$\sim -0.66 \sim 0.25 Z_\odot$, a value that we take as an educated guess for Z_{GM}.

Obviously, in study cases in which mechanical feedback is turned off for comparison sakes, it follows that $Z_{GM} = 0$ and $f_b = f_c = \Omega_b/\Omega_m = 0.156$. In principle, an acceptable fit to the above MW properties can be achieved both for models including mechanical feedback and neglecting it (see next Sections). However, the best values of the free parameters are different in the two cases. We will show later how

model	$Z_g/Z_\odot$	$< Z_*/Z_\odot >$	$Z_{GM}/Z_\odot$	M_g/M_*	M_*/M_*^{MW}	f_b
$\epsilon_* = 0.5$, $\epsilon_w = 0$	1.26	1.13	$--$	0.11	1.71	$--$
$\epsilon_* = 0.7$, $\epsilon_w = 0.2$	0.93	1.01	0.41	0.11	0.85	0.085
observed values	1	1	0.25	0.1	1	0.07

Table 2.1: Averaged values of the global properties of the MW derived using the two best-fit models: no-feedback $\epsilon_* = 0.5$, $\epsilon_w = 0$, and feedback $\epsilon_* = 0.7$, $\epsilon_w = 0.2$. The values have been obtained averaging over 200 realizations of the merger tree. For comparison, we also quote the indicative observed values (see text).

it is possible to assess the role of feedback by using the properties of the observed Galactic halo metallicity distribution function. Note that the calibration procedure is *completely independent* of the assumed Z_{cr} and Pop III IMF.

2.3.1 Close-box vs feedback models

In the following we will describe the main results and implications of the calibration procedure we have obtained by applying GAMETE to 200 different hierarchical merger histories, semi-analytically computed. For this reason we will usually refer to mean values, obtained by averaging over the realizations. Note that, although the calibration procedure will be repeated whenever new features are implemented into the code, eventually providing different values of the free parameters (ϵ_*-ϵ_w), the results we are presenting about the role of mechanical feedback and the metal enrichment of the MW environment are universal.

In Fig. 2.4 we compare the observed global properties of the Galaxy with the results of our model for the no-feedback and feedback case, as a function of the star formation efficiency, ϵ_*. Let's start by analyzing the no-feedback case, meaning $\epsilon_w = 0$. A good overall agreement with the four observed quantities is obtained for relatively high values of $\epsilon_* > 0.1$. In fact, the derived values of $Z_g/Z_\odot$, $Z_*/Z_\odot$, M_*/M_*^{MW} rapidly increase when the star formation efficiency increases from $\epsilon_* =$ 0.01 to 0.1, and remain nearly constant thereafter (note that the value of M_g/M_* actually *decreases* with ϵ_* in this range). These trends can be understood very simply. The gas mass decreases due to star formation (eq. 2.16), forcing the gas fraction to decrease with increasing ϵ_*. Thus, M_* saturates beyond $\epsilon_* > 0.1$ because of the limited gas mass available. Given the proportionality between M_Z and M_* (eq. 2.17), $\langle Z_* \rangle$ shows the same behavior. Conversely, the mass of metals in the gas is determined by the balance between metals synthesized and ejected by stars, and metals locked into newly formed stars (eq. 2.17); when the second effect dominates, it produce a slight decrease of Z_g. The best-fit model requires a high star formation efficiency, $\epsilon_* = 0.5$[6]

---

[6] Because of the assumed star formation law (eq. 2.7), $\epsilon_* = 0.5$ is only the instantaneous star

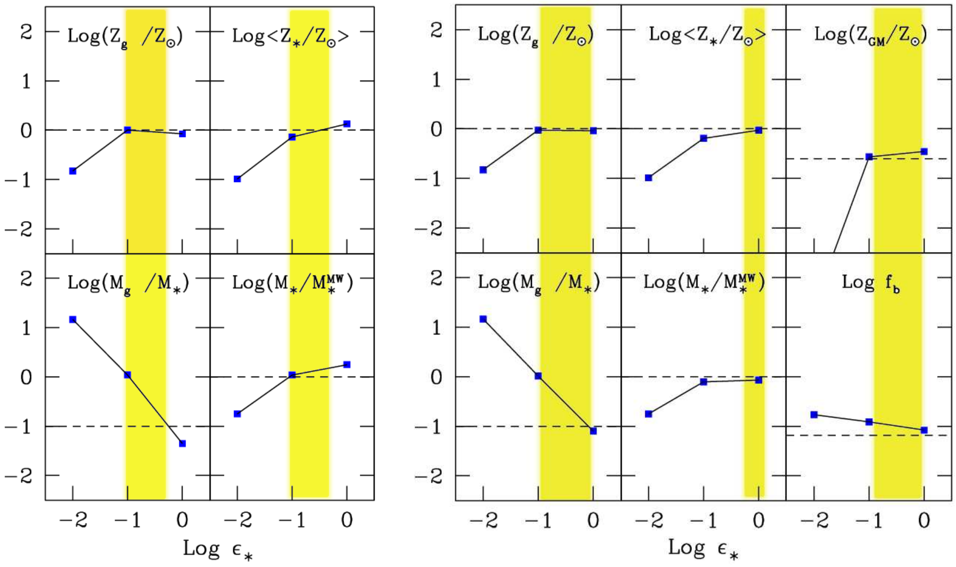

Figure 2.4: Global properties of the MW. Squared points are the main model results (averaging over 200 realizations) as a function of the star formation efficiency, ϵ_*. Error bars are not shown because negligible in the selected scale. Dashed lines represent the (typical) observed values. The shaded areas underline the ϵ_* range that provides a good reproduction of the observed properties. *Left panel*: no-feedback model ($\epsilon_w = 0$); *Right panel*: feedback model with $\epsilon_w = 0.2$.

In the right panel of Fig. 2.4, we show the global properties of the MW derived using a feedback model with $\epsilon_w = 0.2$. For low values of ϵ_*, the effect of mechanical feedback is negligible; similarly to the no feedback model $f_b \approx \Omega_b/\Omega_m = 0.16$, and $Z_{GM} \approx 0$. These results are coherent with our feedback prescriptions (eqs. 2.13 and 2.15) since the efficiency of mechanical feedback depends on the number of SN explosions and therefore on the level of star formation activity. As expected, f_b decreases with ϵ_* while Z_{GM} increases. Note that in the range $0.1 < \epsilon_* < 1$ the feedback model closely resembles the no-feedback one, the major difference being the lower saturation values for the stellar mass and metallicity. Instead, the metallicity of the gas is nearly unaffected because metals and gas are ejected into the GM with the same efficiency (see eqs. 2.16 and 2.17). The best-fit model requires $\epsilon_* = 0.7$ (we stress again that this is *not* the global star formation efficiency, expressed by $f_*(z)$, see eq. 2.7).

The values for the global properties of the MW derived by using the best fit models, with and without mechanical feedback, are summarized in Table 1 along with the reference observed values. Although the mechanical feedback case provides

---

formation efficiency and does not imply that half of the gas mass is converted into star in a single burst. Rather, for this model $f_*(z)$ varies from 6×10^{-4} to 4×10^{-2} in the considered redshift range.

a better agreement with the observed values, it is not possible to clearly discriminate among the two models by using the MW global properties only.

2.3.2 Accretion vs Self-Enrichment

This model degeneracy can be immediately broken by analyzing the properties of the total metallicity distribution function (MDF), *i.e.* the number of MW relic stars as a function of their iron abundance. In Fig. 2.5 (left panel) we compare the MDF derived by using the two best-fit models, with and without mechanical feedback (see Table 1), for the specific value $Z_{cr} = 10^{-4} Z_{\odot}$ and $m_{PopIII} = 200 M_{\odot}$.

The first striking difference is that no stars with [Fe/H] $\lesssim -1.5$ are produced in the no-feedback case, meaning that this model cannot account for range of stellar metallicity observed in the Milky Way. The reason for this result is that in closed box models the gas metallicity is not efficiently diluted. A simple estimate elucidates this point. Following a burst of Pop III stars, the gas metallicity of the host halo is raised up to

$$Z = \frac{M_Z}{M_g} = \frac{Y M_*}{M_g} = Y f_*(z) \gtrsim 0.146 Z_{\odot}, \tag{2.20}$$

where we have used $Y = 0.45$ and the smallest $f_*(z) \sim 6.5 \times 10^{-3}$ value corresponding to $\epsilon_* = 0.5$ (appropriate for the no-feedback case). Note that the final metallicity depends only on the metal yield and on the star formation efficiency. From the previous equation it is easy to see that the resulting abundance is[7]

$$\text{[Fe/H]} \simeq \log (Z/Z_{\odot}) - 0.257 \gtrsim -1.09$$

This value is larger than the low [Fe/H] cutoff in the distribution shown in Fig. 2.5. What is the reason for such discrepancy? In the absence of mechanical feedback, metals can only be diluted through mass accretion of metal-free gas and through mergers with unpolluted progenitors (which at most can halve the gas metallicity Z if they have a comparable mass). However, dilution purely provided by accretion of unpolluted gas is not sufficient to account for the low-Z tail of the MDF, which extends to values [Fe/H] ≈ -4, with three outliers at [Fe/H] < -4.8. The same conclusion is achieved using different mass values for SN$_{\gamma\gamma}$ or assuming a Larson IMF for metal free stars though,in both cases, the different value of the yields cause a shift in the MDF cutoff. For example for the Larson IMF ($Z_{cr} = 0$ model) $Y \sim 0.01$ and $Y_{Fe} \sim 5 \times 10^{-4}$ and the cutoff moves to [Fe/H]$\sim -2.44 \gg -4$. A similar result is obtained for $m_{PopIII} = 140 M_{\odot}$.

In conclusion *mechanical feedback is required* to effectively dilute metals inside haloes, *independently* of the Z_{cr} value and of the assumed PopIII IMF. Heavy el-

---

[7] This relation follows from the definition of [Fe/H] that leads to [Fe/H]$= \log (Z/Z_{\odot}) + 1.044 + \log (Y_{Fe}/Y_Z)$, where for Pop III stars with $m = 200 M_{\odot}$ the iron yield is approximately $Y_{Fe} = 0.05 Y$.

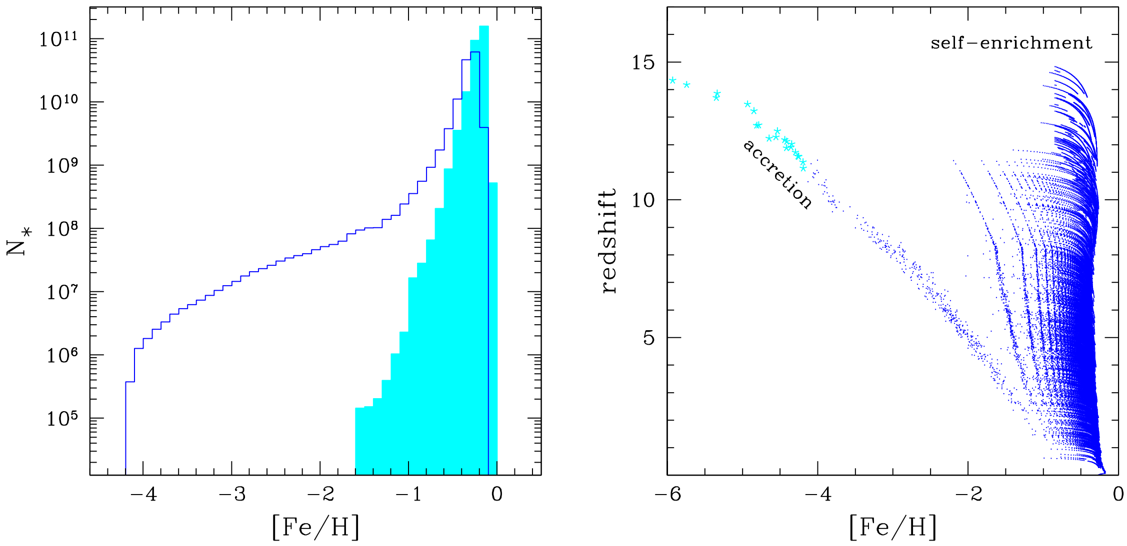

Figure 2.5: *Left panel:* MDFs derived using the no-feedback model (shaded histogram), and the fiducial feedback model (unshaded) both summarized in Table 1. Histograms have been obtained as average over 200 realizations. Both models assume $Z_{cr} = 10^{-4} Z_\odot$ and $m_{PopIII} = 200 M_\odot$. *Right panel:* Age-metallicity relation for the haloes derived using the fiducial feedback model. The starred (solid) points represent Pop III (Pop II/I) star-forming haloes. For clarity results are shown for a single realization.

ements ejected by SN winds mix with the external GM and can be accreted by other haloes, raising their metallicity. Contrary to self-enrichment by previous starburst within the same host halo and to hierarchical enrichment by contaminated progenitors, this accretion-driven enrichment mode is present *only* when mechanical feedback operates. Accretion of metal-enriched GM onto a halo of primordial composition sets the initial conditions for the environment in which most metal-poor stars will later form. Indeed, the unshaded histogram in Fig. 2.5 shows that when mechanical feedback is active the MDF extends down to [Fe/H] $\gtrsim \log(Z_{cr}/Z_\odot)$ as low-mass stellar relics can be produced only in gas clouds with $Z > Z_{cr}$.

The right panel of Fig. 2.5 shows how these two different enrichment modes operate along the merger tree in a single representative realization. Each point denotes the metallicity of a halo at a given redshift; in this plane haloes move from left to right *i.e.* they increase their metallicity. The evolution of each haloes is followed along its track until it suffers a merger event. Two families of curves can be identified, corresponding to self-enrichment and accretion mode, respectively, as marked by the labels in the Figure. In general, at the onset of the first burst of star formation a halo could be either metal-free ([Fe/H] $= -\infty$) or it could have a non-zero metallicity if it has accreted gas from the GM previously polluted by

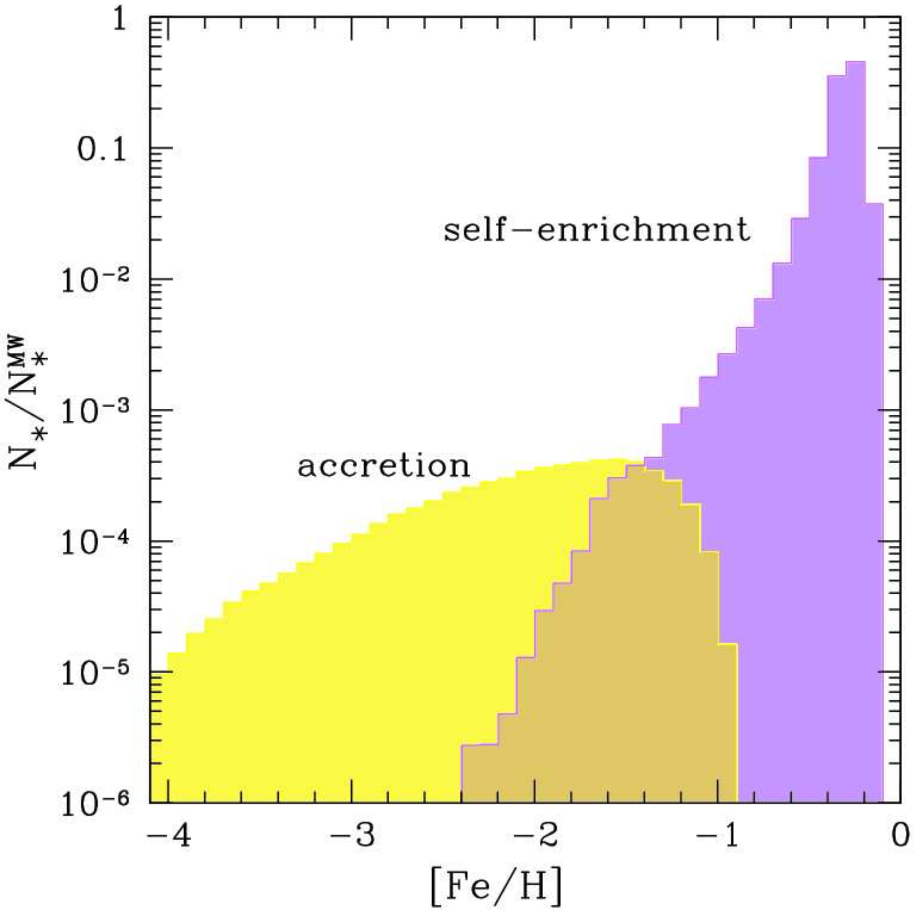

Figure 2.6: Fraction of stars in each [Fe/H] bin formed through accretion (yellow shaded histogram) and self-enrichment (violet shaded histogram) in the fiducial feedback model.

metals ejected from other haloes[8]. In the first case, the halo will host Pop III stars; if metals produced are retained after their explosion the halo becomes self-enriched and moves directly on the corresponding self-enriched track. In the second case, instead, depending on the relative ratio of the GM metallicity and $Z_{cr} = 10^{-4} Z_\odot$ the formed stars could be either Pop III or Pop II. In this particular realization at $z \sim 11$ the GM metallicity crosses the Z_{cr} value and sets the termination of the Pop III formation epoch in accretion-enriched haloes (Fig. 2.7). Such haloes lie on the curve marked as "accretion". However the second star-formation episode will push again these haloes onto the corresponding self-enriched tracks. The accretion-enriched branch ends at $z \sim 1$ and its iron-abundance, [Fe/H]~ -1, reflects that of the GM at the same redshift (see Fig. 2.7).

In Fig. 2.6 the contribution to the total MDF by stars formed via accretion

---

[8] The same conclusion applies to haloes that are just about to gravitationally collapse and virialize.

and self-enrichment is shown. We can observe that stars with [Fe/H]< -2.5 form *only* through the accretion-mode, while iron-rich stars, [Fe/H]> -1, only by self-enrichment. In the intermediate range, $-2.5 \leq$[Fe/H]≤ -1, stellar relics originating from self-enriched and accretion-enriched haloes cannot be distinguished, although at any given [Fe/H] self-enriched stars are systematically younger (fig. 2.5). We can also note that the contribution from the two different formation modes becomes comparable for [Fe/H]~ -1.5. However, stars formed through accretion only represent $\lesssim 0.1\%$ of the total number of Milky Way stars.

It is important to point out that another possibility to increase metal dilution along the merger tree allowing the formation of [Fe/H]< -2.5 stars, is to relax the hypothesis that all Pop III stars end up as $\mathrm{SN}_{\gamma\gamma}$ ($f_{\gamma\gamma} = 1$). Indeed if a fraction of Pop III stars forms with $m > 260 M_\odot$ or $m < 140 M_\odot$ ($f_{\gamma\gamma} < 1$) and ends up as black holes (Heger & Woosley 2002), metal enrichment can be substantially reduced. However, Schneider et al. (2006) have recently studied the dependence of chemical feedback from the parameter $f_{\gamma\gamma}$ (thus from the assumed Pop III IMF), showing that $f_{\gamma\gamma} = 1$ is currently favored by observations of the cosmic star formation history, high redshift number counts and cosmic reionization.

In conclusion mechanical feedback is necessary to reproduce both the global properties of the MW and the observed range of [Fe/H] in halo stars. In the following, we will refer to the best-fit feedback model of Table 1 as our fiducial model.

2.4 The Milky Way environment

From the above analysis it emerges the crucial role played by the MW environment, or GM. We want to stress that this ambient represents the mass reservoir into which haloes are embedded, from which they accrete gas, and out of which the newly forming haloes virialize. Indeed, a full cosmological description of the MW build-up, requires to follow the feedback-driven evolution of the GM properties, as they strongly affect all the subsequent formation of proto-Galactic haloes[9]. For the moment we will only focus on the effects of mechanical and chemical feedback, while in the last Chapters we will also analyze the impact of radiative feedback processes.

2.4.1 Metallicity evolution

The evolution of GM iron and oxygen abundances together with the specific contribution to [O/H] by Pop III and Pop II stars is shown in Fig. 2.7. For reference we also plot the observed [O/H] value measured in high-velocity clouds (Ganguly et al. 2005) which is taken as an indicator of leftover GM in the MW halo. We presented the results for our fiducial feedback model (see Table 1), with $Z_{cr} = 10^{-4} Z_\odot$ and

---

[9] Clearly the same conclusion has to be extended to any study of galaxies formation processes, if the analysis wants to account for the complete cosmological context.

$m_{PopIII} = 200M_\odot$, and for 200 hierarchical merger histories. The predicted [O/H] at $z = 0$ is in perfect agreement with the data. The scatter of the [Fe/H] distribution increases with z and becomes very large at $z \sim 11$ as a result of the large fluctuations in the merging history (see Fig. 2.3) and enrichment of haloes among different realizations at $z > 10$. This result is consistent with the fact that $Q = 1$ at $z = 11$ (see Sec. 2.2.7) and therefore no unpolluted regions are expected below that redshift. The scattering induced by the stochastic nature of the merger tree process is similar, although different in nature, with respect to the abundance fluctuations produced by inhomogeneous mixing, a process not describe by our perfect mixing approximation. This similarity can be appreciated by comparing our results with those found by Mori & Umemura (2006) using a hybrid N-body/hydrodynamic

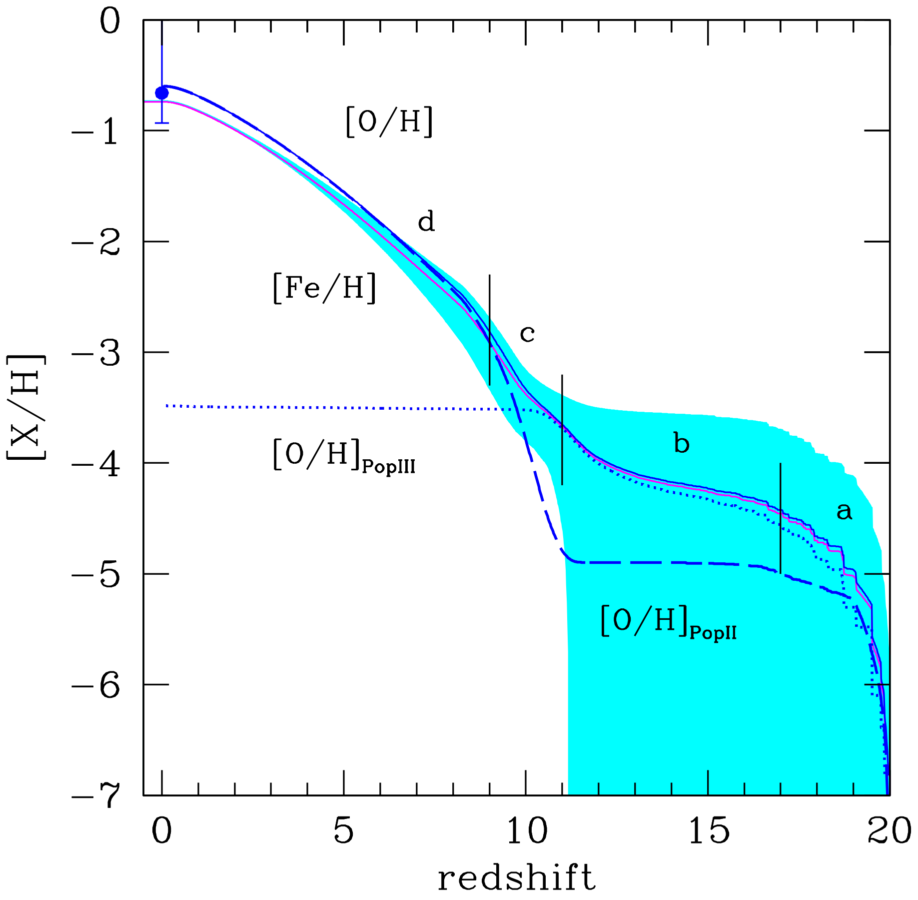

Figure 2.7: GM elemental abundance as a function of redshift for the fiducial feedback model (see Table 1) and $Z_{cr} = 10^{-4} Z_\odot$, $m_{PopIII} = 200M_\odot$. Solid lines show the evolution of oxygen and iron abundance, averaged over 200 realizations of the merger tree; the shaded area delimits the $\pm 1\sigma$ dispersion region. The [O/H] contribution by Pop III (dotted line) and Pop II stars (dashed line) are also shown separately. The point is the measured [O/H] in high-velocity clouds (Ganguly et al. 2005).

code. These authors conclude that the metallicity is highly inhomogeneous during the early phases of galaxy formation ($t \leq 0.1$ Gyr for a $10^{11} M_{\odot}$ galaxy) and becomes more uniform at lower redshifts (see also Fig. 1.2).

In the Figure we can observe that Pop III stars dominate the GM enrichment for $9 < z < 20$ while Pop II stars are the dominant enrichment channel for $0 < z < 9$. The GM enrichment history is the result of 4 phases controlled by different physical mechanisms; these phases are marked in Figure 2.7. The first one (phase a), in the redshift range $17 \lesssim z \lesssim 20$, is characterized by a very rapid increase of the elemental abundances. Given the small binding energy of the high-redshift, low-mass haloes, both $\mathrm{SN}_{\gamma\gamma}$ and the less energetic SNII explosions can overcome the gravitational pull of parent haloes, contributing to the GM enrichment. As the typical halo mass scale grows, as a result of hierarchical formation process (Fig. 2.2, metals produced by SNII are retained inside galaxies and only $\mathrm{SN}_{\gamma\gamma}$ regulate the GM enrichment (phase b). However the abundance grow is limited by the fact that an increasing fraction of the GM is polluted above Z_{cr}, hence quenching the formation of Pop III stars which eventually comes to an end at the beginning of phase (c) when the whole GM is enriched up to $Z > Z_{cr}$. Thanks to the higher star formation efficiency of larger haloes, Pop II stars can eject their heavy elements during this phase. Their ability to do so, though, decreases with time because of the counteracting effect of the gravitational potential of larger galaxies that are forming below $z = 5$ (phase d). Note that *the GM bears the nucleosynthetic signatures of (predominantly) Pop III stars at* $z > 10$; their abundance pattern becomes more and more elusive at later times when Pop II stars start to dominate the enrichment. This physical picture remains qualitatively unaffected by changing the value of Z_{cr} although the relative duration and amplitude of the different enrichment phases may vary. This enrichment history is particular important to interpret the observed features of the Galactic halo MDF as the various phases can be traced by the number of stars that are formed during each of them. We will discuss this point in the next Chapter.

2.4.2 Mass ejection from progenitor haloes

In Fig. 2.8 we show, for a single representative realization, the fraction of metals (or, equivalently, gas[10]) ejected by haloes, M_{ej}, as a function of their mass and redshift with respect to the total amount of metals predicted in the GM at $z = 0$, M_{ej}^{tot}. In the Figure, the curve M_{min} (M_{max}) denotes the minimum (maximum) halo mass in which star formation can develop, *i.e.* $M_{min} = M_{sf}(z) = M_4(z)$. Coherently with ΛCDM models, at high redshifts ($15 < z < 20$) haloes have typical masses close to M_{min}. As the redshift decreases, more massive haloes are produced (predominantly) via merging events which represent the dominant formation channel for $z < 6$ (Fig. 2.2), making $M_{max} \gg M_{min}$. As a general rule, the GM metal enrichment is dominated

---

[10] These quantities are equivalent because of the assumption that the wind has the same metallicity as the ISM of the parent galaxy (see Sec. 2.2.6).

for $z > 2$ by low-mass galaxies; it is only at later epochs that the contribution of larger galaxies becomes important. In fact the distribution seen in Fig. 2.8 is

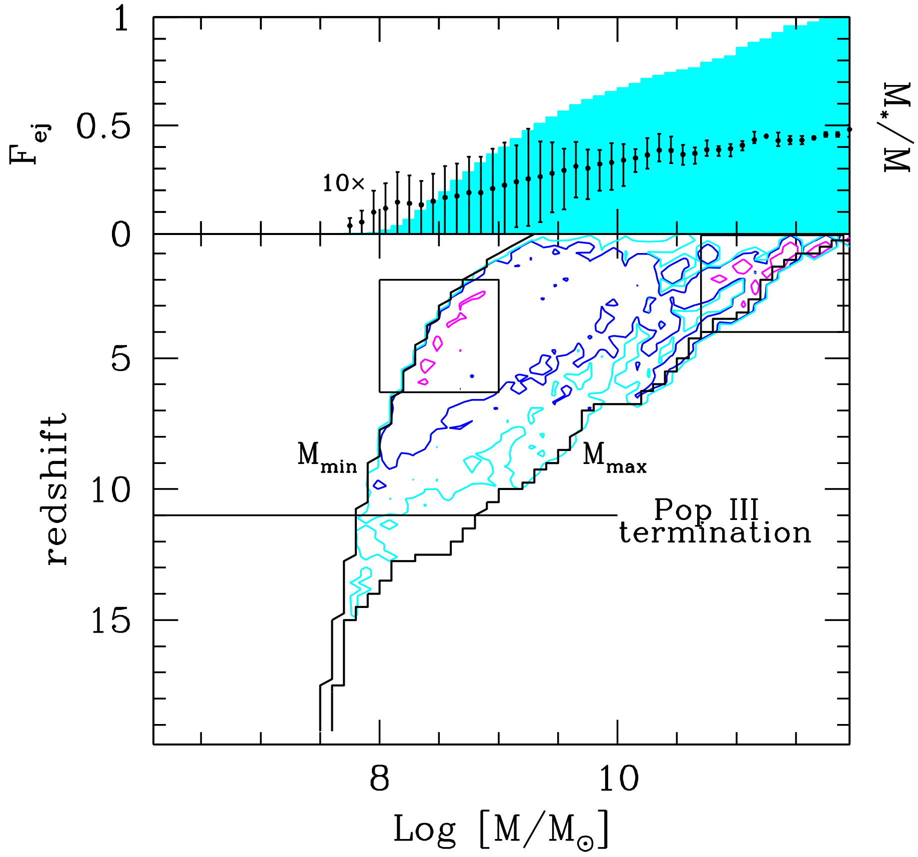

Figure 2.8: *Lower panel*: Fraction of metals ejected by haloes M_{ej} as a function of their mass and redshift with respect to the total amount of metals predicted in the GM at $z = 0$, M_{ej}^{tot}. Curves represent $M_{ej}/M_{ej}^{tot} = 5 \times 10^{-(4,3,2)}$ isocontours; also shown are M_{min} and M_{max}. The Pop III stars termination epoch ($z = 11$) is shown by the horizontal line. The two rectangles identify the position of the maxima (see text). *Top panel*: Cumulative fractional contribution, F_{ej}, to M_{ej}^{tot} integrated over redshift by haloes with different mass (shaded area); points with associated $\pm 1\sigma$ error bars represent stellar-to-total mass ratios in the corresponding mass bin (multiplied by 10).

bimodal: the first, more extended peak is found for $3 < z < 7$ corresponding to haloes in the mass range $M = 10^{8-9} M_\odot$; the second peak corresponds to larger galaxies $M = 10^{11} M_\odot$ at $z < 2$. The bi-modality can be understood as the result of the larger α_{ej} of low-mass haloes (due to their lower gravitational potential) and the larger gas content of more massive ones. The first effect dominates at high redshift; below $z = 2$ the ejected mass from larger haloes becomes substantial despite their relatively low values of α_{ej}. Halos in the intermediate mass range are born from a relatively small number of merging events of gas-poor progenitors and therefore little gas is left for further ejection. The largest haloes instead are characterized by higher baryonic fractions as they incorporate a larger number of progenitors with different histories. For example, haloes with mass $10^{8.5}M_\odot$ at $z = 5$ have contributed alone to 0.5% of the metals present in the GM today. An equivalent contribution is provided by the most massive MW progenitors in the second peak. In the first peak a large plateau is presents around the maximum indicating that low-mass galaxies $M < 6 \times 10^9 M_\odot$ play a fundamental role for the enrichment of the GM.

This is even more evident from an inspection of the top panel of the same Figure where we show the cumulative contribution to M_{ej}^{tot} integrated over redshift (F_{ej}). The curve grows rapidly for $10^8 M_\odot < M < 6 \times 10^9 M_\odot$ and $M > 10^{11} M_\odot$, with a flatter behavior in between, reflecting the afore-mentioned bimodal distribution. *About* 60% *of the ejected mass at* $z = 0$ *comes from haloes with* $M \lesssim 6 \times 10^9 M_\odot$, compared to 20% contribution from the most massive galaxies. We conclude that GM enrichment is dominated by low-mass haloes $M \lesssim 6 \times 10^9 M_\odot$. This result is insensitive to the value of Z_{cr}, although the relative contribution of Pop III and Pop II stars may vary.

As in our code we also store the information about the stellar mass corresponding to each DM halo we can rephrase the previous results in term of such quantity (points in the top panel of Fig. 2.8). Proto-galaxies that mostly contribute to GM pollution have a typical stellar-to-total mass ratio $M_*/M \lesssim 0.03$, or $M_* \lesssim 2 \times 10^8 M_\odot$. Note however that the scatter of the M_*/M ratio can be relatively large as shown by the error bars in the plot: the dispersion is caused by the different star formation histories. The scatter is maximum around $M = 10^9 M_\odot$; this population indeed is the most numerous one through most of the MW history and they may be produced by widely different combinations of formation processes and virialization epochs.

From Fig. 2.7 we have concluded that Pop III dominate the enrichment down to $z = 11$; from Fig. 2.8 we can also set an upper limit to the fraction of today's GM metals provided by Pop III stars. At $z = 11$ the largest halo from which metals can escape is $M \leq 2 \times 10^8 M_\odot$, corresponding to $F_{ej}^{PopIII} < 0.04$ meaning that Pop III stars contribute negligibly to the heavy elements currently detectable in the Galactic environment.

Chapter 3

Stellar relics in the Galactic halo

We are now ready to use the statistical machine provided by our semi-analytical model in order to investigate the implications of the stellar Metallicity Distribution Function (MDF) observed in the Galactic halo (Sec. 1.5.1). As the global MW properties are well matched by our fiducial model *independently* of the assumed mass of Pop III stars (m_{PopIII}) and critical metallicity (Z_{cr}) triggering the formation of low-mass stars, we can now explore the impact of the latter parameters into the predicted MDF shape.

Several authors have attempted to interpret the features of the observed Galactic halo MDF by applying different methods. Using a semi-analytical model, Hernandez & Ferrara (2001) deduced that a characteristic Pop III mass increasing toward high redshifts is required in order to fit the low-Z tail of the MDF. Prantzos (2003) pointed out that the stellar metallicity distribution depends sensitively on whether instantaneous recycling approximation (IRA) is adopted or relaxed. The low-Z cutoff in the MDF has been interpreted by Oey (2003) in the framework of stochastic chemical enrichment models, as a result of the various metal diffusion/transport/mixing processes at work in the Galactic environment. Along similar lines, Karlsson (2006) has noticed that the the metallicity desert between $-4.8 \lesssim$ [Fe/H]< -4 could be used to extract informations about the past Galactic star formation history.

More recently several works analyzed the MDF properties within the framework of the hierarchical merging paradigm, all providing a satisfactory match of the data for [Fe/H]> -4. By using a fully analytical model Prantzos (2008) pointed out that an early infall phase is required in each proto-Galactic haloes in order to reproduce the MDF shape below [Fe/H]≈ -3. Tumlinson (2006) and Komiya et al. (2009a, 2009b) investigated the properties of the first stars by developing algorithms similar in the spirit to our code GAMETE, although very different in calibration procedures and in some of the physical prescriptions. According to Tumlinson the Pop III IMF peaks in the range of massive stars, with mean mass between $(8-40)M_\odot$, and $Z_{cr} \lesssim 10^{-4}Z_\odot$. However the exact value of Z_{cr} cannot be constrained because of the limited number of low-[Fe/H] stars in the data sample. Komiya et al. used the statistics of the observed carbon-enhanced EMP stars (Sec.1.5.1) to constrain the IMF of these stellar populations, finding that it is shifted toward high-masses, with typical values of $\sim 10M_{\odot}$. In addition, they found that $\approx 50\%$ of EMP stars has to pertain to binary stellar systems. These IMF features, used as inputs in their hierarchical tree algorithm, provide a good match of the halo MDF. However they also have to invoke: (i) a mini-haloes pre-pollution mechanism by $\mathrm{SN}_{\gamma\gamma}$ in order to produce UMP/HMP stars, and (ii) a reduced formation of low-mass stars and low-mass binary members below [Fe/H]≈ -4 to reproduce the paucity of these UMP/HMP stars.

3.1 The Metallicity Distribution Function

Let‘s start by comparing the simulated MDF predicted by assuming $Z_{cr} = 10^{-4}Z_{\odot}$ and $m_{PopIII} = 200M_{\odot}$, with the reference Galactic halo MDF (Fig. 1.4), *i.e.* the joint HK/HES samples for [Fe/H]< -2 with the inclusion of the three stars with [Fe/H] $\lesssim -4.8$. Note that, in making such a comparison, we are implicitly assuming that all very metal-poor stars reside into the Galactic halo. Such a working hypothesis, dictated by the lack of spatial information preventing in distinguishing among different components, has been supported by the results of the N-body simulation by Scannapieco et al. (2006). Nowadays moreover, this is fully justified by the results of our recent study (Salvadori et al. 2009), which investigates the spatial distribution of very metal-poor stars in Milky Way halo by coupling GAMETE with the N-body simulation. We will present these results in the next Chapter.

In Fig. 3.1 the data sample is compared with the simulated MDF, that has been normalized to the total number of [Fe/H]≤ -2 stars observed. The results are plotted both in differential and in cumulative form. We can note that the model reproduces the observed MDF quite well, particularly for [Fe/H]> -3.2. A marginally significant deviation from the data (always within 1-σ) is seen at lower [Fe/H] *i.e.* a range populated by stars formed in accretion-enriched haloes (see Sec. 2.3.2). Note that, although this model provides a good match of the MDF including the low-Z cutoff, it cannot account for the existence of the three UMP/HMP stars. By definition indeed, the formation of long-living Pop II stars is allowed only if the gas in the star-forming region has a metallicity $Z \gtrsim Z_{cr} = 10^{-4}Z_{\odot}$ (adopted in this case), which in terms of iron-abundance means [Fe/H] $\gtrsim -4$.

3.2 Changing the critical metallicity

We can now explore which is the sensitivity of the simulated MDF to different Z_{cr} models, trying to bracket the current uncertainty on the determination of $Z_{cr} = 10^{-5\pm1}$ by matching the observed sample. In Fig. 3.2 the results obtained by using three different Z_{cr} values are presented. Note that the choice $Z_{cr} = 0$ is equivalent to

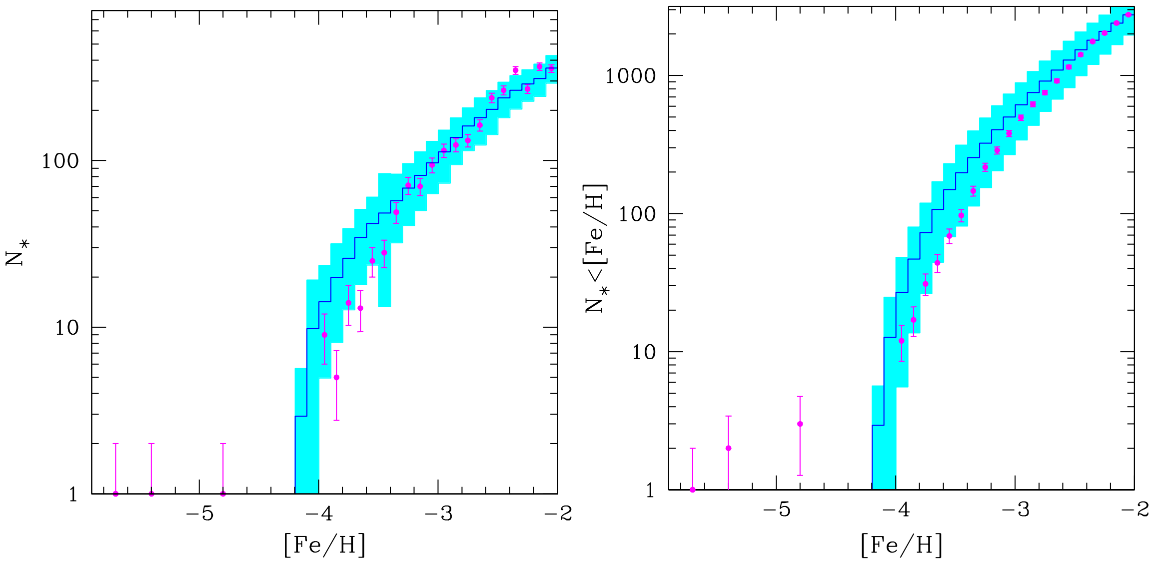

Figure 3.1: *Left panel*: Comparison between the observed Galactic halo MDF (see Sec. 1.5.1) (points), and the simulated one obtained by using the fiducial feedback model with $Z_{cr} = 10^{-4}Z_\odot$, $m_{PopIII} = 200M_\odot$ (histogram). The histogram is the average MDF value over 200 realizations of the merger tree and re-normalized to the number of observed stars with [Fe/H]≤ -2. The shaded area represents $\pm 1\sigma$ Poissonian errors. *Right*: The same results plotted in terms of the *cumulative* number of stars below a given [Fe/H].

state that *all* the stars, including the metal-free ones, form at every times according to a Universal Larson IMF (see Sec. 2.2.3), *i.e.* that Pop III stars have masses in the range $m_{PopIII} = [0.1, 100]M_\odot$. Conversely, we leave m_{PopIII} fixed to our reference value of $200M_\odot$ if $Z_{cr} > 0$.

The first striking result is that the MDF cutoff is shifted at gradually lower values of [Fe/H] when Z_{cr} decreases (for reasons discussed in Sec. 2.3.2); the high-[Fe/H] limit of the distribution appears unchanged, showing, in all cases, a very good agreement with the data for [Fe/H]≥ -3.2. However, the tendency of the data to drop faster than the model at lower [Fe/H], already noticed for $Z_{cr} = 10^{-4}Z_\odot$, persists. In particular, when $Z_{cr} = 10^{-5}Z_\odot$ the MDF shows a steep increase in $-5 <$[Fe/H]< -4.6 followed by a flat plateau extending up to [Fe/H]$= -4.1$, a markedly different shape with respect to the previously analyzed case $Z_{cr} = 10^{-4}Z_\odot$. This evolution bears the imprint of the GM chemical evolution and to understand it in detail it is useful to recall the four enrichment phases identified in Fig. 2.7. During phases in which the GM metallicity grows slowly (as in phase b), stars with approximately equal [Fe/H] are formed; instead, when the GM metallicity changes rapidly (phases a and c), stars born at slightly different cosmological times from accreted gas may have quite different [Fe/H], giving rise to the MDF plateau.

In general, though, the number of stars formed during phase (a) is too small to be appreciated from the normalized MDF. As Z_{cr} is decreased from $10^{-4}Z_\odot$

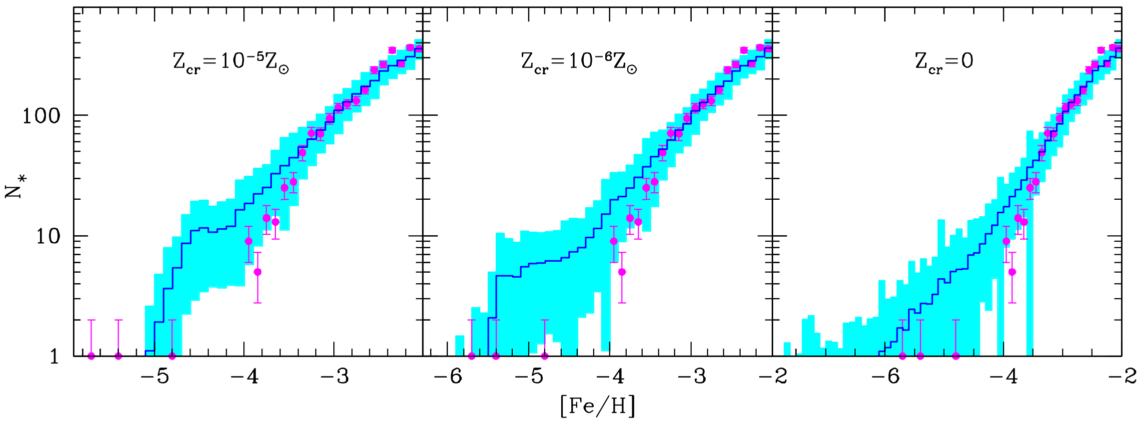

Figure 3.2: Same as left panel of Fig. 3.2 but for values of $Z_{cr} = 10^{-5}, 10^{-6}, 0\ Z_\odot$.

to zero, phase (b) contracts in time, being almost suppressed for $Z_{cr} = 0$. The correspondingly lower GM metallicity, explains the shift of the low-[Fe/H] MDF cutoff to lower values. The metallicity increase during phase (c) brings [Fe/H] to values ≈ -3, where Pop II always dominate the enrichment, independently of the value of Z_{cr}. This physical picture holds qualitatively also for the lower Z_{cr} case discussed below. This result can hardly be overlooked, as it shows that the MDF embeds the features imprinted by mechanical feedback and reflects the heavy element enrichment history of the MW environment.

As already mentioned, no stars have been detected so far by the various surveys in the range $-4.8 <$ [Fe/H] < -4, a feature that we have dubbed as the "metallicity desert". Not only the model with $Z_{cr} = 10^{-5}Z_\odot$ does not show such feature, but it also cannot account for the presence of the two HMP stars. The latter objects can instead be reproduced if $Z_{cr} = 10^{-6}Z_\odot$, which also account for the UMP star with [Fe/H]$= -4.8$. For the reasons explained above, the MDF plateau can now extend through the broad range $-5.6 \leq$[Fe/H]≤ -4.2. Even in this favorable case, though, the metallicity desert cannot be reproduced. If the desert is real or is a mirage produced by selection effects, it is impossible to tell at this stage. What is clear though is that hierarchical models like the present one have serious difficulties to prevent the formation of stars in the desert [Fe/H] range. We will return to this point in the discussion.

Finally, the case $Z_{cr} = 0$ is somewhat peculiar. Although it predicts stars for [Fe/H]< -4.8, as expected from the previous arguments, its MDF shape is different with respect to cases with $Z_{cr} \neq 0$, showing a monotonic increase in the range $-6 \leq$[Fe/H]≤ -2. When $Z_{cr} = 0$, in fact, no Pop III/II IMF transition occurs and, as a consequence, the GM enrichment proceeds more gradually. Even in this case, though, a considerable number of stars $\gtrsim 10$, is predicted in the metallicity desert.

Z_{cr} model	F_0
$10^{-4}Z_\odot$	6.0×10^{-9}
$10^{-6}Z_\odot$	5.8×10^{-9}
0	7.5×10^{-3}

Table 3.1: Values of the F_0 parameter (see text) as a function of the assumed Z_{cr}.

3.3 The lack of $Z = 0$ stars: implications

An interesting issue we can address by using our model concerns the implications for the actual non detection of metal-free stars in the Galactic halo. This observational result can be quantified by using the parameter F_0, which has been originally introduced by Oey (2003) and later improved by Tumlinson (2006). F_0 is defined as the number of metal-free stars divided by the total number of stars with [Fe/H]< -2.5. The observational limit on the value of F_0 is given by the inverse of the total number of stars with [Fe/H]< -2.5 observed into the Galactic halo (where the numerator of the ratio is fixed equal to 1 to give a non-vanishing limit). Using the reference sample by Beers & Christlieb (Sec. 1.5.1) we find that $F_0^{obs} = 1/1152 \sim 8.7 \times 10^{-4}$. In Table 3.1 we present the values of F_0 obtained using the models $Z_{cr} = 10^{-4}Z_\odot$, $Z_{cr} = 10^{-6}Z_\odot$, $Z_{cr} = 0$. Models $Z_{cr} \geq 10^{-6}Z_\odot$ give a value of F_0 compatible with the observational limit whereas for $Z_{cr} = 0$ we find $F_0 = 7.5 \times 10^{-3} > F_0^{obs}$. In this case, in fact, the first burst of Pop III stars produces a huge amount of metal-free, long-lived stars which dramatically pushes F_0 beyond the allowed range. Thus, this parameter allows to *robustly rule out* models in which the critical metallicity is zero, and/or put an important constraint on primordial IMF. In the second option, in order not to conflict with the observations, we must set a lower limit on the mass of the first stars equal to $m_{PopIII} > m_1(z \sim 20) \sim 0.9M_\odot$, *i.e.* the stars have a mass larger than the turn-off mass at $z \sim 20$, the epoch at which the first star formation events occur in our model.

3.4 Second generation stars

An additional information that can be extracted from our study is the fraction of "second generation" (2G) stars, defined as the stars which have been enriched *only* through the nucleosynthetic products of Pop III stars. From an observational point of view it is crucial to identify 2G stars because by studying their elemental composition we could trace back the properties of the first stars that polluted them.

In Fig. 3.3 we identify the MDF regions populated by 2G stars and their fractional number for three values of Z_{cr}. For $Z_{cr} \geq 10^{-6}Z_\odot$ 2G stars populate both the lowest and the highest [Fe/H] tails of the MDF, *i.e.* they formed both in the accretion and self-enrichment modes. If $Z_{cr} = 0$, on the contrary, they can be produced only through self-enrichment. This is because in this case the first (metal-free) Type II SN, are not energetic enough to expel their metals which remain confined within the parent haloes. The instantaneous mixing approximation implies that when Pop II stars are able to eject metals into the GM the formation of 2G stars instantaneously ceases everywhere.

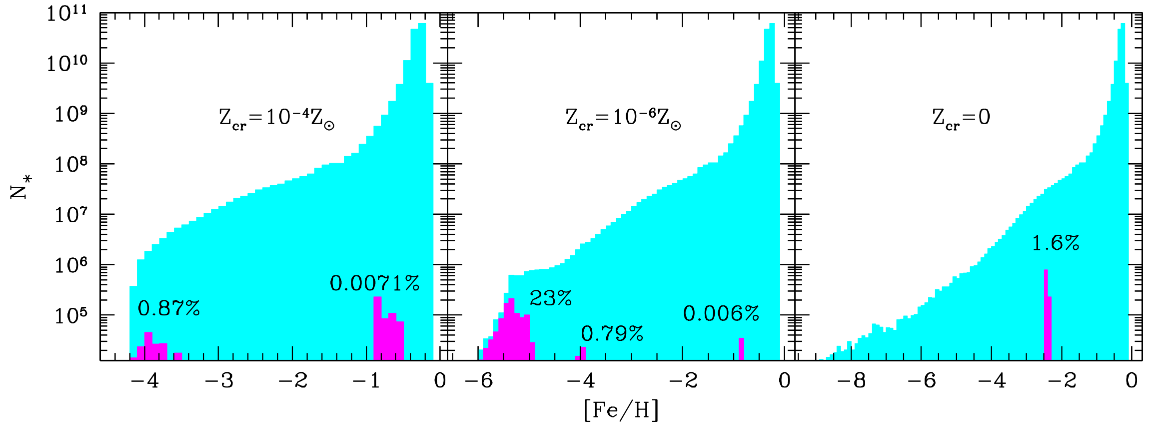

Figure 3.3: Impact of second generation stars for the fiducial feedback model $Z_{cr} = 10^{-4}, 10^{-6}, 0\ Z_{\odot}$. In each panel, the highest (cyan) histogram show the total MDF; the smaller (magenta) histograms represent the MDFs for the 2^{nd}-generation stars. The percentages show the fraction of 2^{nd}-generation stars with respect to the total in the ranges in which they appear.

More specifically, the dominant formation channel of 2G stars is accretion when $Z_{cr} = 10^{-6} Z_{\odot}$ and self-enrichment when $Z_{cr} = 10^{-4} Z_{\odot}$, reflecting the different Pop III/II transition redshift. In the case $Z_{cr} = 10^{-6} Z_{\odot}$ the transition occurs rapidly as a result of the lower amount of metals necessary to reach the critical threshold. Hence, 2G stars can be formed through self-enrichment only in the few haloes hosting Pop III stars; however, in unpolluted haloes accreting gas from the GM, 2G stars can continue to form until the time at which feedback from Pop II stars raises the GM metallicity substantially. For the same reasons, the trend is reversed when $Z_{cr} = 10^{-4} Z_{\odot}$.

Along with their location on the [Fe/H] axis, the percentages shown in Fig. 3.3 quantify the relative number of 2G stars with respect to the total number of stars in the iron-abundance ranges in which 2G stars are found. Two points are worth noting. First, the number of 2G stars formed by self-enrichment is negligible; even in the case $Z_{cr} = 0$, their relative abundance is only 1.6% of the total population of stars with $-2.5 \leq$[Fe/H]≤ -2.3; this means that only 10 of the 612 halo stars observed in the above [Fe/H] range could be truly 2G stars. Second, it is only in the metallicity bins close to the Z_{cr} value that the fraction of 2G stars increases substantially, thanks to the accretion mode of formation operating at those metallicities. However, given the

Z_{cr} model	Number of 2G stars
$10^{-4}Z_\odot$	1.3
$10^{-6}Z_\odot$	0.3
0	6×10^{-2}

Table 3.2: Number of 2G stars expected in the HK/HES sample by Beers & Christlieb for different Z_{cr} models.

very low number of extremely metal-poor stars observed, *their absolute number in the available data sample is likely to be close to zero.* In practice, given the HK/HES sample made by 1150 stars within the range $-4 \leq$[Fe/H]< -2.5, we conclude that, independently of Z_{cr}, the probability to have pure 2G stars among those observed is virtually zero (Table 3.2). Note however that in the case $Z_{cr} = 10^{-6}Z_\odot$ almost all the stars with [Fe/H] $\lesssim -5.4$ are predicted to be 2G stars.

3.5 Varying the Pop III mass

Finally, we can study the impact of varying the mass of Pop III stars in $Z_{cr} > 0$ models. In particular we will explore the effects of setting m_{PopIII} equal to $140M_\odot$ and $260M_\odot$. These two values indeed are the extremes of the $\mathrm{SN}_{\gamma\gamma}$ mass range and respectively correspond to the minimum and maximum iron yield of $Y_{Fe} = 2.8 \times 10^{-15}$ and $Y_{Fe} = 0.45$. We recall that instead, $Y = 0.45$, independently of m_{PopIII}.

In Fig. 3.4 the observed MDF is compared with the six different models, obtained by combining the three critical metallicity values already explored ($Z_{cr} = 10^{-6}, 10^{-5}, 10^{-4}Z_\odot$) with the two Pop III masses ($m_{PopIII} = (140, 200)M_\odot$). We immediately observe that for $m_{PopIII} = 140M_\odot$, the shape of the MDFs is *completely independent of* Z_{cr} and closely resembles the behavior found for the case $Z_{cr} = 0$. This result from the extremely low Y_{Fe} of $140M_\odot$ stars, which makes their contribution negligible to that of Pop II stars which therefore are controlling the MDF shape. If $m_{PopIII} = 260M_\odot$ instead, the MDF cutoff result quite sensitive to the value of Z_{cr}, shifting toward lower [Fe/H] values with decreasing Z_{cr}. Such trend is very similar to the one already found for models with $m_{PopIII} = 200M_\odot$. In this case however, the cutoff is located at higher [Fe/H] value because of the higher value of Y_{Fe}. For this reason the observed data are better reproduced by model with $Z_{cr} \leq 10^{-5}Z_\odot$. Note however that even these models cannot account for the presence of the three UMP/HMP stars.

In conclusion the MDF is sensitive to the value of m_{PopIII}. However, as long as m_{PopIII} is within the $\mathrm{SN}_{\gamma\gamma}$ mass range, it is always possible to find satisfactory fits to the data by suitable changing Z_{cr} within its uncertainty interval $Z_{cr} = 10^{-5\pm1}Z_\odot$.

Most importantly both the value of F_0 (Sec. 3.3) and the number of 2G stars (Sec. 3.4) are practically independent of the value of m_{PopIII}. In particular, using the two best models $m_{PopIII} = 140M_\odot$, $Z_{cr} = 10^{-4}Z_\odot$ and $m_{PopIII} = 260M_\odot$, $Z_{cr} = 10^{-6}Z_\odot$ we obtain $F_0 = 6.88\times10^{-9}$ and 6.3×10^{-9}, respectively. The expected number of 2G stars in the reference data sample, to be compared with Tab. 3.2, is equal to 3.45×10^{-2} and 2.2×10^{-2}, respectively.

3.6 Summary and discussion

In this Chapter the implications for the observed features of the Galactic halo MDF have been investigated within the cosmological context of the hierarchical Galaxy formation. To this aim we used our semi-analytical code GAMETE, *previously calibrated* in order to reproduce the observed properties of the Milky Way (Sec.2.3). The impact of different Z_{cr} and m_{PopIII} values on the simulated MDF has been explored by varying these parameters *only*, and by using a statistically significant sample of 200 hierarchical merger histories. The latter alleviate the effects of our perfect mixing approximation (Sec. 2.2.7) as the spread induced by the stochastic nature of the merger histories mimic that found by sophisticated numerical simulations of mixing in individual galaxies (Sec.2.4.1). The main results of our study can be summarized along the following points:

- The fiducial (feedback included) model for which $Z_{cr} = 10^{-4}Z_\odot$, $m_{PopIII} = 200M_\odot$ provides a very good fit to the MDF, including the cutoff observed at [Fe/H]$= -4$. However, the existence of the three UMP/HMP stars with [Fe/H]≤ -4.8 cannot be explained by this model.

- Models with $Z_{cr} \leq 10^{-6}Z_\odot$ and $m_{PopIII} = 200M_\odot$ can account for these UMP/HMP stars but at the price of overproducing the number of stars below [Fe/H]≈ -3.5 and hence overpopulating the “metallicity desert”.

- The current non-detection of metal-free stars, which provides a value of the parameter $F_0 = 1/1152$, *robustly* constrains either Z_{cr} to be larger than zero or the masses of the first stars to be $m_{PopIII} > 0.9M_\odot$.

- The statistical impact of truly second generation stars, *i.e.* stars forming out of gas polluted *only* by metal-free stars, is found to be negligible, independently of the assumed Z_{cr} and m_{PopIII} values. In the observed Galactic halo sample only (at best) 1-2 stars could retain such metal-free nucleosynthetic imprint.

These findings agree with the studies by Tumlinson (2006) and Komiya et al. (2009) in supporting the massive nature of Pop III stars, and the existence of a critical metallicity (probably equal to $Z_{cr} \approx 10^{-4}Z_\odot$) strongly connected with the MDF cutoff. However, the poor statistics of the observed sample below [Fe/H]≈ -3, and the degeneracy of the models on the adopted free parameters, prevent from finding converging results on the Pop III IMF, and the MDF shape is well reproduced by models assuming very different functional forms.

Within the present study, not devoted to constrain the Pop III IMF, we have assumed it to be either a δ-function in the $\mathrm{SN}_{\gamma\gamma}$ mass range $140M_\odot < m_{PopIII} < 260M_\odot$, or a standard Larson IMF (when $Z_{cr} = 0$). Given the strong [Fe/H] dependence of the $\mathrm{SN}_{\gamma\gamma}$ mass, we have adopted the mean value of the interval as our benchmark, $m_{PopIII} = 200M_\odot$, but we have also explored the implications of assuming the two extreme values, $140M_\odot$ and $260M_\odot$. Our results show that by varying m_{PopIII} within the $\mathrm{SN}_{\gamma\gamma}$ mass range, it is always possible to find satisfactory fits to the data by changing Z_{cr} within its uncertainty interval $Z_{cr} = 10^{-5\pm1}Z_\odot$. It follows that a comparison with additional observations, as for example the chemical abundance of halo stars, is required in order to robustly constraint the Pop III IMF. The investigation by Komiya et al. (2009) develops along this line but, unfortunately, do not use the observed MW properties in order to independently fix the star formation and SN wind efficiencies, hence introducing additional free parameters.

We want to stress that our findings on both the current non-detection of metal-free stars and the impact of the second stellar generation on the data sample, are valid for any couple of Z_{cr}-m_{PopIII} *i.e.* they are not affected by this model degeneracy. During the recent years growing attention has been posed on probing the nucleosynthetic patterns of extremely metal-poor stars, with the hope that these objects are born from gas polluted purely by (a single ?) metal-free SN. Unfortunately, our study shows that these second generation stars have number frequencies that are so low to be zero even in the largest available sample used in the present analysis. A different perspective on the recent data by Cayrel et al. 2004 (later interpreted by Chiappini et al. 2005) is opened by our findings, which indicates that the stars used for the analysis are unlikely to be second generation stars; instead, they represent a more mature population in which the abundance scatter has been smoothed out by several re-processing cycles of the gas.

Additional work is necessary to understand the issues related with the "metallicity desert" *and* UMP/HMP stars, not reproduced by the models unless by assuming a stochastic chemical enrichment of the star-forming gas (Karlsson 2006). In its simplest form this problem can be stated as follows: in order to produce low-mass stars with [Fe/H] $\lesssim -4.8$ the value of Z_{cr} must be decreased to similar levels (or below); as a consequence, an uncomfortably large number of stars is predicted in the desert. In addition we have to take in to account that UMP/HMP stars exhibit very peculiar abundance patterns, being characterized by large overabundance of carbon and nitrogen (*i.e.* $Z \gg Z_{cr}$) with respect to iron. Two class of theoretical models have been proposed to interpret their abundances: (i) they were born in a medium pre-enriched by the yields of one or more SNe (Christlieb et al. 2002, 2004; Umeda & Nomoto 2003; Bonifacio, Limongi & Chieffi 2003; Schneider et al. 2003; Iwamoto et al. 2005), meaning that their low [Fe/H] abundance simply reflects the peculiar evolutionary pattern of their stellar progenitors; (ii) they were born in a primordial environment, consistent with their observed [Fe/H] values, subsequently acquiring their heavy elements through self-enrichment and/or accretion from a binary companion (Shigeyama, Tsujimoto & Yoshii 2003; Suda et al. 2004; Komiya et al. 2009b).

If the first scenario is correct these stars are simply peculiar objects, and the results of the semi-analytical models are reconciled with the observations. Otherwise a mechanism able to form a *very small* number of long-living stars with [Fe/H] $\lesssim -4.8$, has to be provided. A possible solution is given by dust. As pointed out in Sec. 1.3.3 indeed, the Z_{cr} value strongly depends on the total amount of metals locked into dust grains, varying from $Z_{cr} = 10^{-6} Z_{\odot}$ if all the metals are depleted into dust ($f_{dep} = 1$), up to $Z_{cr} = 10^{-4} Z_{\odot}$ if $f_{dep} = 0$. Since the metals released by Pop III stars have high depletion factors, $f_{dep} = (0.3 - 0.7)$, as long as these primordial stars dominate the metal enrichment, they can keep the critical metallicity down to very small values ($Z_{cr} \lesssim 10^{-5} Z_{\odot}$), hence allowing the formation of long-living HMP stars. However, as soon as Pop II stars begin to control the metal enrichment ($z \lesssim 10$, see Fig. 2.7) Z_{cr} can suddenly increases up to $\approx 10^{-4} Z_{\odot}$, thus preventing the formation of low-mass stars in the metallicity desert.

An alternatively explanation is provided by gas heating. In principle, if the Pop III star formation episodes can spread their metals into the GM to reach a metallicity levels of [Fe/H] ≈ -5, they could also heat the gas to about $T_h \gtrsim 10^5$ K. In such preheating scenario (Madau, Ferrara & Rees 2001) gas accretion on virializing haloes with $T_{vir} < T_h$ would be prevented, whereas star formation and self-enrichment could continue in already collapsed structures, which would increase the GM metallicity through their winds. It is only when dark matter haloes of sufficiently large mass become numerous that accretion onto them could start again, now producing stars with [Fe/H]> -4. Translated in redshift, and guided by Fig. 2.7, the metallicity desert could translate in a gap of $\Delta z \approx 5$ at $z > 10$ in which accretion is halted by the preheating, another aspect of the mechanical feedback, which once again is found to play a crucial role in the problem.

We recall, finally, that the metallicity desert could also be a mirage of the selection effects in metal-poor stellar surveys, as suggested by the recent detection of the [Fe/H]$= -4.8$ star (Christlieb et al. 2008), located in a metallicity region previously associated with the desert. Will ongoing surveys reveal the existence of new stars between $-4.8 <$[Fe/H]< -4? Are UMP/HMP stars incredibly rare objects or is their number density extremely low in the regions currently explored by the stellar surveys? A larger statistical sample is clearly required.

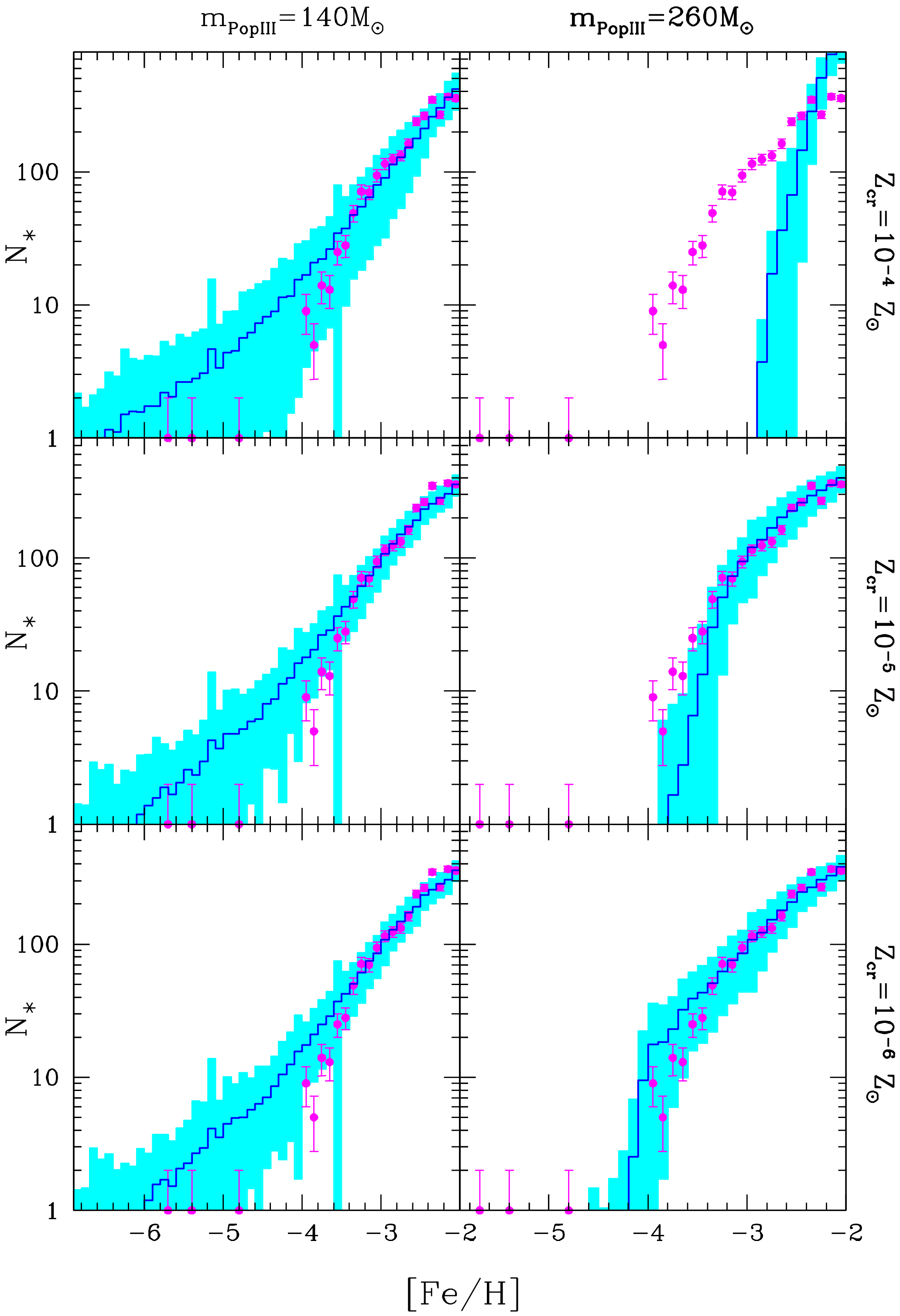

Figure 3.4: Same as left panel of Fig. 3.1 but for different values of $m_{PopIII} = 140M_\odot, 260M_\odot$ and $Z_{cr} = 10^{-4}, 10^{-5}, 10^{-6}Z_\odot$.

Chapter 4

Searching for metal-poor stars

The importance of very metal-poor stars as powerful objects to investigate the properties of the first stellar generations has emerged from the previous Chapter. However it also emerged the demand of collecting larger stellar sample, especially at the lowest metallicities ([Fe/H]< -3); an higher statistics, in fact, would allow to put more solid constraints on the properties of the first stars and to (re-)formulate the problem of the metallicity desert in its definitive form. From an observational point of view however, the intrinsic problem one have to face is that old, very metal-poor (VMP) stars, are extremely rare in the solar neighborhood, comprising no more that the $\sim 0.1\%$ of the stars within a few kpc of the Sun (Beers et al. 2005). Hence, to understand where these stars are preferentially located is an urgent practical question, which has to be theoretically solved.

In addition, the recent analysis of the SDSS calibration stars by Carollo et al. (2007, see also Sec. 1.5.1) have revealed the existence of an "outer" halo, located at Galactocentric radii $r \geq 15$ kpc, which includes a larger fraction of [Fe/H]< -2 stars and peaks at lower metallicity than the "inner" halo ($r < 15$ kpc) does. This evidence poses new challenging questions about the physical origin of such a segregation and the variation of the MDF with Galactocentric radii.

Recently, De Lucia & Helmi (2008), have used a series of high-resolution simulations of MW-size haloes to study the formation of the Galaxy and its stellar halo, finding evidences for the inner/outer halo dichotomy. According to these authors in fact higher-metallicity halo stars ($Z > 0.4Z_{\odot}$) are strongly concentrated toward the Galactic center, while those with lower-metallicities ($Z < 0.4Z_{\odot}$) mostly reside beyond 20 kpc. However, the metallicity of the simulated stars is found to be higher ($Z \gtrsim 0.1Z_{\odot}$) with respect to those observed in the Galactic halo (probably because of the modeling of mechanical feedback), hence preventing the authors from exploring the variation of the halo MDF at different Galactocentric radii. In this Chapter we will investigate the spatial distribution of metal-poor halo stars by combining the high-resolution N-body simulation by Scannapieco and collaborators (Sec. 2.1.1) with our semi-analytical code GAMETE.

4.1 Model improvements

Two additional features have been improved in the model:

- *Mechanical feedback*: by assuming a continuous mass loss prescription (Larson 1974) the mass of gas ejected into the surrounding GM is regulated by the equation

  $$\frac{1}{2} M_{ej} v_e^2 = E_{SN} \tag{4.1}$$

  where E_{SN} is the kinetic energy injected by SN-driven winds (eq. 2.13) and $v_e^2 = GM/r_{vir} = 2E_b/M$ is the escape velocity of the gas from a halo with mass M and binding energy E_b (eq. 2.14). By differentiating the eq. 4.1 we found that the ejection rate is proportional to the SN explosion rate through the relation:

  $$\frac{dM_{ej}}{dt} = \frac{2\epsilon_w \langle E_{SN} \rangle}{v_e^2} \frac{dN_{SN}}{dt} , \tag{4.2}$$

  where ϵ_w is the usual free parameter controlling the SN wind efficiency. Hereafter we will use the expression in eq. 4.2 in order to compute the mass of gas and metals ejected by each star forming halo of the hierarchical tree at each time-step.

- *Reionization imprints:* we account for the effects of the GM reionization by assuming that, after its accomplishment (z_{rei}), the formation of galaxies with circular velocity $v_c < 30$ km/s is suppressed, mining that $M_{sf}(z \leq z_{rei}) = M_{30}(z) = M(v_c = 30 \text{ km/s}, z)$. According with the results of our study (Salvadori, Ferrara & Schneider 2008, see Chapter 6) we assume in the MW environment reionization is complete at $z_{rei} = 6$.

As the N-body simulation is unique, we are now loosing all the statistical information provided by different hierarchical merger histories. These, in particular, accounted for the large spread of the GM metallicity at high redshifts (Sec. 2.4.1), reproducing the effects of an inhomogeneous mixing of metals despite of the perfect mixing approximation. To estimate the impact of the above approximation on model results we explore a simple case of *inhomogeneous metal mixing*, modeled by computing the instantaneous filling factor $Q = (\sum_i 4\pi R_b^3(i)/3V_{MW}(z))$ of the metal bubbles inside the critical MW volume $V_{MW}(z) = 30(1+z)^{-3}$ Mpc^3, and by randomly enriching a fraction $F = 1 - exp(-Q)$ of GM particles. Note that this only provides an upper limit on F, as a clustered system, such as the stars we are considering, will have a smaller filling factor. A simple Sedov-Taylor blastwave solution (Sec. 2.2.7) is used to estimate the bubble radii $R_b(i)$. This case is compared with the perfectly mixed one in Fig. 4.2 (upper panel on the right).

4.2 Testing the model

The model is calibrated as usual, by simultaneously reproducing the global properties of the MW (stellar/gas mass and metallicity) and the metallicity distribution function (Sec. 2.3). Moreover, according with the results of the previous Chapter we fix $m_{PopIII} = 200 M_\odot$ and $Z_{cr} = 10^{-4} Z_\odot$, and check the agreement with the Galactic halo MDF.

4.2.1 The Age-Metallicity relation

A first test of our model results is a comparison with the observed stellar Age-metallicity relation; the results are shown in Fig. 4.1. The simulated distribution can be virtually divided into three main regions defined by the prevailing formation mode of the stars contained within them. The first region (age $>$ 13 Gyr, or $z > 7.5$) is populated by old stars covering almost the entire metallicity range, from [Fe/H]~ -0.3 to [Fe/H]$= -4.2$, and which correspond to the observed *bulge* and *halo* components (see the rectangles in Fig. 4.1). These stars formed in proto-galactic haloes associated to high ($> 2\sigma$) density fluctuations, that virialized during the early stages of Galaxy formation at $z > 7.5$. Similarly to what discusses in Sec. 2.3.2 these first stellar generations *self-enriched* the ISM of their host galaxies up to [Fe/H]> -2, quenching the formation of additional very metal-poor stars. At the same time, metals are expelled by SN feedback in the GM, thus increasing its metallicity above $Z_{\rm cr}$ by $z = 11$ and allowing long-living metal-poor stars to form in newly virialized haloes *accreting* their gas from the GM. From $z = 11$ to $z = 7.5$ coeval formation of metal-poor and metal-rich stars occurs in different objects through accretion and self-enrichment processes. During this epoch $-3 <$[Fe/H]< -2 stars are produced via merging of self-enriched and accreted haloes.

The second region (Age $<$ 13 Gyr, [Fe/H]< -0.3) is filled by stars which almost span the entire range of ages and metallicities along a relation on which the iron-abundance increases with decreasing age (*halo, bulge, thick and thin disk*). These stars formed in accreting haloes; the minimum [Fe/H] value of the stellar distribution at different epochs reflects the iron evolution of the MW environment. Stars located in this area only represent $< 10\%$ of the total stellar mass at $z = 0$.

The third region ([Fe/H]> -0.3) is populated by iron-rich stars formed in self-enriched haloes, which therefore span all the possible ages (*bulge, thin and thick disk*). The bulk of the stellar mass resides in this region and corresponds to the broad peak of the SF rate, $2 < z < 5$ (see for a representative SF history Fig. 5.1). Note that the most iron-rich stars in the simulation with ages $<$ 12 Gyr, are poorer in iron than those observed. This systematic effect may be a consequence of neglecting the contribution of SNIa to gas enrichment. However because this study is mostly concentrated on the spatial distribution of *old* and *iron-poor* Galactic halo stars this does not affect the main results. Even if we consider the possible existence of a

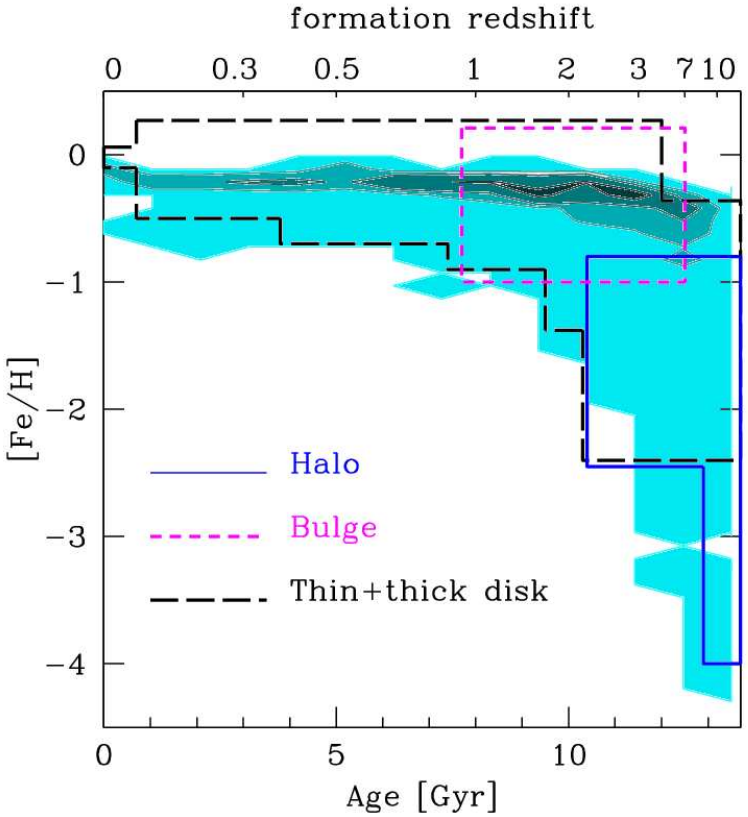

Figure 4.1: Comparison between the observed (rectangles) and simulated (shaded regions) age-metallicity distribution of MW stars. Rectangles show the observed relation for different Galactic components (Freeman & Bland-Hawthorn 2002, Fig. 2): old field stars, old and young halo globulars (blue solid rectangles); thin and thick field stars, thin disk open clusters, thick disk globulars (black long-dashed rectangles); bulge (violet short-dashed rectangles). The colored shaded areas correspond to regions that include, from the darkest to the lightest, the $(30, 62, 90, 100)\%$ of the total number of relic stars produced in the simulation, $M^*_{tot} \approx 4 \times 10^{10} M_\odot$.

"prompt" SNIa component, with lifetime of SNIa of 0.1 Gyr (Mannucci, Della Valle & Panagia 2006), this is typically longer than the evolutionary time-scale of SNII (< 0.03 Gyr). Therefore, the iron produced by the first SNIa will only marginally contribute to pollute an ISM which has been already largely pre-enriched by *several* generations of SNII and Pop III stars.

In the following we will focus on the properties of old metal-poor [Fe/H]< -1 stars, whose features are unaffected by the lack of disk formation and SNIa contribution of our study. In addition, by excluding from our sample all the stars residing at distances < 1 kpc from the Galactic plane, we remove possible contamination by thin/thick disk stars.

4.2.2 The Metallicity Distribution Function

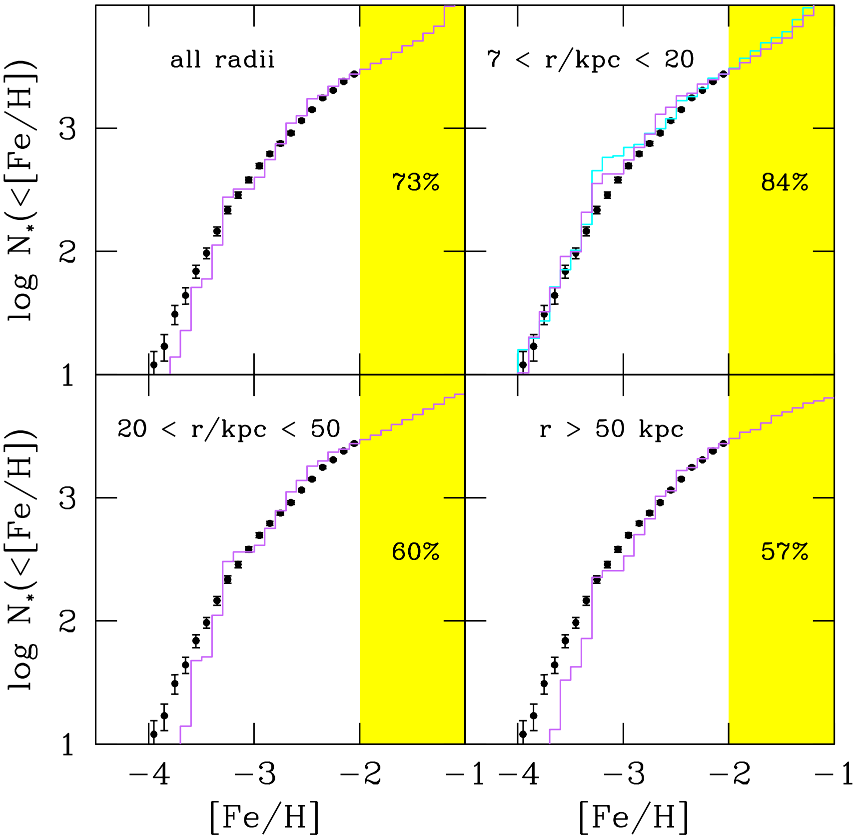

Figure 4.2: Comparison between the cumulative MDF observed in the Galactic halo within $\lesssim 20$ kpc of the Sun (points with Poissonian error bars in all panels, Beers et al. 2005) and those produced in the simulation at different radii (violet histograms) normalized to the number of observed stars. The cyan histogram shows the $7 < (r/\mathrm{kpc}) < 20$ MDF for the inhomogeneous mixing case. For each range of radii the numbers show the percentage of $-2 <$[Fe/H]≤ -1 stars (shaded area) with respect to the total number of [Fe/H]≤ -1 stars.

In the right upper panel of Fig. 4.2 the Galactic halo MDF observed by Beers et al. (2005) is compared with the simulated one at galactocentric distances $7 < (r/\mathrm{kpc}) < 20$. The agreement between the model results for a radial interval representative of the observed region and the data is very good. In the same panel we show for comparison the simulated $7 < (r/\mathrm{kpc}) < 20$ MDF for the inhomogeneous mixing case (cyan histogram). The two mixing prescription only yield a marginal differences, mostly concentrated in the range $-3.5 <$[Fe/H]< -3. These results encourage us to formulate explicit predictions for the radial dependence of the simulated MDF. To explore this point, we compare the *same* observational data with theoretical MDFs obtained in *different* radial bins and normalized to the number of observed stars. We note that the all-radii MDF (left upper panel) already provides a satisfactory match of the data, implying that the observational sample obtained in the above r-range provides a good proxy for the all-radii one. A marginal discrepancy at the low-Fe end of the distribution is found when comparing the observed data with theoretical MDFs derived for $r > 20$ kpc (lower panels), which becomes more sensible as r increases. In conclusion, we find that the MDF varies only very weakly with radius. On the contrary, and in agreement with recent findings by Carollo et al. (2007) and De Lucia & Helmi (2008), the relative contribution of $-2 <$[Fe/H]< -1 stars to the total MDF strongly depends on r, varying from 84% within 7 kpc$< r < 20$ kpc, down to $\leq 60\%$ for $r > 20$ kpc.

4.3 The spatial distribution of metal-poor stars

An inspection of Fig. 4.4 will allow to better understand the MDF features we have just discussed. This Figure indeed offers a spatial visualization of the MDFs in the $\rho - \zeta$ cylindrical coordinate plane, where ζ is the rotation axis and $r^2 = \rho^2 + \zeta^2$. We show the results for the central 100×100 kpc^2 region. Each panel of the figure displays a subset of relics stars ($z = 0$) in a different metallicity range: *metal-poor* (MP), $-2 <$[Fe/H]≤ -1, *very metal-poor* (VMP), $-3 <$[Fe/H]≤ -2, *extremely metal-poor* (EMP), $-4 <$[Fe/H]≤ -3 and "ghost" *Pop III stars*, $Z < Z_{cr}$[1]. We deserve the name of ghost for PopIII stars because our assumptions ($m_{PopIII} = 200 M_\odot$, $Z_{cr} = 10^{-4} Z_\odot$) imply that all of them have been already evolved and disappeared at the present time. The colors in the panels show the total mass of stars contained in an annulus of radial width within 1 kpc, normalized to the total MW stellar mass. The stellar distribution closely follows the dark matter one, *i.e.* it is denser toward the center and in the 10 dwarf galaxies found in 50 kpc $< r <$ 100 kpc. The radial dependence of the MPs distribution (upper left panel) is very steep, varying by more than 2 orders of magnitude in the inner 50 kpc; into the same region instead VMP/EMP stars (right upper and left lower panels) are much more uniformly distributed.

In Fig. 4.3 we show the radial distribution of these stellar populations, obtained by averaging among 20 different directions passing through the Galactic center but not belonging to the disk plane neither intersecting dwarf satellites. The fits of the two distributions are also provided in the Figure: the radial distribution of MP stars closely follows a power-law in radius, $r^{-\gamma}$, with $\gamma = 2.2$ while that of VMP/EMP stars is well approximated by a β-function, $(1 + (r/r_c)^2)^{-3\beta/2}$, with $\beta = 1$. It follows that the relative contribution to the MDF of more pristine stellar generations becomes gradually more important at large r as was clearly shown by the percentage in Fig. 4.2.

---

[1] Note that these definitions do not exactly correspond to those provided in the acronyms list. We will use them in this Chapter only.

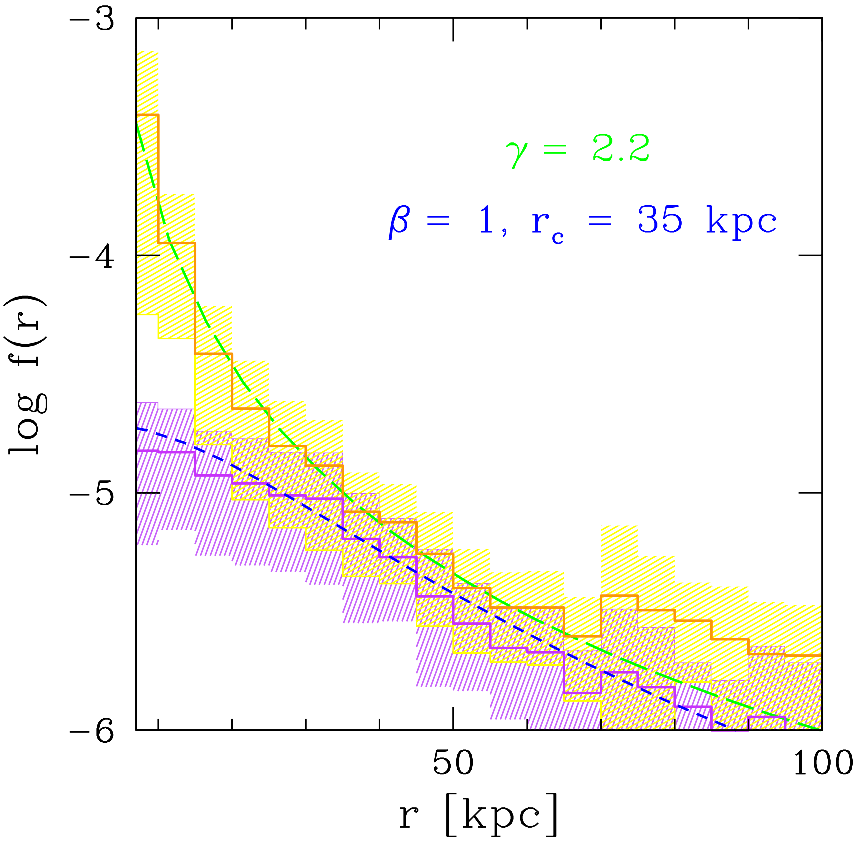

Figure 4.3: Fraction of $-2 <$[Fe/H]< -1 (upper yellow histogram) and [Fe/H]≤ -2 stars (lower violet histogram) with respect to the total stellar mass and in different radial bins. Histograms are the average values among 20 different directions passing through the Galactic center but not belonging to the disk plane neither intersecting dwarf galaxies. The shaded area is the $\pm 1\sigma$ dispersion region. Short- (long-) dashed line is the β-model $(1+(r/r_c)^2)^{-3\beta/2}$ (power-low $r^{-\gamma}$) fit for the stellar distributions.

Coming back to the metallicity maps (Fig. 4.4) we can observe that above $\gtrsim 40$ kpc the density of VMP stars is maximum inside the dwarf satellites, which are clearly identified in the Figure. Interestingly extremely metal-poor stars are found only in two dwarfs and, even in these objects, they represent a sub-dominant stellar population ($\leq 13\%$). Beyond 60 kpc the number of EMPs drops implying that this population is more condensed within such a region. We finally observe that *ghost* Pop III stars were segregated within the central $(30-40)$ kpc region and hosted only by two dwarf satellites.

What determines the spatial distribution of stars with different [Fe/H]? In addition to the underlying structure formation governed by DM, there are two key ingredients: (i) the virialization epoch of the star-forming haloes, which affects the final distribution of DM and hence of stars; (ii) the metal enrichment history of

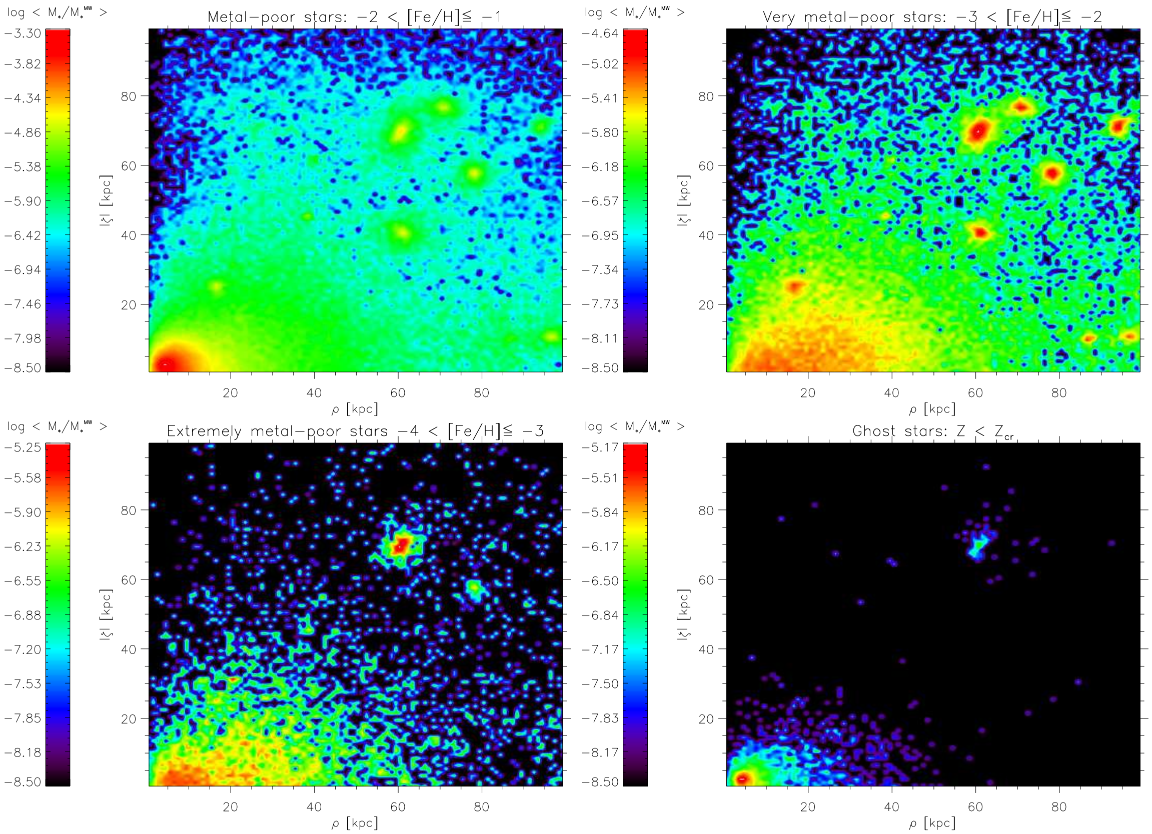

Figure 4.4: Mass distribution of metal-poor (MP) $-2 <$[Fe/H]≤ -1 (left upper panel), very metal-poor (VMP) $-3 <$[Fe/H]≤ -2 (right upper panel), extremely metal-poor (EMP) $-4 <$[Fe/H]≤ -3 (left lower panel), and "ghost", $Z < Z_{cr}$, Pop III stars (right lower panel), in the cylindrical coordinate plane $(r, |\zeta|)$, normalized to the total MW stellar mass in the simulation $M^{*}_{tot} \approx 4 \times 10^{10} M_{\odot}$.

the GM, setting the initial Fe-abundance of the ISM in newly virializing haloes. In Fig. 4.5 we show the average formation redshift of DM particles hosting [Fe/H]< -1 stars, $\langle z \rangle$, in the $\rho - \zeta$ plane. The oldest stars populate the innermost region; moreover, $\langle z \rangle$ gradually decreases with $r = \sqrt{\rho^2 + \zeta^2}$. Beyond $\sim$ 30 kpc on average $\langle z \rangle < 7$. As for $z < 8$ the GM has been already enriched up to [Fe/H]$_{GM} \approx -3$, extremely metal-poor stars become more rare in such outer regions; this explain their spatial condensation. Very metal-poor stars, instead, extend up to 100 kpc as [Fe/H]$_{GM} \approx -2$ when $z = 5$. Finally, as metal-poor stars predominantly form via self-enrichment their spatial distribution is unaffected by the GM enrichment and it is solely determined by hierarchical history of collapsed structures.

A final remark concerns dwarf satellite galaxies. Beyond $\sim$ 30 kpc the dwarf systems can be identified as clumps of high $\langle z \rangle$ against the more uniform background. All satellites found in the simulation are "classical" dwarf galaxies, *i.e.* they have

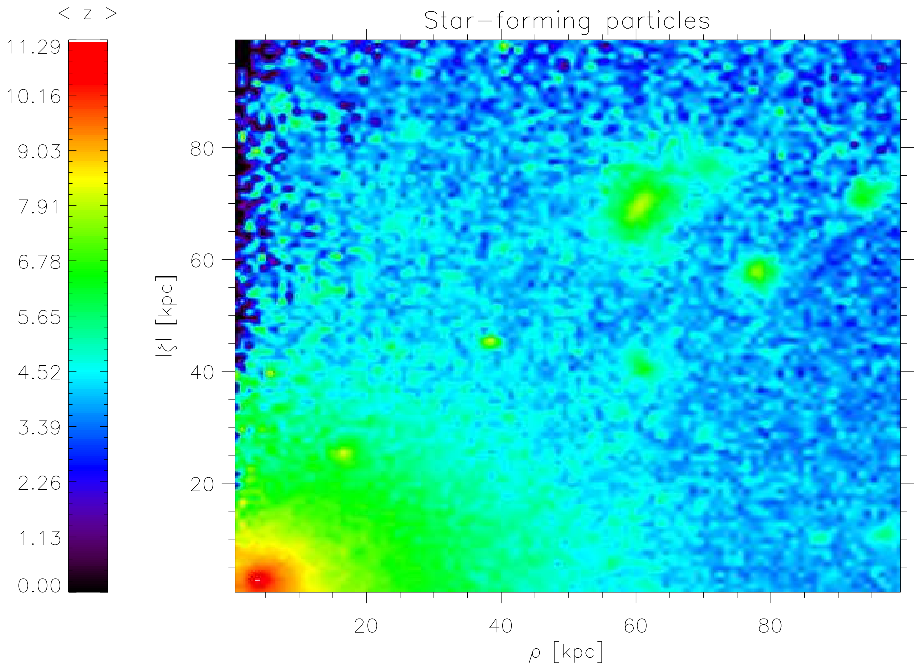

Figure 4.5: Average formation redshift of DM particles hosting [Fe/H]< −1 stars in different regions of the cylindrical coordinate plane $(\rho, |\zeta|)$.

$L > 10^5 L_\odot$. Only two of them, corresponding to rare $> 2\sigma$ fluctuations, were hosting Pop III stars (Fig. 4.4 right down panel) as they virialized and began to form stars when $z > 11$ and $Z_{GM} < Z_{cr}$. The powerful explosions following the evolution of Pop III stars[2] caused the complete blow-away of gas and metals; long-living stars only form at later times when more *pre-enriched* gas is collected by the dwarfs through accretion and merging processes. No clear imprint of their pristine formation can be found in these galaxies, which have similar stellar populations ($\langle$[Fe/H]$\rangle \sim -2$) of "normal" dwarf satellites. Note however that these galaxies represent the most massive dwarfs we found with $M_h = 1 - 2 \times 10^9 M_\odot$ and $M_* = 0.7 - 1.2 \times 10^7 M_\odot$. The remaining 80% of dwarfs correspond to $< 2\sigma$ fluctuations which virialize at later epochs $z = (6 - 8)$ when [Fe/H]$_{GM} > -3$. The lack of [Fe/H]< -3 stars (Helmi et al. 2006) is hence naturally explained in these objects which have a dark matter $M_h = (1 - 7) \times 10^8 M_\odot$ and stellar mass content $M_* = (0.5 - 7.5) \times 10^6 M_\odot$ consistent with that of the observed dwarf spheroidal galaxies.

---

[2] We recall that massive Pop III stars evolve as pair-instability SN. For $m_{\rm PopIII} = 200 M_\odot$, as assumed here, the explosion energy is 2.7×10^{52} erg

4.4 Discussion

Old, [Fe/H]< -2 stars, are intrinsically rare in the Galaxy, representing only $\leq 1\%$ (*i.e.* $\approx 5 \times 10^8 M_\odot$) of the total stellar mass. This makes the selection of very metal-poor stars one of the major issues of stellar surveys devoted to their investigation. In this study we have explored the spatial distribution of such elusive stellar populations by combining the N-body simulation described in Sec. 2.1.1 with our semi-analytical code GAMETE. Our findings show that: (i) the radial distribution of $-2 <$[Fe/H]< -1 stars is very steep, following a power-law, $r^{-\gamma}$, with $\gamma = 2.2$; on the contrary (ii) VMP/EMP stars exhibit a central core for $r < r_c = 35$ kpc, closely following a β-function, $[(1 + (r/r_c)^2]^{-3\beta/2}$, with $\beta = 1$. Hence, though both populations are *more concentrated* toward the center, (iii) the relative contribution of [Fe/H]< -2 stars *increases* from 16% in the inner halo ($r < 20$ kpc) to $> 40\%$ in the outer halo, in good agreement with the results by Carollo et al (2007)[3]. The last finding, combined with the higher concentration of VMP stars within $r < 35$ kpc, and the reduced capability of magnitude limited survey at increasing distances, makes *the outer halo between* 20 *kpc* $\lesssim r \lesssim$ 40 *kpc the most promising region to search for very metal-poor stars.*

The spatial distribution of very/extremely metal-poor stars is imprinted by two physical mechanisms: (i) the natural concentration of old stellar particles toward the more central region of the Galaxy; (ii) the gradual enrichment, through SN-driven outflows, of the MW environment out of which haloes virialize.

Our analysis predicts that *the MDF of [Fe/H]*< -2 *stars weakly varies through the central* 50 *kpc.* Furthermore the all-radii MDF, including all the stars within $r_{vir} = 239$ kpc, satisfactory matches the data once normalized to the number of observed stars. Two immediate consequences arise from these results: (i) the observed sample, which only explored a small portion of the Galactic halo, is a good representation of the complete one; (ii) the results of semi-analytical models, which cannot incorporate the spatial information, can nevertheless be compared with the observations to give reasonable approximate results. The working hypothesis we adopted in the previous Chapter is therefore fully justified.

Beyond 60 kpc the density of very metal-poor stars is maximum inside the "classical" ($L > 10^5 L_\odot$) dwarf galaxies. We find that *8 out of 10 of such objects only host [Fe/H]*> -3 *stars, in agreement with observations by Helmi et al. (2006)*; in the remaining two extremely metal-poor stars represent a sub-dominant stellar population, making up only $\leq 13\%$ of the total stellar mass. Typically these galaxies virialize at $z \sim 6 - 8$, have a total mass $M_h = (1 - 7) \times 10^8 M_\odot$ (*i.e.* they are $< 2\sigma$ fluctuations of the density field), and stellar mass $M_* = (0.5 - 7.5) \times 10^6 M_\odot$. Interestingly, no ultra faint dwarf galaxies ($L < 10^5 L_\odot$) are found in our simulation, confirming that these newly-discovered satellites are probably left-overs of H_2

---

[3] The low-metallicity bias in their data sample, leading to an underestimate of the number of [Fe/H]> -2 stars, prevents a rigorous comparison between simulated and observed MDFs.

cooling mini-haloes (Salvadori & Ferrara 2009), whose physics is not included in the present study. We will discuss this issue in Chapter 7. Note finally that only a very small fraction ($\sim 10\%$) of the dark matter substructures underlined in Fig. 2.1 is found to become visible satellite galaxies, as shown in the maps of Figs. 4.4-4.5. This is a consequence of the $M_{sf}(z)$ evolution assumed equal to $M_4(z)$ when $z > z_{rei} = 6$ and to $M_{30}(z)$ otherwise. Again we will extensively discuss this topic in Chapter 7, while talking about the missing satellites problem.

We devote the final remark to our "perfect mixing" approximation. As the porosity increases rapidly with time ($Q \approx 1$ for $z \approx 7$), the MDFs from the inhomogeneous models are mostly consistent with those derived by using the perfect mixing approximation. For example, the MDFs differences between the two mixing prescriptions (Fig. 4.2, right upper panel) are smaller than the $\pm 1\sigma$ error expected from averaging over different hierarchical merger histories (see Fig. 3.1). On the other hand, the true scatter in [Fe/H] at low metallicities and large radii may be substantially larger than in either of these models, as stars are strongly clustered toward the center of our simulation, which will reduce the true filling factor. This could have a non-negligible effect on the spatial distribution of ghost Pop III stars, which are found to be segregated within the inner ~ 30 kpc region (see for comparison the distribution of the first/second generation stars provided in Scannapieco et al. 2006, which adopted an opposite metal-mixing prescription). The full physical modeling of metal mixing and diffusion remains one of the largest uncertainties in galaxy formation, and more work is required before one can draw definite conclusions.

Chapter 5

The puzzling ^{6}Li plateau

We know that one of the most challenging issues related to the abundances of Galactic halo metal-poor stars concerns the origin of the ^{6}Li and ^{7}Li plateau. The problem can be briefly resumed as follows: observations of the lithium isotopes in the atmosphere of metal-poor halo stars reveal abundances of $^7\mathrm{Li/H} = (1-2) \times 10^{-10}$ and $^6\mathrm{Li/H} = 6 \times 10^{-12}$ *independent* of the stellar [Fe/H]. The presence of such a plateau supports the idea that these lithium isotopes are primary elements, synthesized during the Big Bang Nucleosynthesis (BBN). However, the values predicted by the BBN disagree with those observed: $(^7\mathrm{Li/H})_{\mathrm{BBN}} \sim 4 \times 10^{-10}$ and $(^6\mathrm{Li/H})_{\mathrm{BBN}} \sim 10^{-14}$ (see Sec. 1.5.1 for all the references). The discrepancy of the ^{7}Li abundance is only marginal; in addition mixing and diffusion processes during stellar evolution could reduce the predicted value by about 0.2 dex (Pinsonneault et al. 2002; Korn et al.2006), thus releasing the discrepancy. A more serious issue, instead, is represented by ^{6}Li whose observed abundance results more than 2 orders of magnitude higher than the predicted one.

Three main solutions have been proposed to overcome this problem: (i) a modification of BBN models (Kawasaki et al. 2005; Jedamzik et al. 2006; Pospelov 2007; Cumberbatch et al. 2007; Kusakabe et al. 2007), (ii) the fusion of ^{3}He accelerated by stellar flares with the atmospheric helium (Tatischeff & Thibaud 2007), (iii) a mechanism allowing for later production of ^{6}Li during Galaxy formation. The latter scenario involves the generation of cosmic rays (CRs). ^{6}Li, in fact, can be synthesized by fusion reactions ($\alpha + \alpha \rightarrow {}^6\mathrm{Li}$) when high-energy CR particles collide with the ambient gas. Energetic CRs can either be accelerated by shock waves produced during cosmological structure formation processes (Miniati 2000; Suzuki & Inoue 2002; Keshet 2003) or by strong supernova (SN) shocks along the build-up of the Galaxy.

In their recent work Rollinde, Vangioni & Olive (2006) used the supernova rate (SNR) by Daigne et al. (2006) to compute the production of ^{6}Li in the IGM. Assuming that all metal-poor halo stars form at $z \sim 3$, and from a gas with the same IGM composition, they obtained the observed ^{6}Li value. Despite the apparent success of the model, these assumptions are very idealized and require a closer inspection. In this Chapter we revisit this solution by using our code GAMETE that provides a more realistic and data-constrained approach to the problem. Indeed, the gradual enrichment of the gas and the formation of the subsequent stellar populations is followed self-consistently along the hierarchical tree, and both the global properties of the MW and the Galactic halo MDF are well reproduced.

5.1 Modeling the ^{6}Li production by cosmic rays

5.1.1 Star formation rate

We use GAMETE in order to compute the global Milky Way star formation rate (SFR), both for Pop III and Pop II/I stars, and the metallicity evolution of the MW environment. As usual we assume our fiducial observation-calibrated model with $m_{PopIII} = 200M_{\odot}$ and $Z_{cr} = 10^{-4}Z_{\odot}$, and we use a statistically significant sample of different hierarchical merger histories (100). In Fig. 5.1 (upper panel) the derived Galactic (comoving) SFR density is shown for Pop III and Pop II/I stars. We immediately observed that Pop II/I stars dominate the SFR at any redshift, in agreement with our findings in Fig. 2.5 (right panel). As pointed out in Sec. 2.3.2 indeed, following a burst of Pop III stars the metallicity of the host halo raises to $Z > Z_{cr}$ meaning that chemical feedback suppress the Pop III star formation in self-enriched progenitors. Hence Pop III stars can only form in those haloes which virialize from the GM and so, as soon as $Z_{\rm GM} \gtrsim Z_{cr}$ ($z \approx 10$), their formation is totally quenched. The above results are in agreement with recent hydrodynamic simulations implementing chemical feedback effects (Tornatore et al. 2007). The earlier Pop III disappearance of our model ($z \sim 10$) with respect to this study ($z \sim 4$) is a consequence of the biased volume we consider *i.e.* the MW environment. As the higher mean density accelerates both the star formation and metal enrichment, PopIII stars disappear at earlier times; the SFR maximum value and shape, however, match closely the simulated ones.

In Fig. 5.1 (lower panel) we show the corresponding evolution of the GM iron and oxygen abundance that we already know. The small differences with respect to Fig. 2.7 are a consequence of the different prescription adopted to model mechanical feedback (Sec. 4.1). In Sec. 2.3.2 we showed that the present-day stars with [Fe/H]<-2.5 formed in haloes accreting gas from the GM, Fe-enhanced by previous SN explosions. Therefore the initial [Fe/H] abundance of the gas within a halo is set by the corresponding [Fe/H] abundance of the MW environment at its virialization redshift.

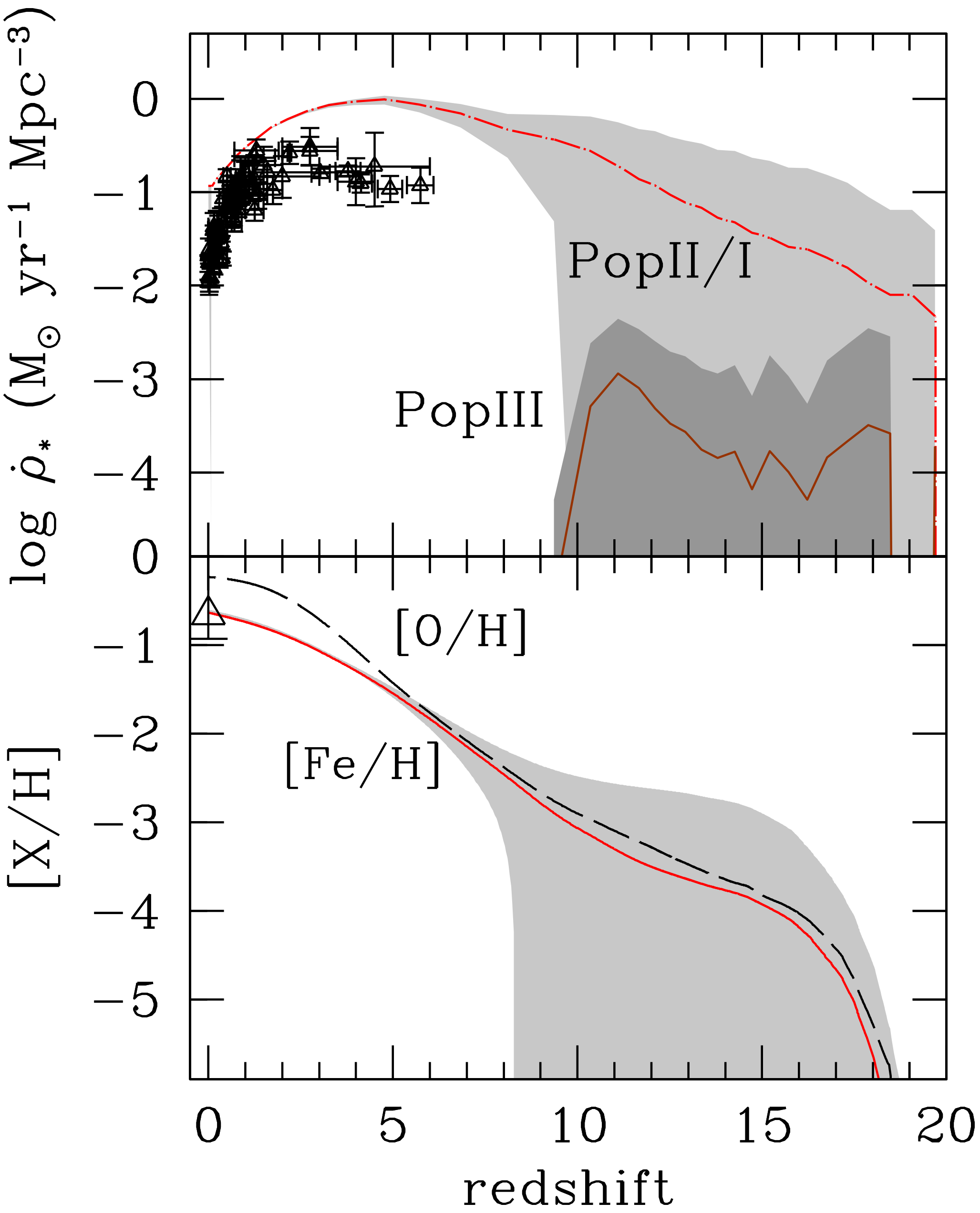

Figure 5.1: *Upper panel*: Comoving SFR density evolution for Pop III (solid line) and Pop II/I stars (dashed line). The curves are obtained after averaging over 100 realizations of the merger tree; shaded areas denote ±1σ dispersion regions around the mean. Points represent the low-redshift measurements of the cosmic SFR by Hopkins (2004). *Lower panel*: Corresponding GM iron (solid line) and oxygen (dashed line) abundance evolution. The point is the measured [O/H] abundance in high-velocity clouds by Ganguly et al. (2005).

5.1.2 Lithium production

To describe the production of ^{6}Li for a continuous source of CRs we generalize the classical work of Montmerle (1977), who developed a formalism to follow the propagation of an homogeneous CR population in an expanding universe, assuming that CRs have been instantaneously produced at some redshift.

Since the *primary* CRs are assumed to be produced by SNe, the physical source function $\mathcal{S}(E,z)$ is described by a power law in momentum:

$$\mathcal{S}(E,z) = C(z)\frac{\phi(E)}{\beta(E)}\ (\mathrm{GeV/n})^{-1}\,\mathrm{cm}^{-3}\,\mathrm{s}^{-1} \tag{5.1}$$

with $\beta = v/c$ and

$$\phi(E) = \frac{E+E_0}{[E(E+2E_0)]^{(\gamma+1)/2}}\ (\mathrm{GeV/n})^{-1}\,\mathrm{cm}^{-2}\,\mathrm{s}^{-1} \tag{5.2}$$

where γ is the injection spectral index and $E_0 = 939$ MeV and E are, respectively, the rest-mass energy and the kinetic energy per nucleon. The functional form of the injection spectrum $\phi(E)$ is inferred from the theory of collisionless shock acceleration (Blandford & Eichler 1987) and the γ value is the one typically associated to the case of strong shock. We note however that the results are only very weakly dependent on the spectral slope. Finally, $C(z)$ is a redshift-dependent normalization; its value is fixed at each redshift by normalizing $\mathcal{S}(E,z)$ to the total kinetic energy transferred to CRs by SN explosions:

$$\mathcal{E}_{\mathrm{SN}}(z) = \int_{E_{\mathrm{min}}}^{E_{\mathrm{max}}} E\mathcal{S}(E,z)\mathrm{d}E \tag{5.3}$$

with

$$\mathcal{E}_{\mathrm{SN}}(z) = \varepsilon(1+z)^3[E_{\mathrm{II}}\mathrm{SNR}_{\mathrm{II}}(z) + E_{\gamma\gamma}\mathrm{SNR}_{\gamma\gamma}(z)] \tag{5.4}$$

where $E_{\mathrm{II}} = 1.2 \times 10^{51}$ erg and $E_{\gamma\gamma} = 2.7 \times 10^{52}$ erg are, respectively, the average explosion energies for a Type II SN ($\mathrm{SN_{II}}$) and a $\mathrm{SN}_{\gamma\gamma}$; $\varepsilon = 0.15$ is the fraction of the total energy not emitted in neutrinos transferred to CRs by a single SN, assumed to be the same for the two stellar populations; $\mathrm{SNR_{II}}$ ($\mathrm{SNR}_{\gamma\gamma}$) is the $\mathrm{SN_{II}}$ ($\mathrm{SN}_{\gamma\gamma}$) explosion comoving rate, simply proportional to the Pop II/I (Pop III) SFR. The efficiency parameter is inferred by shock acceleration theory and confirmed by recent observations of SN remnants in our Galaxy (Tatischeff 2008).

We now need to specify the energy limits E_{min}, E_{max} of the CR spectrum produced by SN shock waves (eq. 5.3). We fix $E_{\mathrm{max}} = 10^6$ GeV, following the theoretical estimate by Lagage & Cesarsky (1983). Due to the rapid decrease of $\phi(E)$ the choice of E_{max} does not affect the result of the integration and hence the derived $C(z)$ value. On the contrary $C(z)$ strongly depends on the choice of E_{min}: the higher E_{min}, the higher is $C(z)$. Since observations cannot set tight constraints on $E_{\rm min}$, due to solar magnetosphere modulation of low-energy CRs, we consider it as a free parameter of the model.

Once the spectral shape of $\mathcal{S}(E,z)$ is fixed, we should in principle take in account the subsequent propagation of CRs both in the ISM and GM. Following Rollinde et al (2006), we make the hypothesis that primary CRs escape from parent galaxies on a timescale short enough to be considered as immediately injected in the GM without energy losses. At high redshift in fact: (i) structures are smaller and less dense (Zhao et al. 2003) implying higher diffusion efficiencies (Jubelgas et al. 2006); (ii) the magnetic field is weaker and so it can hardly confine CRs into structures. Note also that, besides diffusive propagation of CRs, superbubbles and/or galactic winds could directly eject CRs into the GM.

Under this hypothesis the density evolution of primary CRs only depends on energy losses suffered in the GM. The nuclei lose energy mainly via two processes, ionization and Hubble expansion, and they are destroyed by inelastic scattering off GM targets (mainly protons).

We can follow the evolution of α-particles (primary CRs) through the transport equation (Montmerle 1977)

$$\frac{\partial N_{\alpha,\rm H}}{\partial t} + \frac{\partial}{\partial E}(bN_{\alpha,\rm H}) + \frac{N_{\alpha,\rm H}}{T_D} = K_{\alpha p}\mathcal{S}_{,\rm H}(E,z) \tag{5.5}$$

where $N_{i,H}$ is the ratio between the (physical) number density of species i and GM protons, $n_H(z) = n_{\rm H,0}(1+z)^3$; $\mathcal{S}_{,\rm H}(E,z) \equiv \mathcal{S}(E,z)/n_{\rm H}(z)$ is the normalized physical source function, $b \equiv (\partial E/\partial t)$ is the total energy loss rate adopted from Rollinde et al. (2006), T_D is the destruction term as in the analytic fit by Heinbach & Simon (1995); finally, $K_{\alpha p} = 0.08$ is the cosmological abundance by number of α-particles with respect to protons.

We consider ^{6}Li as entirely secondary, *i.e.* purely produced by fusion of GM He-nuclei by primary α-particles. The physical source function for ^{6}Li is given by:

$$\mathcal{S}_{\rm 6Li}(E,z) = \int \sigma_{\alpha\alpha\to{\rm 6Li}}(E,E')n_{\rm He}(z)\Phi_\alpha(E',z){\rm d}E' \tag{5.6}$$

where E' and E are respectively the kinetic energies per nucleon of the incident particle and of the produced ^{6}Li nuclei, and $\Phi_\alpha(E',z) = \beta(E')N_\alpha(E',z)$ the incident α-particle flux. Making the approximation $\sigma_{\alpha\alpha\to{\rm 6Li}}(E,E') = \sigma_l(E)\delta(E-E'/4)$ (Meneguzzi et al. 1971) and defining $\mathcal{S}_{\rm 6Li,H} \equiv \mathcal{S}_{\rm 6Li}/n_{\rm H}$, the eq. (5.6) becomes

$$\mathcal{S}_{\rm 6Li,H}(E,z) = \sigma_l(E)K_{\alpha p}n_{\rm H}(z)\Phi_{\alpha,\rm H}(4E,z) \tag{5.7}$$

where the cross section $\sigma_l(E)$ is given by the analytic fit of Mercer et al. (2001):

$$\sigma_l(E) \sim 66\exp\left(-\frac{E}{4\ {\rm MeV}}\right)\ {\rm mb} \tag{5.8}$$

We can now write a very simple equation describing the evolution of ^{6}Li:

$$\frac{\partial N_{6\mathrm{Li,H}}}{\partial t} = \mathcal{S}_{6\mathrm{Li,H}}(E, z) \tag{5.9}$$

in this case, in fact, destruction and energy losses are negligible since their time scales are very long with respect to the production time scale (Rollinde et al. 2005).

The solution of the coupled eqs. (5.5)-(5.9) gives ^{6}Li/H at any given redshift z.

5.2 The ^{6}Li evolution

The system of equations introduced in the previous Section are solved numerically using a Crank-Nicholson implicit numerical scheme (Press 2002). Because of its stability and robustness implicit schemes are used to solve transport equations in most CRs diffusion problems (Strong & Moskalenko 1998).

We test the accuracy of our code by studying a simplified case in which an analytic solution can be derived and compared with numerical results. To this aim we assume that: (i) both energy losses and destruction of primary CRs in the GM can be neglected; (ii) the physical energy density injected by SN is constant, $\mathcal{E}_{\mathrm{SN}} \sim 7.4 \times 10^{-27}$ GeV cm^{-3} s^{-1}, in the redshift range $z > 3$. It is worth noting that the above hypothesis conspire to give an upper limit to the exact solution, thus providing an estimate of the maximum achievable ^{6}Li abundance. Under these approximations, the source spectrum defined in eq. (5.1) becomes:

$$\mathcal{S}(E, z) = 6.4 \cdot 10^{-29} \frac{\phi(\mathrm{E})}{\beta(\mathrm{E})}\ (\mathrm{GeV/n})^{-1}\,\mathrm{cm}^{-3}\,\mathrm{s}^{-1} \tag{5.10}$$

and eqs. (5.5)-(5.9) can be solved. We find

$$N_{\alpha,\mathrm{H}}(z) = 39.6\,(1+z)^{-9/2} \tag{5.11}$$

and

$$N_{6\mathrm{Li,H}}(z) = 8.2 \times 10^{-11}(1+z)^{-3} \tag{5.12}$$

From Fig. 5.2 we conclude that the analytical solution for the GM ^{6}Li abundance (eq. 5.12) is perfectly matched by the numerical[1] one. Also shown are the numerical solutions obtained by relaxing first the hypothesis (i) and then (i) + (ii). Not unexpectedly, the inclusion of energy losses and destruction term into eq. (5.5) affects only slightly the result, as the typical time-scales of such processes are longer than the ^{6}Li production one.

---

[1] This solution represents an upper limit for the Rollinde et al. (2006) model, as inferred from their Fig. 2.

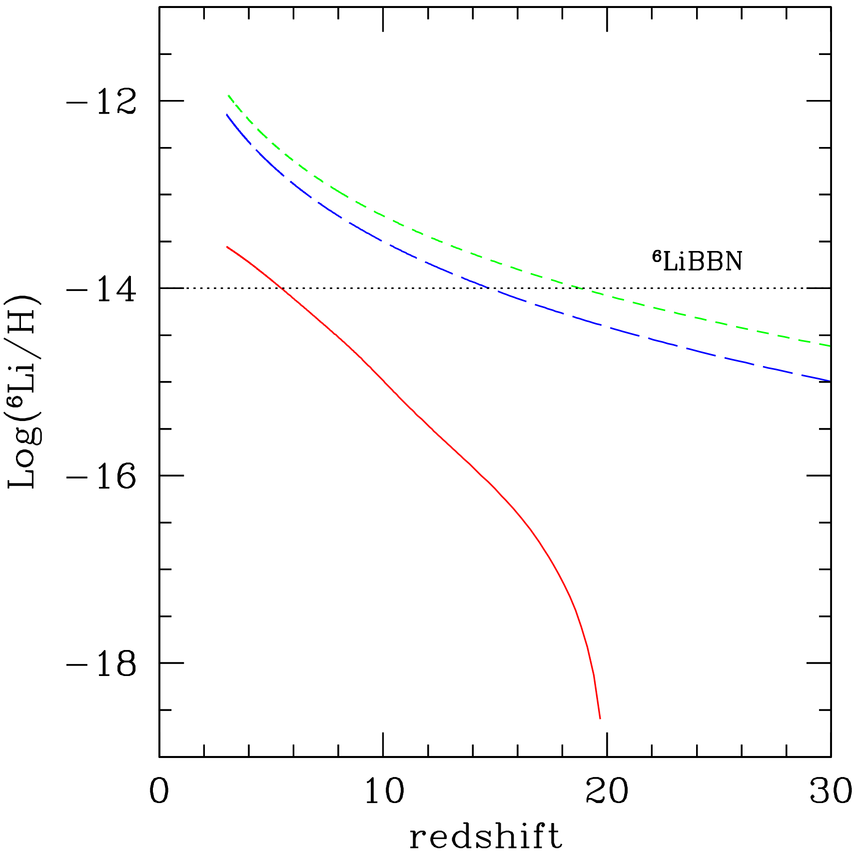

Figure 5.2: Redshift evolution of GM ^{6}Li/H abundance for the analytical (green short-dashed line) and numerical solution (overlapped) of a simplified model with no energy losses and destruction, and $\mathcal{E}_{\rm SN} = 7.4 \times 10^{-27}$ GeV cm^{-3} s^{-1} for $z > 3$, the same model including energy loss/destruction (blue long dashed line), the fiducial model with realistic SNR, $\varepsilon = 0.15$ and $E_{\rm min} = 10^{-5}$ MeV (red solid line). The horizontal dotted line shows the ^{6}Li/H abundance predicted by the BBN.

A realistic injection energy, on the contrary, has a strong impact on the predicted shape and amplitude of the ^{6}Li evolution. In fact, the SFR, and consequently $\mathcal{E}_{\rm SN}$, is an increasing function of time in the analyzed redshift range (Fig. 5.1 upper panel). The maximum $\mathcal{E}_{\rm SN}$ we can obtain by using the SNR derived from the curve in Fig. 5.1, a realistic energy transfer efficiency $\varepsilon = 0.15$, and $E_{\rm min} = 10^{-5}$ GeV (Rollinde et al. 2006), is $\mathcal{E}_{\rm SN}^{max} \sim 8.6 \times 10^{-28} < 7.4 \times 10^{-27}$ GeV cm^{-3} s^{-1}. Note that the ^{6}Li/H abundance at $z = 3$ results more than 1 order of magnitude smaller than the value of the simplified case. In the following, we will refer to this physical model as our fiducial model.

5.3 ^{6}Li abundance in metal-poor halo stars

We can now use the [Fe/H] predicted by GAMETE (Fig. 1, lower panel) to convert redshift into [Fe/H] values and derive the GM ^{6}Li vs [Fe/H]. According to our semi-analytical model for the build-up of the MW, in fact, the GM elemental abundances reflect those of metal-poor halo stars, which are predicted to form out of new virializing haloes accreting gas from the GM (Sec. 2.3.2). This implies that the observed metal-poor halo stars formed continuously within the redshift range $3 < z \leq 10$. From Fig. 5.3 we see that our fiducial model yields log ^{6}Li/H$= -13.5$, *i.e.* about three orders of magnitude below the data.

This discrepancy cannot be cured by simply boosting the free parameters to their maximum allowed values. This is also illustrated in the same Figure, where for the upper curve we assume $\varepsilon = 1$, $E_{\rm min} = 10$ MeV/n[2] and for the SFR the maximum value allowed by GAMETE within 1-σ dispersion. Although the discrepancy between observations and model results is less prominent in this case, we are still unable to fit the data, in particular at [Fe/H] $= -3$ (*i.e.* at higher redshifts) only Log ^{6}Li/H$= -12.6$ has had time to be produced, failing short by 30 times.

In addition the flat data distribution cannot be recovered. It is worth noting that, as also pointed out by Asplund et al. (2006) ^{6}Li may be depleted in stars, mainly during the pre-main sequence phase. If this is the case, the ^{6}Li abundance observed in stars would not be representative of the gas from which they have formed. Taking into account this effect the inferred ^{6}Li abundances become metallicity dependent, *i.e.* the flatness is lost. Because of depletion however, the derived ^{6}Li values would be higher for all [Fe/H], making the discrepancy between our results and observations even larger.

We finally note, as already claimed by Rollinde et al. (2006), that the production of ^{7}Li through this mechanism is comparable with that of ^{6}Li , being the production cross sections of the two isotopes very similar. No overproduction of ^{7}Li is then expected with respect of the BBN-based value.

5.4 Summary and discussion

We have investigated the production of ^{6}Li via cosmic ray spallation along the build-up of the MW by using the data-constrained framework provided by GAMETE. According to our results both the level and flatness of the ^{6}Li distribution cannot be explained by CR spallation if these particles have been accelerated by SN shocks inside MW building blocks. Although previous claims (Rollinde et al. 2006) of a

---

[2] This value is exceptionally high and corresponds to the energy at which the ^{6}Li production is most efficient. Thus the ^{6}Li production will be drastically reduced by increasing $E_{\rm min}$ above this value.

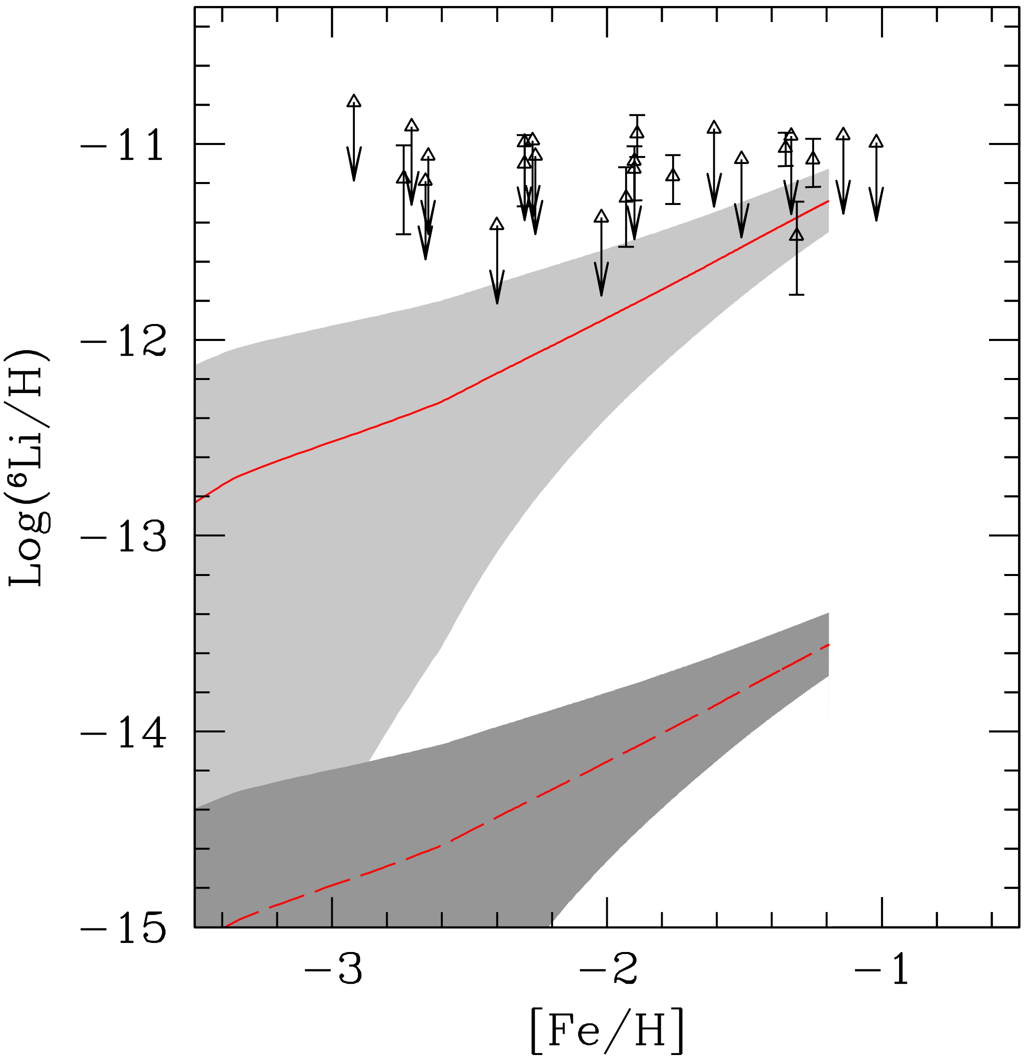

Figure 5.3: Redshift evolution of ^{6}Li/H vs [Fe/H] for the fiducial model ($\varepsilon = 0.15$, $E_{\rm min} = 10^{-5}$ GeV/n, dashed line) and for the maximal model ($\varepsilon = 1$, $E_{\rm min} = 10$ MeV/n, solid line). Shaded areas denote $\pm 1\sigma$ dispersion regions around the mean. Points are the observed abundances by Asplund et al. (2006), with arrows denoting 3σ upper limits to the ^{6}Li abundance.

possible solution[3] invoking the production of ^{6}Li in an early burst of Pop III stars have been put forward, such scenario is at odd with both the global properties of the Milky Way and its metal-poor halo stars.

Our model, which follows in detail the hierarchical build-up of the MW and reproduces correctly the MDF of the metal-poor Galactic halo stars, predicts a monotonic increase of ^{6}Li abundance with time, and hence with [Fe/H]. Moreover, our fiducial model falls short of three orders of magnitude in explaining the data; such discrepancy cannot be cured by allowing the free parameters ($E_{\rm min}, \varepsilon$) to take their maximum (physically unlikely) values. Apparently, a flat ^{6}Li distribution appears inconsistent with any (realistic) model for which CR acceleration energy is tapped from SNe: if so, ^{6}Li is continuously produced and destruction mechanisms are too inefficient to prevent its abundance to steadily increase along with [Fe/H].

Clearly, the actual picture could be more complex: for example, if the diffusion coefficient in the ISM of the progenitor galaxies is small enough, ^{6}Li could be produced *in situ* rather than in the more rarefied GM. This process might increase the species abundance, but cannot achieve the required decoupling of ^{6}Li evolution from the enrichment history.

Alternatively, shocks associated with structure formation might provide a different ^{6}Li production channel involving CRs spallation (Suzuki & Inoue 2002); although potentially interesting as this mechanisms decouples metal enrichment, which is governed by SNe, and CR acceleration, which instead is due to structure formation shocks, this scenario has to face two main difficulties: (i) at redshifts $z \approx 2-3$, at which shocks are most efficient, the star-forming gas must be still [Fe/H]< -3, and (ii) metal-poor halo stars that formed at earlier epochs should have vanishing ^{6}Li abundance (Prantzos et al. 2006). According to the picture provided by GAMETE Galactic halo stars with [Fe/H]< -2.5 form in newly virializing haloes accreting gas from the Galactic Medium (Fig. 2.6). Since [Fe/H]$_{GM} > -1.5$ when $z = 3$ (Fig. 5.1, lower panel) this implies that such alternative solution must also be excluded.

We conclude that more exotic models involving either suitable modifications of BBN or some yet unknown production mechanism *unrelated to cosmic SF history* have to be invoked in order to solve the problem.

---

[3] Note that their eq. 18 contains an extra dz/dt term

Chapter 6

Feedback imprints in dSphs

We know that feedback processes strongly affect the formation and evolution of dwarf galaxies. In this Chapter we will focus on the most common dwarf satellites in the Milky Way system, the dwarf spheroidal galaxies (dSphs). We saw that these MW companions, though characterized by very different star formation histories, are all lacking of gas, ongoing star formation, and all display the presence of an ancient stellar population (> 10 Gyr). The latter feature implies that dSphs can provide crucial insights on feedback processes driving the early phases of the MW formation.

The large amount of available data for these nearby satellites, observed since many decades, contrast with the lack of a comprehensive scenario for their formation and evolution. During the past years several authors have focused in investigating different aspects of the evolution of classical ($L_{tot} > 10^5 L_{\odot}$) dSphs and on the observed properties related with them, giving important contributions to our actual understanding of such puzzling objects. The main subjects explored are summarized in the following list:

- *Origin and dark matter content*: Bullock et al. (2001); Mayer et al. (2002); Kravtsov et al. (2004); Ricotti & Gnedin (2005); Gnedin & Kravtsov (2006); Read, Pontzen & Viel (2006); Moore et al. (2006); Metz & Kroupa (2007); Klimentowski et al. (2009); Li et al. (2009); Kravtsov (2009).

- *Star formation histories and abundance ratios*: Ikuta & Arimoto (2002); Fenner et al. (2006); Lanfranchi & Matteucci (2007); Stinson et al. (2007); Valcke et al. (2008); Revaz et al. (2009); Calura & Menci (2009); Sawala et al. (2009).

- *Internal kinematic and chemistry*: Kawata et al. (2006); Marcolini et al. (2008).

- *Gas content: stellar feedback and tidal stripping*: MacLow & Ferrara (1999); Ferrara & Tolstoy (2000); Tassis et. al (2003); Marcolini et al. (2003); Fujita et al. (2004); Mayer et al. (2006); Lanfranchi & Matteucci (2007); Klimentowski et al. (2009); Peñarrubia et al. (2009).

- *Metallicity distribution function*: Ripamonti et al. (2006); Prantzos (2008); Revaz et al. (2009); Calura & Menci (2009); Sawala et al. (2009).

In spite of the huge amount of theoretical work many questions remain unanswered, and models able to *simultaneously* reproduce several observed properties of dSphs are still missing. In particular none of them can account for the lack of [Fe/H]< -3 stars, matching correctly the observed stellar MDFs (Helmi et al. 2006).

In this Chapter we will use our code GAMETE in order to investigate the formation and evolution of dSphs in their own cosmological context. This approach provides a self-consistent description of the dSphs evolution and MW formation: the dwarf satellites form out from their natural birth environment, the Milky Way environment, whose metallicity evolution is completely determined by the history of star formation and mechanical feedback processes along the build-up of the Galaxy.

6.1 New Features of the model

We first discuss the additional features we have incorporated in the model. The aim of introducing these new physics is to obtain a more complete description of the evolution of a single dSph galaxy. These can be summarized as follows:

- *Infall rate.* The gas in newly virialized haloes is accreted with an infall rate given by

$$\frac{dM_{inf}}{dt} = A\left(\frac{t}{t_{inf}}\right)^2 \exp\left(-\frac{t}{t_{inf}}\right). \tag{6.1}$$

  The selection of this particular functional form has been guided by the results of simulations presented in Kereš et al. (2005). For reasons that will be clarified in Sec. 6.3.1, the infall time is assumed to be proportional to the free-fall time, $t_{inf} = t_{ff}/4$ where $t_{ff} = (3\pi/32G\rho)^{1/2}$, G is the gravitational constant, and ρ is the total (dark + baryonic) mass density of the halo. The normalization constant is set to be $A = 2(\Omega_b/\Omega_m)M/t_{inf}$ so that for $t \to \infty$ the accreted gas mass reaches the universal value $M_{inf}(\infty) = (\Omega_b/\Omega_m)M$. No infall is assumed after a merging event *i.e.* all the gas is supposed to be instantaneously accreted. Hydrodynamical simulations in fact show that galaxy mergers can drive significant inflow of gas raising the star formation rate by more than an order of magnitude (Mihos & Hernquist, 1996 and references therein).

- *Finite stellar lifetimes.* We follow the chemical evolution of the gas taking into account that stars of different masses evolve on characteristic time-scales

(Lanfranchi & Matteucci 2007). The rate at which gas is returned to the ISM through winds and SN explosions is computed as:

$$\frac{dR(t)}{dt} = \int_{m_1(t)}^{100M_\odot} (m - w_m(m))\Phi(m)\mathrm{S}FR(t-\tau_m)dm, \tag{6.2}$$

where $\tau_m = 10/m^2$ Gyr is the lifetime of a star with mass m, w_m is the remnant mass and $m_1(t)$ the turnoff mass *i.e.* the mass corresponding to $t = \tau_m$. Similarly, the total ejection rate of an element i, newly synthesized inside stars (first term in the parenthesis) and re-ejected into the ISM without being re-processed (second term), is

$$\frac{dY_i(t)}{dt} = \int_{m_1(t)}^{100M_\odot} [(m - w_m(m) - m_i(m,Z))\times \tag{6.3}$$

$$Z_i(t-\tau_m) + m_i(m,Z)]\Phi(m)\mathrm{S}FR(t-\tau_m)dm,$$

where $m_i(m,Z)$ is the mass of element i produced by a star with initial mass m and metallicity Z and $Z_i(t-\tau_m)$ is the abundance of the $i-th$ element at the time $t-\tau_m$. The SN rate is simply computed as

$$\frac{dN_{SN}(t)}{dt} = \int_{m_1(t)>8M_\odot}^{40M_\odot} \Phi(m)\mathrm{S}FR(t-\tau_m)dm. \tag{6.4}$$

As usual we used the grid of values $w_m(m)$ and $m_i(m,Z)$ by Heger & Woosley (2002) for $140M_\odot < m < 260M_\odot$, Woosley & Weaver (1995) for $8M_\odot < m < 40M_\odot$ and van der Hoek & Groewengen (1997) for $0.9M_\odot < m < 8M_\odot$.

- *Differential winds.* The gas ejected out of the host halo is assumed to be metal-enhanced with respect to the star forming gas. According to Vader (1986), who studied SN-driven gas loss during the early evolution of elliptical galaxies, the SN ejecta suffer very limited mixing before they leave the galaxy, playing a minor role in its chemical evolution. Such hypothesis implies different ejection efficiency for gas and metals. This result has been later confirmed by numerical studies (Mac Low & Ferrara, 1999; Fujita et al. 2004). Adopting a simple prescription, we assume that the abundance of the $i-th$ element in the wind is proportional to its abundance in the ISM, $Z_i^w = \alpha Z_i^{ISM}$, and we take $\alpha = 10$ only for newly virialized haloes ($M < 10^9 M_\odot$) otherwise $\alpha = 1$.

For any star forming halo of the MW hierarchy, we therefore solve the following system of differential equations:

$$\mathrm{S}FR = \epsilon_* \frac{M_g}{t_{ff}}, \tag{6.5}$$

$$\frac{dM_g}{dt} = -\mathrm{S}FR + \frac{dR}{dt} + \frac{dM_{inf}}{dt} - \frac{dM_{ej}}{dt}, \tag{6.6}$$

$$\frac{dM_{Z_i}}{dt} = -Z_i^{ISM}\mathrm{S}FR + \frac{dY_i}{dt} + Z_i^{vir}\frac{dM_{inf}}{dt} - Z_i^{w}\frac{dM_{ej}}{dt}. \tag{6.7}$$

The first equation is simply the star formation rate; M_g is the mass of cold gas inside haloes, ϵ_* the usual free parameter controlling the star formation efficiency, and t_{ff} the free-fall time. The second equation describes the mass variation of cold gas: it increases because of gas infall and/or returned from stars and decreases because of star formation and gas ejection into the GM. The third equation, analogous to the second one, regulates the mass variation of an element i; Z_i^{ISM}, Z_i^{vir}, and Z_i^w are the abundance of the $i-th$ element in the ISM, in the infalling gas (*i.e.* in the hot gas at virialization), and in the wind, respectively.

6.1.1 Model parameters

The model is now characterized by six free parameters: ϵ_*, ϵ_w, Z_{cr}, m_{PopIII}, t_{inf} and α. As usual we calibrate ϵ_* and ϵ_w by matching the global properties of the Milky Way (Sec. 2.3) and we fix Z_{cr} and m_{PopIII} in order to reproduce the observed Galactic halo MDF (Fig. 6.1, left panel). We can see that the agreement between the observed and simulated MDF is very good. Note that because of the relaxed IRA and of assumed infall rate, metals are now more efficiently diluted inside haloes, and the MDF is better matched by assuming $Z_{cr} = 10^{-3.8}Z_{\odot}$. Nevertheless [Fe/H]$< -2.5$ stars are still found to be mostly produced in newly virializing haloes, accreting metal-enriched gas from the MW environment. The two additional free parameters introduced in the model, t_{inf} and α, are fixed in order to match the observed Sculptor MDF *without altering* the MW properties as we will discuss in detail in Sec. 6.3.1. Our fiducial model is characterized by the following parameter values[1]: $\epsilon_* = 1$, $\epsilon_w = 0.002$, $Z_{cr} = 10^{-3.8}Z_{\odot}$, $m_{PopIII} = 200M_{\odot}$, $t_{inf} = t_{ff}(z_{vir})/4$ and $\alpha = 10$. Once fixed, the parameters are used to solve the system of equations (6.5)-(6.7) for *all* the progenitor haloes of the MW.

6.2 Life and times of dSphs

In the following Sections we will describe the evolutionary scenario of a typical dSph galaxy provided by our model, from its birth to the present day.

---

[1] The difference of ϵ_*, ϵ_w values with respect to those found in Chapter 3 is a result of model improvements. Note however that the integrals of the star formation rate and the gas ejection rate from progenitor haloes remain unaltered.

6.2.1 The birth environment

The first point to address is the selection criteria to identify dSphs among various MW progenitors. We use two criteria: the first is based on dynamical arguments and the second on reionization.

We want to select virializing haloes which could become dSph satellites. Using N-body cosmological simulations, Diemand, Madau & Moore (2005) show that in present-day galaxies, haloes corresponding to rare high-σ density peaks are more centrally concentrated. The probability of a protogalactic halo to become a satellite increases if it is associated with lower-σ density fluctuations. This result, combined with the fact that at each redshift 95% of the total dark matter lies in haloes with mass $M < M_{2\sigma}$, which correspond to $< 2\sigma$ fluctuations, suggest that most satellites originate from such density peaks. Note that our findings in Chapter 4 confirm this thesis, as 8 out of 10 of the dwarf galaxies identified at $z = 0$ were associated to $< 2\sigma$ fluctuations at their formation epoch. Therefore, we select dSph candidates from haloes with masses $M_4 < M < M_{2\sigma}$. In Fig.6.1 (right panel) we show the redshift evolution of $M_4(z)$, defined in Sec. 2.2.2 as $M_4(z) = 10^8 M_\odot[(1+z)/10]^{-3/2}$, and of the halo masses corresponding to $1-3\ \sigma(M,z)$ density peaks. Note that, in addition, the adopted dynamical criterion can be used to set an upper limit to the dSph candidates formation epoch of $z_{vir} < 9$ (see the Figure).

The second criterion is based on reionization. We discussed in Sec. 1.3.1 that during this epoch the increase of the IGM temperature causes the growth of the Jeans mass and consequent suppression of gas infall in low-mass objects. In particular, cosmological simulations by Gnedin (2000) show that below a characteristic halo mass-scale the gas fraction is drastically reduced compared to the cosmic value. We adopt again the simple prescription introduced in Chapter 4 and assume that the formation of galaxies with circular velocity $v_c < 30$ km/s is suppressed after reionization, meaning that when $z < z_{rei}$ haloes with masses below $M_{30}(z)$ have no gas. Since $M_{30}(z) > M_4(z)$ (see the right panel of Fig. 6.1) and the probability to form a newly virialized halo with $M > M_{30}$ is very low, the second criterion implies that the formation of dSph candidates is unlikely to occur below z_{rei}.

Following the two above criteria, dSph candidates can only form in the redshift range $z_{rei} < z_{vir} < 9.$[2]. From the lower panel of Fig. 5.1, which reflects the derived Fe-evolution of the GM (see the middle panel of Fig. 1. in Salvadori, Ferrara & Schneider 2008), it is evident that in this redshift range the mean GM iron abundance is $-2 \lesssim$ [Fe/H] $\lesssim -3$. This implies that the birth environment of dSph candidates is naturally pre-enriched to [Fe/H] values consistent with the observations by Helmi et al.(2006).

In what follows, we will present the results obtained by our fiducial model averaged over 100 different realizations of the hierarchical merger tree of the MW. In

---

[2] In the following Chapter we will see that it is possible to extend this redshift range by allowing the selection of haloes that have already formed stars (*i.e.* not newly virialized).

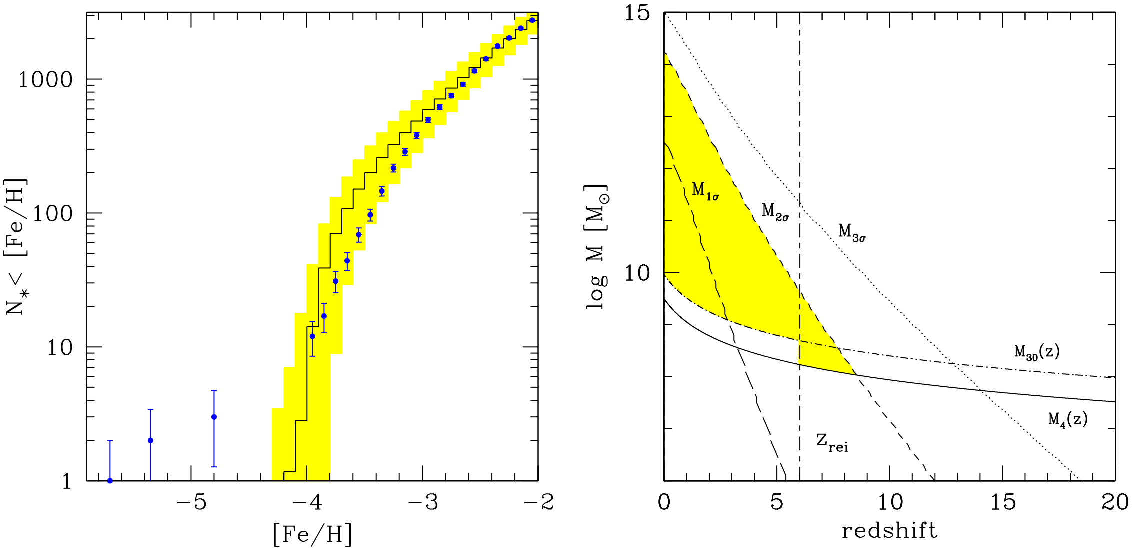

Figure 6.1: *Left panel*: Cumulative number of stars below a given [Fe/H] observed in the Galactic halo (points) and simulated by using the fiducial model $Z_{cr} = 10^{-3.8} Z_{\odot}$, $m_{PopIII} = 200 M_{\odot}$ (histogram). The histogram is the average MDF over 100 realizations of the merger tree re-normalized to the number of observed stars with [Fe/H]≤ -2. The shaded area represents $\pm 1\sigma$ errors Error bars are the Poissoninan errors. *Right*: Evolution of the mass corresponding to 1 (long dashed line), 2 (short dashed line) and $3\sigma(M, z)$ (dotted line) density peaks; the solid line show the evolution of $M_4(z)$, the dotted-dashed line the evolution of $M_{30}(z)$. The selected reionization redshift $z_{rei} = 6$ is also shown in the Figure. The shaded area delimits the region $M_4(z) < M < M_{2\sigma}$ for $z > z_{rei}$, $M_4(z) < M < M_{2\sigma}$ for $z < z_{rei}$.

each single realization, dSph candidates are selected from newly virializing haloes with masses and redshifts corresponding to the shaded area in the right panel of Fig. 6.1, that is $M_4 < M < M_{2\sigma}$ for $z > z_{rei}$ and $M_{30} < M < M_{2\sigma}$ otherwise. Their subsequent evolution is followed in isolation with respect to the forming Galaxy: they neither merge nor accrete material from the GM.

According to the results by Choudhury & Ferrara (2006), we vary the reionization redshift within the range $5.5 < z_{rei} < 10$. The total number of dSph candidates depends on z_{rei} and it is typically larger than the number of observed ones. Therefore, for each z_{rei}, it is necessary to randomly extract a sub-sample in order to match the total number of known MW satellites, ~ 15. The average properties of a dSph galaxy presented in the following Sections refer to the case $z_{rei} = 6$ (see the discussion in Sec. 6.1) and are obtained averaging over the selected satellites from all the 100 realizations of the MW merger tree (about ~ 2000 objects).

6.2.2 Feedback regulated evolution

The life of a dSph is very violent in the first hundred Myr, due to mechanical feedback effects which are more intense in low mass objects. The evolution of the mass of cold gas (eq. 6.6) helps in understanding this behavior. Fig. 6.2 shows the evolution of several properties of an average dSph galaxy ($M = 1.6 \times 10^8 M_\odot$) that virialized at $z_{vir} = 7.2$, with respect to the formation time (age) $T = t - t_{vir}$. Three main evolutionary phases are identified in the Figure, depending on the dominant physical processes.

An increasing fraction of cold gas is collected during Phase I ($T < 40$ Myr) dominated by the infall rate. The mass of the infalling gas rapidly increases during this epoch, reaching a maximum when $T = t_{inf} \sim 25$ Myr. The mass of ejected and returned gas start to contribute to eq. 6.6 only when the most massive SNe of $40 M_\odot$ explode[3], ~ 6 Myr from the formation of the first stellar generation. Thereafter, the mass of ejected and returned gas rapidly grow, due the raising number of SNe and evolving low mass stars. The ISM metallicity and iron abundance evolve accordingly during this phase: they are steadily equal to the values of the infalling gas ($Z_{vir} \sim 10^{-3} Z_\odot$, [Fe/H]$\sim -2.9$) before the first SNe explodes and then rapidly increase.

During Phase II (40 Myr $\lesssim T \lesssim$ 60 Myr) the gain of cold gas by infall is mostly used to form stars and M_g remains constant. Note that the M_*/M curve in Fig. 6.2 represents the *total* stellar mass at time T.

Finally, during Phase III ($T \gtrsim 70$ Myr), the mass of the ejected gas overcomes the infalling gas and M_g starts to decrease. Because of the metal-enhanced wind prescriptions M_Z and M_{Fe} should in principle decrease earlier and faster than M_g. This is the case for M_Z: in Fig. 6.2 the metallicity is a slowly decreasing function both during Phase II and Phase III so that $|\dot{M}_Z| < |\dot{M}_g|$. Conversely, the M_{Fe}/M_g ratio is enhanced during these epochs: the mass of newly synthesized iron released by a SN with a $m = 12 M_\odot$ progenitor is ~ 2 orders of magnitude bigger than for $m = 40 M_\odot$ (Woosley & Weaver, 1995)[4]; for this reason, when lower mass SNe evolve, a larger amount of iron is injected into the ISM and the second right-term in eq. 6.7 can contrast the high ejection rate.

When $T \sim 100$ Myr the mass of gas lost due to winds becomes larger than the remaining gas mass and M_g drops to zero. During this blow-away metals and iron are also ejected out of the galaxy. Moreover, since SN explosions continue at subsequent times, even the infalling gas can rapidly acquire enough energy to escape the galaxy. The infall is first reversed and in few Myr, when the remaining mass of hot gas has blowed-away, definitively stopped. The occurrence of reversal infall in high-redshift dwarf galaxies is confirmed by numerical simulations (Fujita et al.

---

[3] Stars with $40 M_\odot < m < 100 M_\odot$ are predicted to collapse to black holes (Woosley & Weaver, 1995) while massive Pop III stars cannot be produced in dSph galaxies since their birth environment is pre-enriched to $Z_{vir} \sim 10^{-3} Z_\odot > Z_{cr} = 10^{-3.8} Z_\odot$

[4] This result is virtually independent of the initial metallicity of the star. In the same mass range, the total mass of metals produced remains constant.

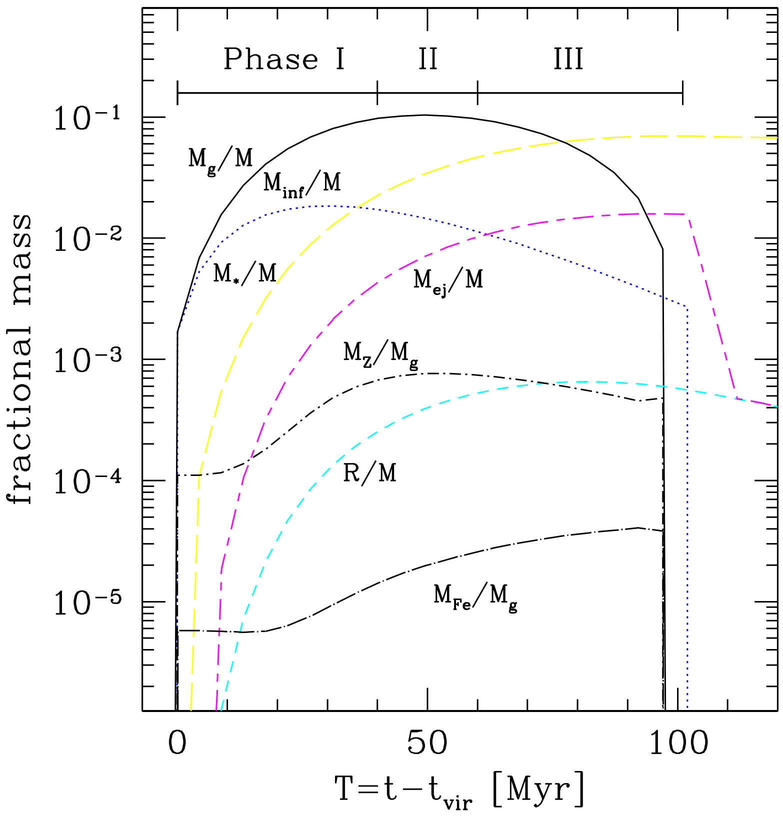

Figure 6.2: Evolution of M_g/M (solid line), M_*/M (long dashed line), M_{inf}/M (dotted line), M_{ej}/M (long-short dashed line), R/M (short dashed line), M_Z/M_g (dotted-short dashed line), M_{Fe}/M_g (dotted-long dashed line) for a typical dSph with total mass $M = 1.6 \times 10^8 M_\odot$, that virialize at redshift $z_{vir} = 7.2$, with respect to its age $T = t - t_{vir}$. The three main evolutionary phases (Phase I $T < 40$ Myr, Phase II 40 Myr $< T <$ 60 Myr, Phase III $T >$ 60 Myr) are also shown.

2004). Eventually at $T \sim 100$Myr our template dSph is a gas free system.

6.2.3 Beyond blow-away

In Fig. 6.3 we show the star formation rate (SFR) of a typical dSph galaxy as a function of its age. The highest peak corresponds to the star formation activity during the first 100 Myr *i.e.* before the blow away. After the blow-away the galaxy remains gas free and star formation is suddenly halted *i.e.* $SFR(T) = 0$. The gas returned by evolved stars represents the only source of fresh gas for the galaxy after the blow away. However, until the latest SN explodes, this low mass of gas is easily ejected outside the galaxy by SN winds (Fig. 6.2); the dSph remains dormant ($SFR = 0$) for the subsequent $\sim$ 150 Myr (this time-lag corresponds to the life time of the lowest $m = 8M_\odot$ SN progenitor formed just before the blow-away). Observationally, mass loss from evolved stars has been invoked by Carignan et al. (1998) in order to explain the detection of neutral hydrogen (HI) associated with the Sculptor dSph galaxy.

After the latest SN explosion, the return rate dR/dt by evolved stars with $m < 8M_\odot$ becomes the only non-zero term of eq. 6.6 and the dSph enters a rejuvenation phase: the recycled gas is collected into the galaxy and star formation starts again.

From the beginning of the rejuvenation phase the subsequent evolution of the galaxy proceeds like in the first 100 Myr of its life. However (Fig. 6.3) SFR is now more than 2 orders of magnitude lower than before the first blow-away, due to the paucity of returned gas. Almost 100 Myr later the galaxy is drained of the whole mass of gas and metals: a new blow-away has occurred and the cycle starts again.

In Fig. 6.3 we note that the repetition of blow-away and rejuvenation phases causes an intermittent SF activity with a typical blow-away separation of ~ 150 Myr. Such burst-like SFH is similar to that inferred from the CMD observed in dSph galaxies such as Carina (Smecker-Hane et al. 1994) although the typical duration of active and quiescent phases is $\sim (1-2)$ Gyr. In agreement with the present work, recent simulations for the collapse of an isolated dwarf galaxy (Stinson et al. 2007), show that feedback effects cause a periodic SF activity, with a typical duration of active and quiescent phases of ~ 300 Myr.

Fig. 6.3 also shows that about 1 Gyr after the formation of the galaxy, this burst-like SFH ends. Because of the gradually smaller mass of gas returned by stars, fewer SNe are produced during this epoch. For this reason, gas ejection is less efficient and can be easily counteracted by the continuous input of returned gas.

Although the SF activity continues until the present-day, the mass of stars formed after the first blow-away ($M_* \sim 2 \times 10^5 M_\odot$) is only 1% of the mass of stars formed before the blow-away ($M_* \sim 2 \times 10^7 M_\odot$). Consistent with this result, the analysis of the dSph CMD diagrams by Dolphin et al. (2005) shows that dSphs typically form most of their stars over 10 Gyr ago.

After the first blow-away subsequent stellar generations formed out of gas recycled by low mass star. The characteristic iron-abundance of this gas is [Fe/H]~ -1.5, as can be inferred using the results of van der Hoek & Groewengen (1997).

6.3 Observable properties

In the following Sections we will compare our numerical results for dSph galaxies with the most relevant observations. Given the amount of available data we take Sculptor as our reference dSph to compare with.

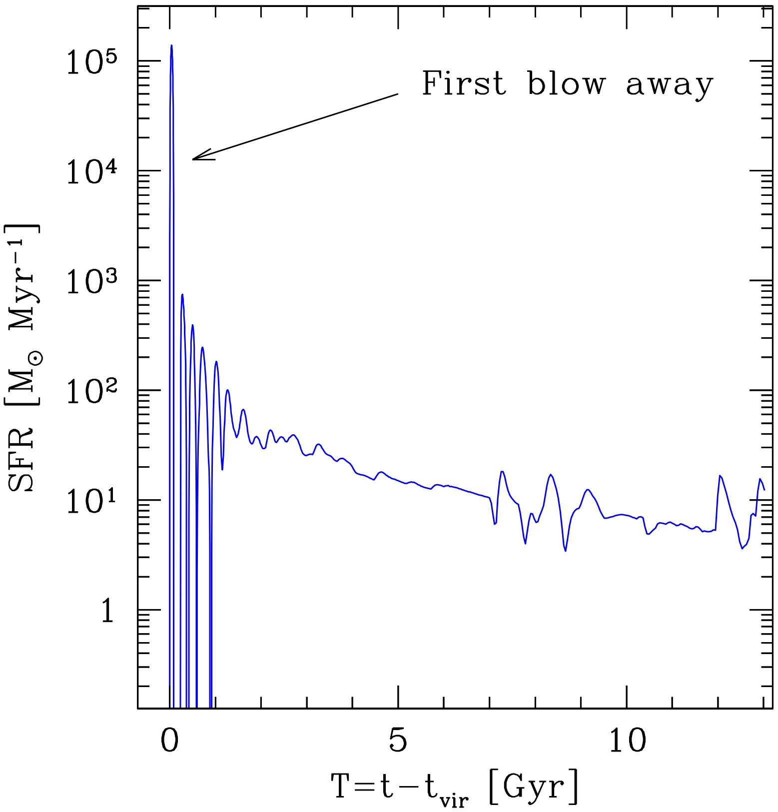

Figure 6.3: SFR of a typical dSph with total mass $M = 1.6 \times 10^8 M_\odot$, which virialize at redshift $z_{vir} = 7.2$, as a function of its age $T = t - t_{vir}$. The arrow shows the occurrence of the first blow-away.

6.3.1 Metallicity Distribution Function

Let's start by analyzing the metallicity distribution function (MDF). In Fig. 6.4 we compare the Sculptor MDF observed by Helmi et al. (2006) with the simulated one, normalized to the total number of observed stars (513). The theoretical MDF is obtained as follows: we adopt a reionization redshift of $z_{rei} = 6$; given this choice, the average number of dSph candidates in each realization is $N_{tot} \sim 200$, among which 10% are assumed to become MW satellites, hence naturally matching the number of observed satellites. A higher reionization redshift of $z_{rei} = 8.5$ would reduce the number of dSph candidates to $N_{tot} \sim 5$, well below the observed value. This allows to put a solid constraint on the reionization redshift of $z_{rei} < 8.5$. As can be inferred from the Figure, the model shows a good agreement with the observed MDF, particularly for [Fe/H]< -1.5. A marginally significant deviation is present at larger [Fe/H] values.

We have already discussed in the previous Section that the bulk of stars ($\sim 99\%$) in a dSph galaxy is formed during the first 100 Myr of its life when [Fe/H]< -1.5. Essentially, stars formed after the first blow away ([Fe/H]> -1.5), are unnoticeable in the normalized MDF. For this reason the physical processes regulating the MDF shape are mostly those responsible for the cold gas mass evolution analyzed in Sec. 6.2.2. We can use the evolution of M_{Fe}/M_g shown in Fig. 6.2 in order to convert time in [Fe/H] variable and identify the three main evolutionary phases into the MDF.

We find that stars with [Fe/H] $\lesssim -2$ formed during the infall-dominated Phase I; the MDF shape at low [Fe/H] values is then essentially regulated by the functional form of the infall rate. Stars with $-2 \lesssim$ [Fe/H] $\lesssim -1.6$ (around the MDF maximum) are formed during Phase II *i.e.* when the mass of cold gas remains approximately constant; the maximum of the MDF is instead fixed by the values of t_{inf} and α. In particular, t_{inf} determines the beginning of Phase II and α its end. Their values ($t_{inf} = t_{ff}(z_{vir})/4$, $\alpha = 10$) have been selected in order to match the Sculptor MDF maximum/shape without altering the global MW properties and Galactic halo MDF (the same parameter are in fact applied to all the virialized MW building blocks). Finally, stars with [Fe/H] $\gtrsim -1.6$, are formed during the feedback-dominated Phase III. Note in particular that the value of the MDF cut-off ([Fe/H]~ -1.5) corresponds to the gas iron-abundance at the blow-away.

At [Fe/H] $\gtrsim -1.5$ our model slightly underpredicts the data as the theoretical MDF drops very steeply. The explanation for such disagreement is likely to reside in our simplified dynamical treatment of mechanical feedback. Interestingly, Mori, Ferrara & Madau (1999), investigated the dynamics of SN-driven bubbles in haloes with $M = 10^8 M_\odot$ at $z = 9$ using 3D simulations. They found that less than 30% of the available SN energy gets converted into kinetic energy of the blown away material, the remainder being radiated away. A large fraction of gas remains bound to the galaxy, but is not available to form stars before it cools and rains back onto the

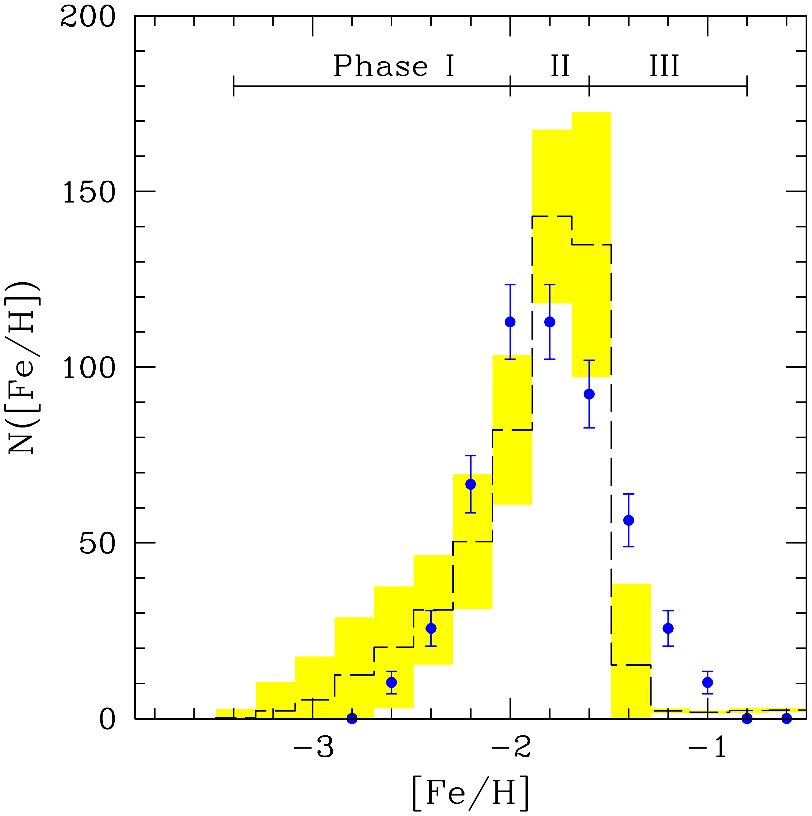

Figure 6.4: Comparison between the Sculptor MDF observed by Helmi et al. (2006), (points) and simulated one obtained by assuming $t_{inf} = t_{ff}/4$, $\alpha = 10$, $z_{rei} = 6$ (histogram). Error bars are the Poissonian errors. The histogram is the averaged dSph MDF over the surviving satellites (~ 20) in all the 100 realization of the merger tree (~ 2000 objects). The shaded area represents the $\pm 1\sigma$ Poissonian error.

galaxy after ~ 200 Myr. Such effect is not included in our modeling. Qualitatively we do expect that such "galactic fountain" would increase the amount of Fe-enriched gas to restart SF after blow-away, and hence the number of [Fe/H]≥ -1.5 stars.

The total number of relics stars shown in the MDF corresponds to a total stellar mass of $M_* = (3 \pm 0.7) \times 10^6 M_\odot$. Using the total (dark+baryonic) dSph mass, derived from our simulations $M = (1.6 \pm 0.3) \times 10^8 M_\odot$ we can compute the mass-to-luminosity ratio

$$\left(\frac{M}{L_*}\right) = \left(\frac{M}{M_*}\right) \times \left(\frac{M_*}{L_*}\right) \sim 150 \quad , \tag{6.8}$$

having assumed $(M_*/L_*) = 3$, in agreement with the results by Ricotti & Gnedin 2005. This result is consistent with the most recent estimate for Sculptor (Battaglia 2007; Battaglia et al. 2008), that gives a very high value $(M/L) = 158 \pm 33$.

6.3.2 Color-Magnitude Diagram

Another comparison with data can be done in terms of color-magnitude diagram (CMD) of the Sculptor stellar population observed by Tolstoy et al. (2004). CMD represents one of the best tools to study the star formation history of a galaxy. Starting from our numerical results for a typical dSph, we have computed the corresponding synthetic CMD using the publicly available IAC-STAR code by Aparicio & Gallart (2004). Given the IMF, the SFR and the ISM metallicity evolution, IAC-STAR allows to calculate several properties of the relic stellar population and, in particular, the stellar magnitudes. We have used the stellar evolution library by Bertelli (1994) and the bolometric correction library by Lejeune et al. (1997). Note that the IAC-STAR input parameters for the ISM metallicity evolution must be $Z^{IAC-STAR} > 0.005 Z_{\odot}$. No binary stars have been included.

We adopt a randomization procedure in order to simulate the observational errors in the synthetic CMD and compare numerical results with data. To this aim, we first derive the normalized error distribution for the magnitude M_I and the color index $V - I$ from the data sample by Tolstoy (private communication). Errors have been randomly assigned at every synthetic star, identified by a (M_I, $V - I$) pair using a Monte Carlo method and randomly added or subtracted. Note that more accurate (and complicated) randomization procedures exist (see for example Aparicio & Gallart 2004); however, we consider the simple approach adopted here adequate for our present purposes. In Fig. 6.5 we compare the synthetic and observed CMDs. Data by Tolstoy et al. (~ 10300 stars into the relevant M_I, $V - I$ range) have been normalized to the total number of synthetic stars derived by IAC-STAR (~ 2300). In order to do so stars have been randomly selected from the data sample.

The match between theoretical and experimental points is quite good. We note however that the number of red giant branch (RGB) stars in the synthetic CMD is lower than the observed one. This discrepancy can be explained with the contamination of the data sample by Galactic foreground stars (see Tolstoy et al. 2004). The synthetic CMD reproduces reasonably well the blue/red horizontal branch stars (BHB/RHB stars) *i.e.* stars residing in the CMD branch ($0 < M_I < 1$, $0 < (V - I) < 1$). A well populated HB in the CMD diagram might be interpreted as an indication of an old stellar population (age > 10 Gyr). The interpretation of the blue and red HB, on the contrary, is quite controversial: due to the age-metallicity degeneracy of the CMD stellar colors become bluer when stars are younger and/or poorer in metallicity. For this reason the position of a star in the CMD cannot be unequivocally interpreted. In our model the majority of the stars are formed during the first 100 Myr of the dSph life; this means that all the stars have basically the same age $\gtrsim 13$ Gyr; so the HB morphology, in our model, reflects the metallicity gradient of the stellar populations: BHB stars belong to metal-poor stars formed during the Phase I (see Fig. 6.2) while RHB stars to the more metal-rich stars formed

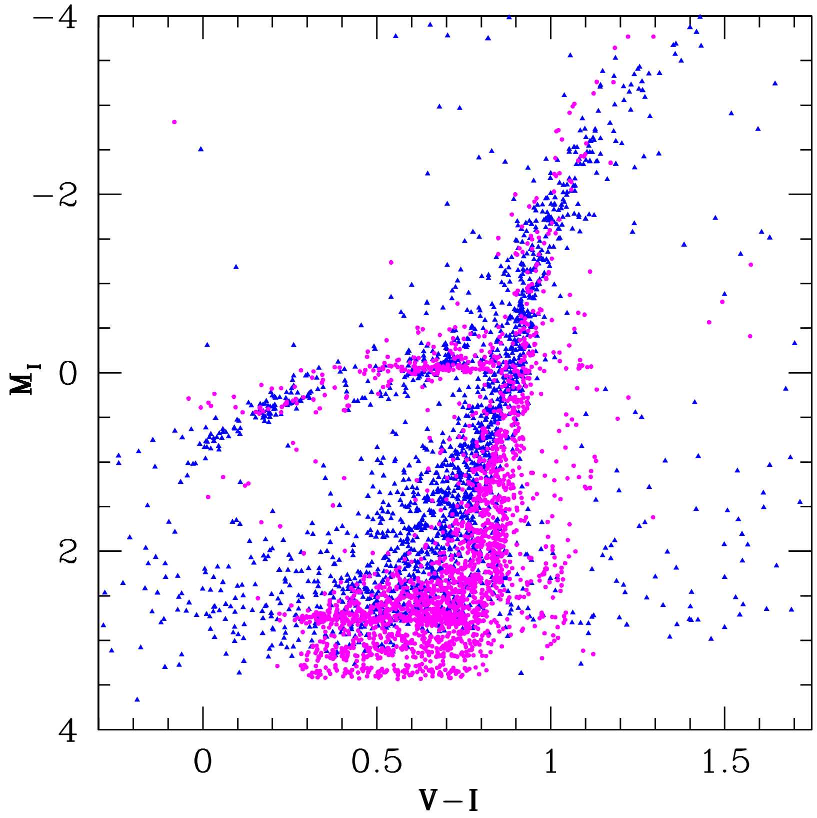

Figure 6.5: Comparison between the CMD of the Sculptor stellar population observed by Tolstoy et al. (2004) (triangles) and the synthetic CMD (open points) derived for a typical dSph galaxy with total mass $M = 1.6 \times 10^8 M_\odot$ which virialize at redshift $z_{vir} = 7.2$.

during the Phase II.

6.3.3 Keys abundance ratios

A method commonly used to break the age-metallicity degeneracy and derive accurate SFH from the CMD diagrams, is the analysis of the stellar elemental abundances. In most of the observed dSph galaxies the abundance ratio of α elements (O, Mg, Si, Ca) relative to iron ([α/Fe]) shows a strong decrease when [Fe/H]> -2 (Venn et al. 2004; Tolstoy, Hill, Tosi 2009). Since α-elements are primarily generated by SN II while a substantial fraction of iron-peak elements (Fe, Ni, Co) are produced by type Ia SNe (SNe Ia), the decline of [α/Fe] is usually interpreted as a contribution by SNe Ia. Using this argument and the assumption that the lifetime of SNe Ia is around 1.5 Gyr, Ikuta & Arimoto (2002) inferred an age spread of 1-2 Gyr in the dominant stellar population of Draco, Sextans and Ursa Minor dSphs. However, the issue of the lifetime of SNe Ia remains quite debated and uncertain, with timescales as short as 40 Myr having been suggested (see Ricotti & Gnedin 2005 for a thorough discussion) under starburst formation conditions.

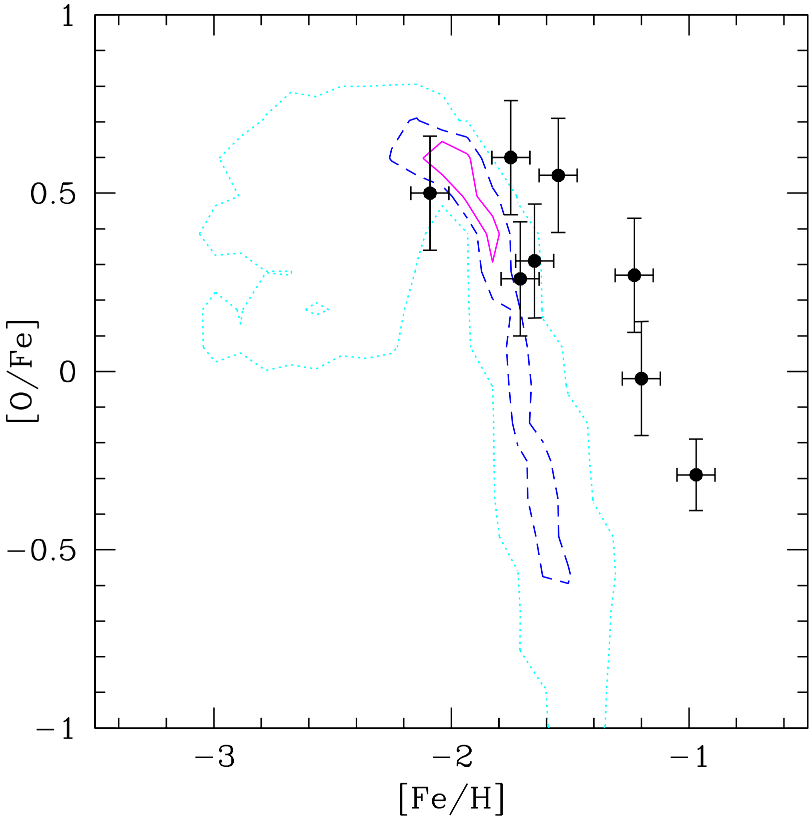

Figure 6.6: Oxygen-to-iron stellar abundance with respect to [Fe/H] for the Sculptor dSph. Points refer to 8 Sculptor stars observed by Gaisler et al. (2005) and Shetrone et al. (2003); contours represent the probability, respectively equal to 0.6 and 0.8 and 0.99, to find a star into the [O/H]-[Fe/H] plane.

In Fig. 6.6 we compare the oxygen-to-iron stellar abundance with respect to [Fe/H] for 8 stars observed in Sculptor by Gaisler et al. (2005) and Shetrone et al. (2003), with the results of our model. In spite of the poor statistics the data show a clear indication of the [O/Fe] decrement for [Fe/H]> -1.8; in particular, subsolar values are observed. Even if SNe Ia are not included in our model, a drop in the [O/Fe] occurs as a result of having released the IRA approximation (see also Fenner et al. 2006) and of differential winds. However, subsolar [O/Fe] values can only be accounted for by differential winds. This is because when [O/Fe] reaches the maximum value[5], the "effective oxygen yield" $(dY_O/dt - Z_O^w dM_{ej}/dt)$ is strongly reduced with respect to iron due the effect of differential winds, which, as can be

---

[5] The relative production rate of oxygen with respect to iron is larger in low-mass SNe II.

deduced from eq. 6.7, have a larger impact on more abundant elements ($Z_i^w = \alpha Z_i^{ISM}$). This causes a pronounced and rapid decrease of [O/Fe] to subsolar values. We note that model results tend to underpredict the observed stellar abundances: essentially, differential winds are too efficient. We recall, however, that the value $\alpha = 10$ have been selected in order to match the Sculptor MDF. The problem of the lack of [Fe/H]> -1.5 stars noted in Sec. 6.1, is evident also here. A more sophisticated treatment of differential winds and/or the inclusion of the missing physical effects discussed in Sec. 6.1, should presumably remove such discrepancies. Noticeably the result of Fig. 6.6 is fully consistent with the analysis by Fenner et al. (2006), who studied the Sculptor chemical evolution including differential winds. In conclusion we find that the trend of [α/Fe] does not require a prolonged star formation phase (> 1 Gyr) but can be satisfactorily explained even if 99% of the stars formed during the first 100 Myr of the dSph lifetime.

Additional constraints on the SFH may also come from the analysis of the abundances of s-elements associated with the slow neutron-capture process. These are produced by low-mass stars during Asymptotic Giant Branch (AGB) phases. From an analysis of [Ba/Y] Fenner et al. (2006) concluded that most of the stars must be formed over an interval of at least several Gyr to allow time for metal-poor AGB stars to enrich the ISM up to the observed values. Our model does not make specific prediction on s-elements; it is likely however that since the bulk of stars is predicted to formed on a time-scale of ~ 100 Myr there would not be enough time for the ISM to be enriched with the products of AGB stars. Nevertheless this may not be the only scenario to explain s-elements abundances. For example binary systems in which the lower mass, long-living star, accretes s-enhanced gas directly from the companion rather than from the ISM can equally explain the observed high s-elements abundances. Internal production during the dredge-up phase can represent yet another possibility. These alternative scenarios are supported by the observed stellar [s/Fe] ratio with respect to [Fe/H]. The data (Venn et al. 2004) show that the [s/Fe] values do not increase at higher [Fe/H], as expected if the ISM is gradually enriched by the contribution of lower mass stars. Moreover, a large [s/Fe] spread is observed for any [Fe/H] which is expected if the efficiencies of accretion, dredge-up and s-element production are functions of stellar mass.

6.3.4 Dark Matter content

DSph galaxies represent the most dark matter-dominated systems known in the Universe. It is then very interesting to determine their dark matter mass. Observationally, the mass content of dSph galaxies is derived by measuring the velocity dispersion profile of their stellar populations and comparing it with the predictions from different kinematic models. The latter step strongly depends on the adopted stellar kinematics (in particular the assumed velocity anisotropy radial profile), on the dark matter mass distribution, and on the nature of the dark matter itself.

Recently, Battaglia (2007), Battaglia et al. (2008) have derived the velocity dispersion profile of Sculptor measuring the velocities of ~ 470 RGB stars. They model Sculptor as a two component system with a metal poor and a metal rich stellar population that show different kinematics. They use these two components as distinct tracers of the same potential and find that the best model is a cored profile with $r_c = 0.5$kpc and $M(< r_{last})^6 = (3.4 \pm 0.7) \times 10^8 M_\odot$ which gives an excellent representation of the data assuming an increasing radial anisotropy. Interestingly, the values of $M(< r_{last})$ obtained assuming a NFW model for the dark matter distribution or a constant radial anisotropy are $M(< r_{last}) = (2.4^{+1.1}_{-0.7}) \times 10^8 M_\odot$ and $M(< r_{last}) = (3.3 \pm 0.8) \times 10^8 M_\odot$, respectively, consistent with the above result within 1σ. The average mass of dSph galaxies that we infer from our simulations is consistent with these estimate $M = (1.6 \pm 0.8) \times 10^8 M_\odot$.

As the last measured points in Battaglia (2007), Battaglia et al. (2008) typically reach 1-2 kpc, one could suspect that additional dark matter could be located outside this radius, thus turning their determination into a lower mass limit. However, for the mean mass value and formation redshift that we have obtained $M \approx 10^8 M_\odot, z_{vir} \approx 7$, the virial radius of such a halo is 1 kpc. Thus, the agreement (at $1 - 2\sigma$ level) between our prediction and the actual mass determinations might not be coincidental, but reflects the fact that in these small objects star formation has propagated up to the most remote galactocentric regions. This prediction could be eventually checked by deeper observations and/or other techniques.

Finally, by assuming a NFW density profile, $z_{vir} = 0$ and a concentration parameter $c = 35$ (Battaglia 2007), we calculated the dark matter mass enclosed within a radius of 0.6 kpc $M_{0.6} = (2.3) \times 10^7 M_\odot$. This finding agrees with the results by Mateo et al. (1998), Gilmore et al. (2007) and Walker et al. (2007), who suggest that dSph galaxies might have a common mass scale $M_{0.6} = (2 - 7) \times 10^7 M_\odot$.

6.3.5 Gas footprints of feedback

A final comparison with data can be done in terms of the observed gas properties. In the previous Sections we have shown that metal-enhanced winds driven by SN explosions play a fundamental role in determining the evolutionary times scales and properties of a dSph galaxy. Based on observations obtained with the Chandra X-Ray Observatory, Martin, Kobulnicky & Heckman (2002) provide the first direct evidence for metal-enhanced winds from dwarf starburst galaxies. They have observed the hot X-ray-emitting gas around the nearby dwarf galaxy NGC 1569 which entered in a starburst phase (10-20) Myr ago. The X-ray spectrum they find presents strong emission lines from α-process elements, that require the wind metallicity to be $Z^w > 0.25 Z_\odot$ *i.e.* larger than $Z^{ISM} = 0.2 Z_\odot$, supporting our assumption of metal enhanced winds $Z^w = 10 Z^{ISM}$. In particular, their best fit models predict the ratio of α-elements to Fe to be 2-4 times higher than the solar value; it is then likely that

---

[6] $M(< r_{last})$ is the mass enclosed within the last measured point.

the ISM is preferentially depleted in α-elements consistent with the findings shown in Fig. 6.6. We stress that these observations confirm the idea that mechanical feedback processes start to play a significant role in the dSph evolution on a very short time-scale (10-20 Myr after the beginning of the starburst phase).

Alternatively, the efficiency of mechanical feedback processes can be tested using observations of neutral hydrogen (HI). The Local Group dSph galaxies are all relatively HI poor (Mateo 1998) suggesting that little gas has remained after the main SF phase. Within the known dSph galaxies, Sculptor is one of the few with detectable HI emission. Using radio observation, Carignan et al. (1998) derived a lower limit for the HI mass of $M_{HI} > 3 \times 10^4 M_\odot$. Our simulation predicts an average mass of gas $M_g = (2.68 \pm 0.97) \times 10^4 M_\odot$, in very good agreement with the observed value if indeed this gas is in neutral form. According to our model, the HI mass detected in Sculptor can be associated to gas returned by evolved stars, an explanation also offered by Carignan et al. (1998).

6.4 Summary and discussion

We have proposed a global scenario for the formation and evolution of classical ($L_{tot} > 10^5 L_\odot$) dSph galaxies in their cosmological context by using an improved version of our semi-analytical code GAMETE. This approach allows us to follow self-consistently the dSph evolution and the MW formation and match, simultaneously, most of their observed properties. In this theoretical framework dSphs form within the Galactic environment, whose metallicity evolution depends on the history of star formation and mechanical feedback along the build-up of the Galaxy. The star formation and mechanical feedback efficiencies of dSphs are assumed to be the same as for all the Galactic building blocks and they are calibrated to reproduce the observed global properties of the MW.

DSph candidates are selected among the MW progenitors following a dynamical and a reionization criteria; we choose haloes with masses (i) $M_4 < M < M_{2\sigma}$ if $z > z_{rei}$, (ii) $M_{30} < M < M_{2\sigma}$ if $z < z_{rei}$ *i.e.* we assumed the formation of galaxies with circular velocity $v_c < 30$ km/s to be suppressed after reionization, where $5.5 < z_{rei} < 10$ (Choudhury & Ferrara 2006). As the number of dSph candidates found varies with z_{rei}, we determine the fraction that will become MW satellites requiring that their number matches the observed one (~ 15). Once formed, dSphs are assumed to evolve in isolation with respect to the merging/accreting Galaxy. In this work we present the results obtained assuming $z_{rei} = 6$. This value provides a good agreement between the Sculptor MDF and the simulated one and gives a total number of dSph candidates of $N_{tot} \sim 200$; hence, we suppose that $\sim 10\%$ of them become MW satellites.

The results of our model, supported by the comparison with observational data and previous theoretical studies, allow to sketch a possible evolutionary scenario for dSphs. In our picture dSph galaxies are associated with Galactic progenitors corresponding to low-sigma density fluctuations ($M_4 < M < M_{2\sigma}$), that virialize from the MW environment before the end of reionization, typically when $z = 7.2 \pm 0.7$. Their total (dark+baryonic) mass results to be $M = (1.6 \pm 0.7) \times 10^8 M_\odot$.

At the virialization epoch the dSph birth environment is naturally pre-enriched due to previous SN explosions up to $[\mathrm{Fe/H}]_{GM} \gtrsim -3$, a value fully consistent with that inferred from observations by Helmi et al. (2006). The subsequent dSph evolution is strongly regulated by mechanical feedback effects, more intense in low mass objects (MacLow & Ferrara 1999). We take winds driven by SN explosions to be metal enhanced ($Z^w = 10Z^{ISM}$) as also confirmed by numerical simulations (Fujita et al. 2004) and by the X-ray observations of the starburst galaxy NGC1569 (Martin et al. 2002). Typically, ~ 100 Myr after the virialization epoch a complete blow-away of the gas caused by mechanical feedback is predicted. The 99% of the present-day stellar mass, $M_* = (3 \pm 0.7) \times 10^6 M_\odot$, is expected to form during the first 100 Myr. The stellar content of dSphs is then dominated by an ancient stellar population (> 13 Gyr old), consistent with the analysis of the dSph CMD diagrams by Dolphin et al. (2005).

After the blow-away the galaxy remains gas-free and SF is stopped. Fresh gas returned by evolved stars allows to restart the SF ~ 150 Myr after the blow-away. The SFR, however, is drastically reduced due to the paucity of the returned gas. Mass loss from evolved stars has been also invoked by Carignan et al. (1998) to explain the detection of HI in the Sculptor dSph. About ~ 100 Myr later, a second blow-away occurs and the cycle starts again. Such intermittent SF activity is similar to those observed in Carina by Smecker-Hane et al. (1994) and to the one derived by Stinson et al. (2007) using numerical simulations. Roughly 1 Gyr after the virialization this burst-like SFH ends while the SF activity proceeds until the present-day with a rapidly decreasing rate. At $z = 0$ the dSph gas content is $M_g = (2.68 \pm 0.97) \times 10^4 M_\odot$.

Our model allows to match several observed properties of Sculptor:

- The Metallicity Distribution Function (Helmi et al. 2006). The pre-enrichment of the dSph birth environment accounts for the lack of observed stars with $[\mathrm{Fe/H}] < -3$, a striking and common feature of the four dSph galaxies observed by Helmi et al. (2006).

- The stellar Color Magnitude Diagram (Tolstoy et al. 2003) and the decrement of the stellar [O/Fe] abundance ratio for $[\mathrm{Fe/H}] > -1.5$ (Gaisler et al. 2005, Shetrone et al. 2003). The agreement found between models and observations support the SFH we have predicted.

- The DM content $M = (3.4 \pm 0.7) \times 10^8 M_\odot$ and the high mass-to-light ratio $(M/L) = 158 \pm 33$ recently derived by Battaglia (2007), Battaglia et al. (2008);

we find $(M/L) \sim 150$ using the predicted dark matter to stellar mass ratio and assuming $(M/L)_* = 3$.

- The HI gas mass content. The value derived by radio observations ($M_{HI} > 3 \times 10^4 M_\odot$, Carignan et al. 1998) is in agreement with our findings.

Interestingly, the model can also be used to put an upper limit on epoch of the MW environment reionization, $z_{rei} < 8.5$. The total number of selected dSph candidates in fact, is reduced below the observed one ($N_{tot} \sim 5$) if $z_{rei} = 8.5$. In addition, the imprint of reionization lies in the suppression of dSphs formation below the reionization redshift, $z_{rei} = 6$. This result is consistent with the presence of an ancient stellar population in *all* the observed dSph galaxies (Grebel & Gallagher 2004).

Despite the success of the model in producing a coherent physical scenario for the formation of dSphs in their cosmological context and matching several of the Sculptor and MW properties, several aspects deserve a closer inspection. Although Sculptor represents the best dSph to compare with because of its average properties and the large amount of available data, examples of deviations are already known. In particular we recall that the SFHs differ considerably among dSph galaxies (Dolphin et al. 2005, Grebel & Gallagher 2004). The Fornax CMD diagram, for example, indicates a massive presence of younger stars than in other dSphs (Dolphin et al. 2005; Stetson et al. 1998; Buonanno et al. 1999); the peculiarity of this object is also evident in the observed MDF, which is a monotonically increasing function up to [Fe/H]~ -1 (Pont et al. 2004; Helmi et al. 2006; Battaglia et al. 2006). The dSph properties inferred in our model, including the SFH and the MDF, are instead "Universal". This is a consequence of the selection criteria, that gives a Universal dSph host halo mass, and of the assumed cosmological gas fraction in all virializing haloes. Since $M_4(z) < M_{2\sigma}$ only for $z < 9$ (see Fig. 6.1, right panel) and the typical mass of *newly* virializing halo is $\sim M_4(z) < M_{30}$, dSphs are forced to form in the redshift range $6 < z_{rei} < 9$. Due to the small variation of $M_4(z)$ in such a range, the dSph dark matter content is very similar in all objects and equal to $\sim 10^8 M_\odot$.

Clearly, random episodes of mass accretion and/or merging with other haloes would allow to produce a spread in both the total mass content and the SFH of dSphs. In the next Chapter we will see how it is possible to extend the mass range of the dSph hosting haloes by including in the selection criteria those objects that have already formed stars. A spread in the dSph properties will be naturally obtained as a result of the different merging/accretion histories and final redshift of assembling.

Another physical mechanism might be invoked in order to explain the paucity of remnant gas in dSphs, and perhaps as a mechanism of star formation suppression: tidal stripping by the gravitational field of the Galaxy (Ibata et al. 2001; Mayer et al. 2002, 2006). Models not accounting for mechanical feedback effects (Marcolini et al. 2008; Revaz et al. 2009; Sawala et al. 2009) cannot reproduce the paucity of gas in dSphs, and invoke this mechanism in order to reconcile their results with the observations. In our model we see no need to resort to such effect as the large majority of the gas is expelled by SN feedback within the first 100 Myr of dSph evolution (we recall that the amount of newly born stars after that time is only $\approx 1\%$ of the final stellar mass). Hence, by the time dSphs find themselves embedded in the MW gravitational potential, there is little gas left to be stripped.

Finally we have to note that our model cannot account for the existence of the newly discovered ultra faint dSphs, all the selected candidates being Sculptor-like dSphs with a total luminosity $L_{tot} > 10^5 L_{\odot}$.

Chapter 7

Ultra faint dwarfs

Ultra faint dwarf spheroidal galaxies (UFs) represents the *least* metal-rich, the *least* luminous, and probably the *least* massive stellar systems ever known ($\langle[\mathrm{Fe/H}]\rangle \lesssim -2.2$, $L_{tot} < 10^{3-5}L_{\odot}$, $M \approx 10^{7-8}M_{\odot}$). Such extreme features make these galaxies the living fossils best suitable for the investigation of the early cosmic star formation, initially developing in H_2 cooling minihaloes (Sec. 2.2.1). In addition to these challenging properties the nature of UFs is made more intriguing by the observed Fe-Luminosity relation and metallicity distribution function. Indeed while the Fe-Luminosity relation constitutes an extension toward lower metallicities of that of classical dSphs, suggesting a common origin of these galaxies, the UFs MDF reveals the existence of $[\mathrm{Fe/H}] < -3$ stars which are *missing* in classical dSphs.

During the past year several authors explored the origin and properties of UFs, mainly focusing on the implications for the missing satellites problem (Madau et al. 2008; Bovill & Ricotti 2009; Muñoz et al. 2009; Koposov et al. 2009; Macció et al. 2009; Kravtsov et al. 2009; D'Onghia et al. 2009). According with the results of the cosmological simulations by both Bovill & Ricotti (2009) and Muñoz et al. (2009), the existence of $L_{tot} < 10^5 L_{\odot}$ dSphs is a strong evidence for H_2 cooling in minihaloes. The first study, which accounts for the boost of H_2 production driven by the ionizing radiation (positive feedback), and successfully reproduces some of the observed properties of UFs and classical dSphs, predicts that the SF in minihaloes can proceed until the end of reionization, fixed at $z_{rei} = 8.2$. The second authors instead, found that in order to match the observed luminosity function of the MW satellites, the minihaloes SF has to be suppressed as soon as $z = 23$, while $z_{rei} = 11$.

Different scenarios for the origin of UFs has been proposed by other studies. By combining N-body simulations with semi-analytical models, Macciò et al. (2009) found that the luminosity function of the MW satellites can be match without invoking minihaloes, its functional form being shaped by tidal destruction, suppression of gas infall due to ionizing background, and stellar feedback. Numerical simulations by Mayer et al. (2007), found that the combination of the high mass-to-light ratio of UFs along with their exceptional proximity to the Milky Way, implies a formation mode completely driven by tidal shocks and ram pressure. Finally D'Onghia et al. (2009), have recently proposed a "resonant stripping" scenario for the formation of UFs, which successfully account for some of their morphological and kinematic properties. Unfortunately, none of these studies analyzed either the observed Fe-Luminosity relation of UFs or the observed MDF; by the way the latter has never been investigated so far.

In this Chapter we will explore the origin and evolution of UFs by implementing the physics of $T_{vir} < 10^4$ K minihaloes in our code GAMETE, which self-consistently describes the gradual build-up of the MW and its dwarf satellite galaxies.

7.1 Including minihaloes

The inclusion of minihaloes requires to take into account the effects of radiative feedback processes which, as pointed out in the Introduction, are crucial in order to determine both the minimum mass and the efficiency of star formation.

We know that two distinct radiative feedback processes control the redshift evolution of the minimum mass of star-forming haloes, M_{sf}. The first one has to do with the increase of the Jeans mass in progressively ionized cosmic regions, quenching the infall of gas in haloes below a given circular velocity, v_c^*. As usual we adopt the typical value $v_c^* = 30$ kms^{-1} after the end of reionization $z_{rei} = 6$. Before reionization a second type of feedback, related to the photodissociation of H_2 molecules by the Lyman-Werner (LW) background photons, becomes important and suppress the SF in minihaloes to an extent which depends on the intensity of the UV background (Haiman, Rees & Loeb 1996; Ciardi, Ferrara & Abel 2000; Kitayama et al. 2000; Machacek, Bryan & Abel 2001). According to Dijkstra et al. (2004) at $z \approx 10$ objects with $v_c \geq 10$ km s^{-1} ($T_{vir} \approx 2000$K) can self-shield and collapse; therefore we use this value as the minimum absolute threshold for star formation. During reionization ($6 < z < 9$) the interplay between these two feedback types is quite complicated and no consensus is found on the evolution of $M_{sf}(z)$. Instead of modeling in detail the build-up of LW and ionizing UV backgrounds, we interpolate between the low- and high-redshift behaviors and use an heuristic form for $M_{sf}(z)$ which leads to the suppression of SF in gradually more massive objects (Fig. 7.1). Such parametrization of $M_{sf}(z)$ allows to *correctly reproduce* the observed iron-luminosity relation of dSphs (Fig. 7.2)[1].

As usual dSph candidates are selected among the star forming haloes of the merger tree which are likely to become satellites *i.e.* those corresponding to density fluctuations $< 2\sigma$. In addition we now enable the selection of haloes which have already formed stars, hence broadly extending the DM mass range of dSph candidates (Fig. 7.1). This implies that the same haloes can be selected several times at

---

[1] The total luminosity value is derived from the stellar mass content as $L = M_* \times (M/L)_*$ by assuming $(M/L)_* = 1$.

different redshifts; in order to limit multiple selections, we require the stellar mass of dSph candidates to be $M_* < 0.1(\Omega_b/\Omega_m)M$. Through this method we build a statistically significant dSph sample; however, it prevents us from making specific predictions on the actual number of dSph satellites. Once selected, the isolated evolution (no further merging or accretion events) of virtual haloes with the same initial conditions (dark matter/gas/stellar content, metallicity) is followed.

In Fig. 7.1 the halo masses of selected dSph candidates is shown along with their initial baryonic fraction, f_b, with respect to the cosmic value $f_c = \Omega_b/\Omega_m = 0.156$. We classify dSphs according to their initial baryonic content as gas-rich, $f_b/f_c > 0.5$, intermediate, $0.1 < f_b/f_c < 0.5$, and gas-poor, $f_b/f_c < 0.1$, systems.

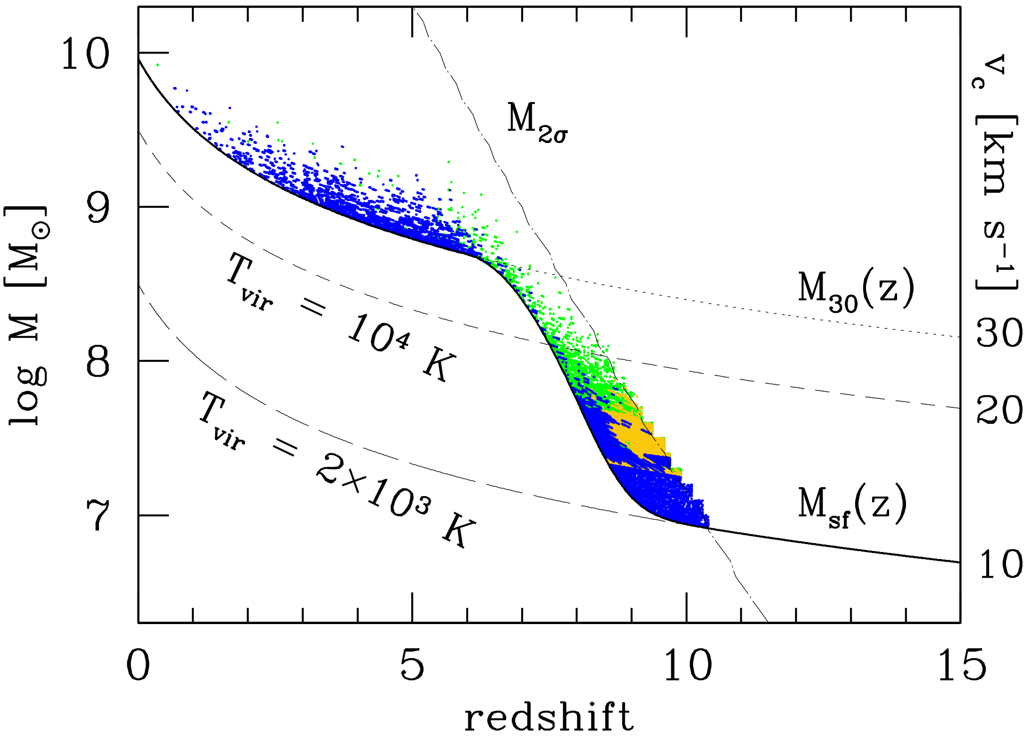

Figure 7.1: Dark matter halo mass and circular velocity of selected dSph candidates as a function of their formation redshift z (points) for 10 realizations of the hierarchical merger tree. Different colors show the baryonic fraction f_b at the formation epoch with respect to the cosmic value $f_c = 0.156$: $f_b/f_c > 0.5$ (blue), $0.1 < f_b/f_c < 0.5$ (green), $f_b/f_c < 0.1$ (yellow). The lines show the evolution of $M_{sf}(z)$ (solid), $M_{30}(z)$ (dotted), the halo mass corresponding to 2σ peaks (dotted-long dashed), $T_{vir} = 10^4$K (short dashed line) and $T_{vir} = 2 \times 10^3$K (long dashed line).

The second important improvement of the model, related with the inclusion of minihaloes, is to assume a mass-dependent SF efficiency. In minihaloes, in fact, the ineffective cooling by H_2 molecules limits the amount of gas than can be transformed into stars. Several authors (Madau, Ferrara & Rees 2001; Ricotti & Gnedin

2005; Okamoto, Gao & Theuns 2008) agree that in these systems the SF efficiency decreases $\propto T_{vir}^3$. A suitable form is then

$$\epsilon \propto \frac{\epsilon_*}{[1 + (\frac{T_{vir}}{2\times 10^4 \mathrm{K}})^{-3}]}, \tag{7.1}$$

where ϵ_* is the local star formation efficiency defined in Sec. 2.2.2. For all the free parameters of the model we use the values found in the previous Chapter and check that both the global properties of the MW and the Galactic halo MDF are well reproduced.

7.2 The Fe-Luminosity relation

We can start by comparing the observed metallicity-luminosity relation with our predictions; the results are reported in Fig. 7.2. The overall agreement is satisfactory, and the increasing trend of metallicity with luminosity well reproduced. The faint end of the relation, $L < 10^6 L_\odot$, is predominantly populated by minihaloes; above that luminosity H-cooling haloes dominate. The low-L segregation of minihaloes naturally arises from their low masses and it is further extended toward very faint luminosities, $L < 10^4 L_\odot$, by the reduced SF efficiency and, most importantly, by their low initial baryonic fraction $f_b/f_c < 0.1$. Being UFs defined as systems with $L < 10^5 L_\odot$, we conclude that all UFs are minihaloes but there are minihaloes that are not UFs.

We have just pointed out that the initial baryonic fraction is a key factor in dSph galaxy evolution. What sets such initial value? Gas-rich systems are distributed through the entire mass ($M = 10^{7-10} M_\odot$) and formation redshift ($z = 2-10$) ranges of selected dSph candidates (Fig. 7.1). These dSphs are the present-day counterpart of predominantly newly virialized objects accreting gas from the GM. Intermediate systems ($0.1 < f_b/f_c < 0.5$) originate from mixed merging of star-forming and starless progenitors; they are typically more massive than gas-rich haloes and form at lower redshifts. Their smaller baryonic content is the result of shock-heating of the infalling gas during major merging events (Cox et al. 2004) which stops accretion. Finally, gas-poor systems formed by merging of *recently* virialized, $M > M_{sf}$ progenitors. Since most of the diffuse gas is still accreting, shock heating quenches the infall early on. Note that a low baryonic content might also result from shock-stripping of the gas due to winds outflowing from nearby galaxies (Scannapieco, Ferrara & Broadhurst 2000).

The faintest UFs are found to be gas-poor systems; this fact has two important implications. First, being the SN rate depressed in these systems by the scarce availability of gas, mechanical feedback has negligible effects, and they evolve as a closed-box. As essentially all metals are retained they have a relatively high Fe-abundance which is seen as an almost inverted Fe-L relation below $L = 10^{4.5} L_\odot$.

Second UFs have extremely large $M/L > 100$ ratios, and the faintest ones among them reach such extreme values as $M/L \approx 10^4$.

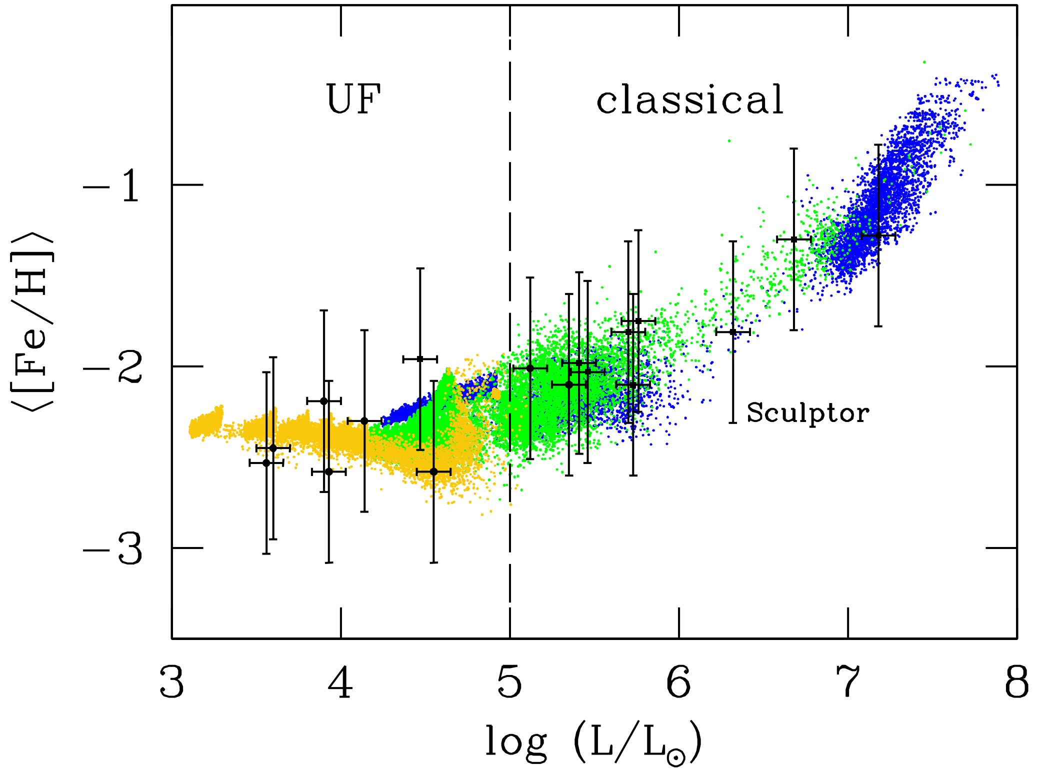

Figure 7.2: Total luminosity of selected dSph candidates as a function of their average iron abundance (points) for 10 realizations of the hierarchical merger tree. As in Fig. 7.1 different colors show the baryonic fraction at the formation epoch with respect to the cosmic value. The points with error bars are observational data from Kirby et al. 2008.

7.3 Metallicity Distribution Functions

To get more insight in the nature of UFs it is instructive to analyze their stellar metallicity distribution function.

7.3.1 Classical vs ultra faint dwarfs

In Fig. 7.3 (left panel) we show the MDF averaged over all UF candidates in 10 realizations of the merger tree, along with the available data (Kirby et al. 2008). The shape of the distribution is relatively broad extending from [Fe/H]≈ -4 to ≈ -1, in good agreement with observations. This is noticeably different from the Sculptor MDF shown in the right panel of the same Figure. SN feedback in Sculptor is much stronger than in UFs, as explained above; SF activity is then terminated shortly after 100 Myr (see Fig. 6.3) whereas UFs can continue to quietly form stars up to 1 Gyr from their birth. These physical differences are reflected in the wider MDF of ultra faint dSphs. In our model Sculptor-like dSphs[2] are associated with gas-rich, H-cooling haloes, with $M \approx 10^8 M_\odot$, virializing at $z \approx 7.5$, in agreement with our findings in Salvadori, Ferrara & Schneider (2008), exposed in the previous Chapter. However, in contrast with that study we now predict a small tail of $[\mathrm{Fe/H}] < -3$ stars. These are relics of the rare SF episodes occurred in some progenitor minihaloes (which were not considered previously) at $z > 7.5$. Therefore, such a small number of very iron-poor stars in classical dSphs are expected to be characterized by the same abundance pattern of $[\mathrm{Fe/H}] < -3$ stars in UFs. The rest of the MDF, on the contrary, is built after the stellar population bulk assembling at lower redshifts. A striking difference between the two distributions in Fig. 7.3 is the larger fraction ($\approx 25\%$) of extremely metal poor stars ($[\mathrm{Fe/H}] < -3$) present in the MDF of ultra faint dSphs. The interpretation of this result is clear: as UFs form earlier the metallicity of the GM gas out of which they virialize is correspondingly lower but still high enough that low-mass stars can be produced according to the critical metallicity criterion. In principle, then, UFs are potentially powerful benchmarks to validate this criterion, which would exclude the presence of stars of *total* metallicity below Z_{cr}, here fixed at $Z_{cr} = 10^{-3.8} Z_\odot$.

7.3.2 The Ultra Faint candidates

The observed MDF for the single ultra faint dSphs (Kirby, private communication) are compared with the simulated ones in Fig. 7.4. The latter have been obtained by averaging over UF candidates with L_{tot} equal to those of the observed UFs (see Fig.1.8), in 10 realizations of the merger tree. The panels, from top to bottom, show the MDF of UFs with increasing luminosity. We note that the more luminous is a UF, the higher is the [Fe/H] value of the MDF maximum, reflecting the trend of the Fe-Luminosity relation. The agreement between model results and observations is very good for the most luminous UFs. This is particularly evident for the case of Canes Venatici I (CVnI), which counts the highest number of observed stars. At the lower luminosity however, the MDF maximum predicted by the model is shifted toward lower [Fe/H] values than those observed. Although this effect could be partially alleviated by averaging over a larger number of hierarchical merger histories, a more rapid metal enrichment seems to be required in order to match the data. This could be either driven by a lower value of M_{sf} or by the clustering of the metal sources at the high redshifts. Although the implications by both these effects could be very interesting, at the moment, the insufficient statistics of observed stars prevent us from making any definitive conclusion.

---

[2] $L \approx 10^{6.2} L_\odot$, $\langle[\mathrm{Fe/H}]\rangle \approx -1.8$, see also Fig. 7.2

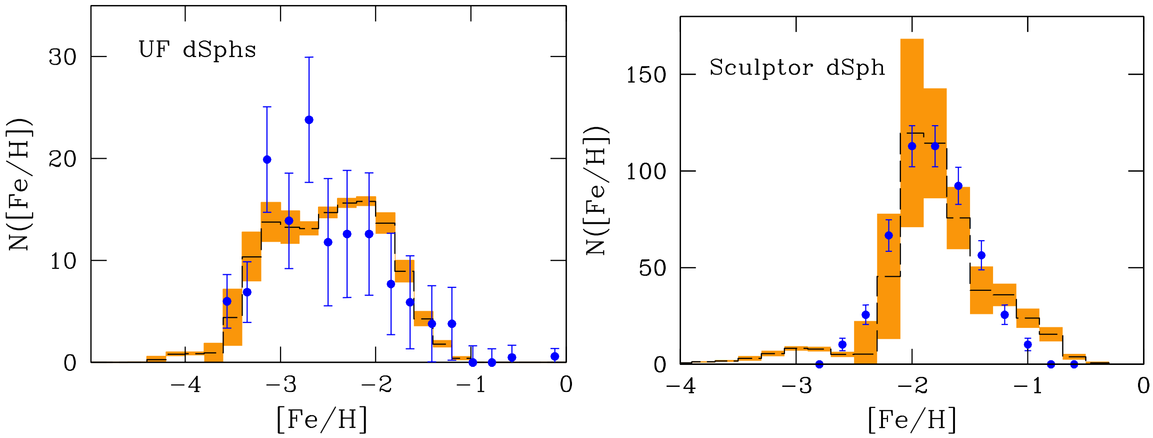

Figure 7.3: *Left panel:* comparison between the MDF of UFs observed by Kirby et al. (2007) (points) and the simulated one (histogram). Error bars are the Poissonian errors. The histogram is the averaged MDF over all UFs candidates ($L < 10^5 L_\odot$) in 10 realizations of the merger tree. The shaded area represents the 1σ scatter among different realizations. *Right panel* comparison between the Sculptor MDF observed by Helmi et al. (2006) (points), and the simulated one (histogram). Error bars are the Poissonian errors. The histogram is the averaged MDF over all the Sculptor-like dSph candidates ($10^6 L_\odot < L < 10^{6.5} L_\odot$) in 10 realizations of the merger tree. The shaded area represents the $\pm 1\sigma$ Poissonian error.

7.4 The star formation efficiency

We saw that the star formation in the faintest UFs is strongly depressed with respect to the more luminous dSphs. Two physical mechanism drive this process: the limited availability of cold, star-forming gas due to ineffective H_2 cooling, and their specific formation mechanism resulting in gas-starved systems. The mass of stars formed at $z = 0$ normalized to the cosmic baryon content associated with a halo of mass M, $\mathcal{F} = M_*/f_c M$ is shown in Fig. 7.5 as a function of M. A handy fit to the curve is given by

$$\mathcal{F} = exp(a + bx + cx^2) \tag{7.2}$$

where $a = -66$, $b = 5.97$, $c = -0.14$ and $x = ln(M/M_\odot)$. By inspecting that Figure the interplay between different factors affecting the SF can be readily understood. Haloes above $10^9 M_\odot$ convert about 10% of their potentially available $f_c M$ baryonic mass into stars; this value is solely determined by mechanical feedback. In haloes with $10^8 - 10^9 M_\odot$ gas infall starts to be quenched by shock-heating during formation by mergers, with SN feedback playing a sub-dominant role. Therefore $\mathcal{F}$ drops by about a factor 3 in this range. Finally, minihaloes $M < 10^8 M_\odot$ are affected by an additional suppression factor related to their decreasing SF efficiency (eq. 7.1) due to radiative feedback acting on the H_2 chemical network. The larger $\mathcal{F}$ scatter toward

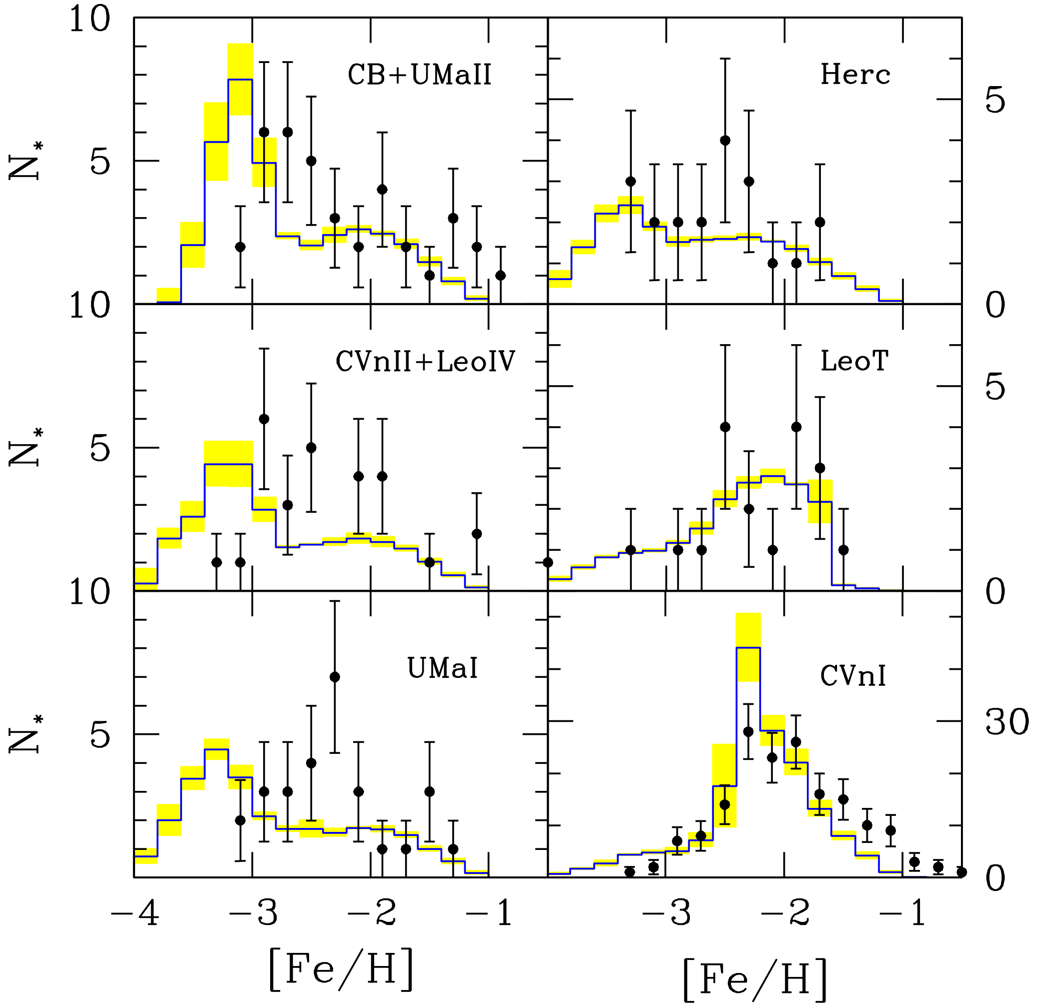

Figure 7.4: Comparison between the observed (Kirby private communication, points) and simulated (histograms) MDFs of UFs. Error bars are the Poissonian errors. The histograms are the averaged MDFs over UFs candidates in 10 realizations of the merger tree, with luminosity respectively equal to: $L_{tot} = 10^{3.6\pm0.2} L_\odot$ (CB and UMa II), $L_{tot} = 10^{3.9\pm0.2} L_\odot$ (CVn II and Leo IV), $L_{tot} = 10^{4.1\pm0.1} L_\odot$ (UMa I), $L_{tot} = 10^{4.6\pm0.1} L_\odot$ (Herc), $L_{tot} = 10^{5.1\pm0.3} L_\odot$ (Leo T), $L_{tot} = 10^{5.4\pm0.1} L_\odot$ (CVn I). The shaded area represents the 1σ scatter among different realizations.

low M is hence due to the increasing number of physical processes influencing star formation.

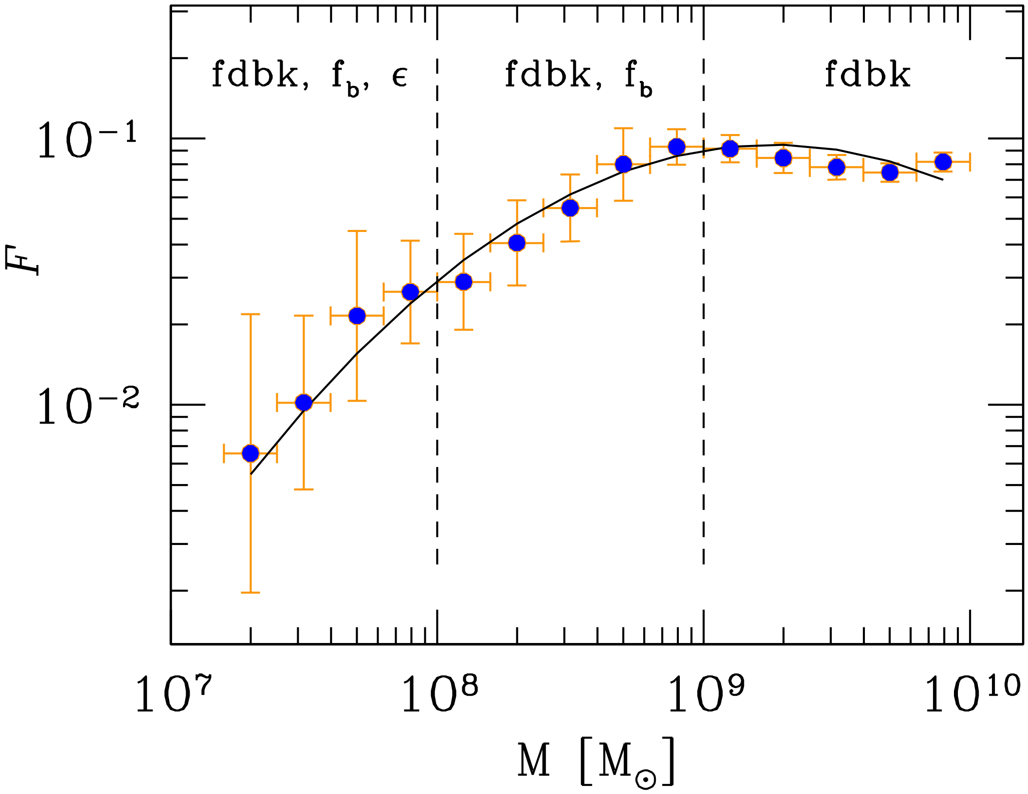

Figure 7.5: Fraction $\mathcal{F} = M_*/f_c M$ of the potentially available cosmic baryon content turned into stars as a function of M. The points are the average over all dSph candidates in 10 realizations of the merger tree. Error bars show the $\pm 1\sigma$ dispersion among different dSphs. The solid line is the handy fit.

The recent work of Madau et al. (2008) attempts to determine $\mathcal{F}$ for minihaloes by matching the luminosity function of MW satellites in the SDSS under the assumption that the formation of these systems stopped at $z_{rei} = 11$ due to reionization photoheating. They find that $\mathcal{F} = (0, 0.0025, 0.02)$ for haloes with a total mass $M = (< 3.5 \times 10^7 M_\odot, (3.5-7) \times 10^7 M_\odot, > 7 \times 10^7 M_\odot)$. In the same range of masses we find slightly higher $\mathcal{F}$ values (Fig. 7.5). However the agreement between the two studies is very good when we compare the value of $\mathcal{F}$ associated to dSphs of different magnitude M_V (Fig. 7.6). This is a consequence of the large scatter of $\mathcal{F}$ toward lower M, and it implies that at any given M_V UFs candidates in our model are hosted by more massive DM haloes than those in Madau et al. (2008); this is likely an effect of the lower reionization redshift we are assuming $z_{rei} = 6$, which allows the formation of gradually more massive haloes hosting dSphs (Fig. 7.1). In spite of this success, it is still unclear if the lower value of z_{rei} we are assuming would

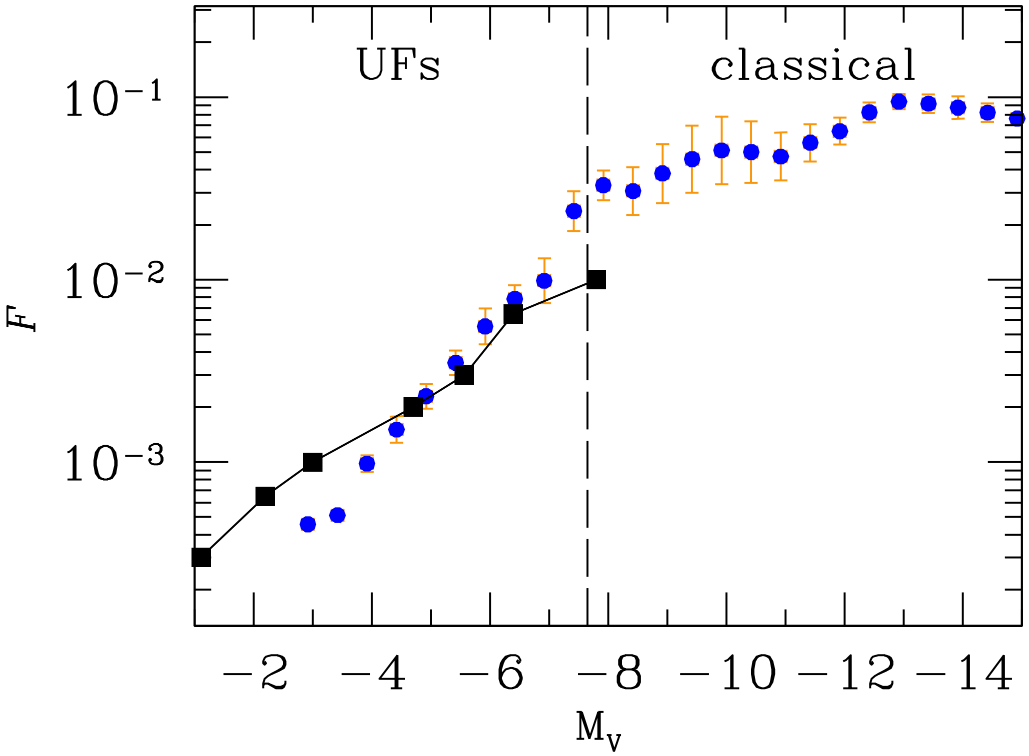

Figure 7.6: Fraction $\mathcal{F} = M_*/f_c M$ of the potentially available cosmic baryon content turned into stars as a function of M_V. The points are the average over all dSph candidates in 10 realizations of the merger tree. Error bars show the ±1σ dispersion among different dSphs. The squared points are the results by Madau et al. 2008

produce an excess of visible MW satellites; on the other hand, the effects of an early formation of UFs ($z > 12$) on the median and shape of the minihaloes/UFs MDF, have to be explored. Clearly a more comprehensive study is required to answer these questions.

7.5 Summary and discussion

We investigated the nature of UFs ($L_{tot} < 10^5 L_\odot$) by including in our semi-analytical model for the MW formation the presence of star-forming minihaloes and an heuristic prescription to account for the effects of radiative feedback. Both these ingredients are required in order to explain the existence of $L_{tot} < 10^5 L_\odot$ dSphs.

According to our results UFs are the oldest and most dark matter ($M/L > 100$) dominated dSphs in the MW system with a total mass $M = 10^{7-8} M_\odot$ and $L = 10^{3-5} L_\odot$; they are found to be left-overs of H_2-cooling minihaloes formed at $z > 8.5$, *i.e.* before reionization. Their MDF is broader (because of their more prolonged SF) and shifted toward lower [Fe/H] (as a result of a lower GM metallicity at the time of formation) with respect to classical dSphs. Our conclusions support the "primordial scenario" for the origin of dSphs proposed by Bovill & Ricotti (2008). In such a scenario feedback effects of the type discussed here represent fundamental evolutionary ingredients. The picture is strengthen by the successful simultaneous match of the Fe-L relation and the MDF of UFs. Our model reproduces at the same time also the observed MDF of both the MW and of a prototypical classical dSph as Sculptor.

The skeptic might wonder about the possible role of tidal stripping. In our picture UFs are, among all dSphs, those associated with the highest$-\sigma$ fluctuations ($\sim 2\sigma$) forming at the earliest possible epochs (Fig. 7.1). According to N-body cosmological simulations (Diemand, Madau & Moore 2005), and to our results in Chapter 4 (Fig. 4.5), this implies that UFs are most probably found at small Galactocentric radii, as indeed deduced from observations; such data however must be interpreted with care as it might be biased due to the magnitude limit of the SDSS. The proximity to the MW may cause gas/stellar loss by tidal stripping from these satellites (Mayer et al. 2007). However, it seems unlikely that UF can be the stripped remnant of classical dSph as the scaling of the luminosity-velocity dispersion with luminosity would be too steep to explain the observed trend (Peñarrubia, Navarro & McConnachie, 2008). The success of our model also lends support to the conclusion that tidal stripping plays at most a minor role.

A comparison between our results and those by Madau et al. (2008) reveals that the fraction of the potentially available baryon content turned into stars, $\mathcal{F}$, as a function of the dSph magnitude, M_V, agrees in the two studies. Hence, although our method prevents us from making specific predictions on the actual number of satellites, there is no missing satellites problem in terms of SF efficiency. It is unclear if the lower reionization redshift we have assumed would produce an excess of $z = 0$ satellites, though models claiming a good reproduction of the observed number (Bovill & Ricotti 2009, Muñoz et al. 2009) adopt different z_{rei}. On the other hand it has to be checked if an higher reionization redshift ($z_{rei} = 11$) could provide the good match of the observations we are now obtaining. Interestingly, at any given M_V, ultra faint candidates in our model are found to be hosted by more massive DM haloes than those in Madau et al. (2008); this implies that it may be possible to use the observed mass-to-light ratio of UFs in order to discriminate among the two different scenarios.

A final caveat concerns the adopted heuristic assumption for $M_{sf}(z)$. Physically $M_{sf}(z)$ is tightly related to the reionization history of the MW environment. Although we have not attempted to model in detail the radiative feedback processes determining the evolution of such quantity, which we defer to further study, it is conceivable that the grow of the LW background intensity will suppress the cooling and SF ability of progressively more massive minihaloes. Guided by this general argument we have then chosen an heuristic form of $M_{sf}(z)$ which suitably accounts for this physical process as required by the data. A more physical interpretation of its shape derived from a detailed modeling of the LW background intensity growth during reionization is nevertheless necessary; it may well unfold the complicated physics behind radiative feedback.

Chapter 8

Conclusions

In this Thesis I have discussed how it is possible to use the "stellar archeology" of the most metal-poor stars in order to explore the properties of the first stellar generations and the physical processes governing the early phases of galaxy formation. To this aim I have developed a new Monte Carlo code GAMETE (Galaxy MErger Tree & Evolution) which reconstructs the MW hierarchical merger tree and follows the stellar population and the chemical enrichment histories of the Galaxy and its dwarf satellites along the hierarchy. The elusive features of the early Universe are indirectly explored by comparing the local observations with the results of the model at $z = 0$, hence providing a self-consistent cosmological scenario simultaneously accounting for several observed properties of the MW and dSphs. In the following I will discuss the foremost results of this Thesis along with the main implications arising from them.

The impact of mechanical feedback

Mechanical feedback induced by SN energy deposition plays a crucial in driving the formation of the oldest stars in the MW system. Though the global properties of the MW (stellar/gas mass and metallicity) are well matched by using both a closed-box model and a model including mechanical feedback, *SN-driven winds are required in order to efficiently dilute metals and reproduce the wide range of [Fe/H] values characterizing halo stars.* Indeed while [Fe/H]> -1 stars form in *self-enriched* haloes, those with [Fe/H]< -2.5 form in newly virializing haloes, *accreting* gas from the *MW environment* previously enriched by earlier SN explosions. The observed Age-Metallicity relation is well matched by the model which allows us to clarify the formation mechanism of the stars populating different regions.

The Milky Way environment

The MW environment is the gas reservoir into which haloes are embedded, from which they accrete gas, and out of which they virialize. Its metal content rapidly increases with time as a result of metal ejection driven by SN explosions along the build-up of the Galaxy, hence affecting the chemical composition of the gas in the newly virializing haloes. At $z > 10$ the metallicity spread of the GM among different realizations is considerable, reflecting the large fluctuations in the hierarchical merging histories and mimicking the effects of an inhomogeneous metal mixing. We found that (i) Pop III stars dominate the GM enrichment only for $z > 9$, contributing to $< 0.4\%$ of the total mass of metals at $z = 0$; hence there is little hope to disentangle the nucleosynthetic imprint of Pop III stars among the heavy elements currently detectable in the Galactic environment; (ii) the 60% of the total mass of metals found in the GM at $z = 0$ come from haloes with $M < 6 \times 10^9 M_\odot$ implying that low-mass haloes are the dominant contributors to the cosmic metal enrichment.

The first stars

The properties of the first stars are investigated by analyzing the impact of the adopted Z_{cr} and m_{popIII} values on the simulated Galactic halo MDF, the global MW properties being independent on them. The low-Fe tail of the MDF strongly depends on the assumed parameters: the model $Z_{cr} = 10^{-4} Z_\odot$, $m_{popIII} = 200 M_\odot$ provides a very good fit to the MDF, including the sharp cutoff observed at [Fe/H]≈ -4, though it cannot account for the existence of the three UMP/HMP stars with [Fe/H]< -4.8. The latter can be accommodated by assuming $Z_{cr} < 10^{-6} Z_\odot$ but at the price of overproducing the number of stars below [Fe/H]≈ -3.5 and hence overpopulating the "metallicity desert". Conversely the current non-detection of metal free stars into the observed samples allows to robustly constrain either $Z_{cr} > 0$ and/or $m_{popIII} > 0.9 M_\odot$. We conclude that *the observed MDF cutoff strongly supports the existence of a critical metallicity,* $Z_{cr} \approx 10^{-4} Z_\odot$*, governing the transition from massive Pop III stars to normal Pop II/I stars.* However the mass of Pop III stars cannot be constrained due to a model degeneracy; indeed it is always possible to fit the observed MDF by varying m_{popIII} within the $\mathrm{SN}_{\gamma\gamma}$ mass range and Z_{cr} in its uncertainty interval. Larger stellar samples are actually required to constrain the Pop III IMF.

The second generation of stars

The Holy Graal of the various halo stellar surveys has undoubtedly been the detection of a truly metal-free star. As these objects have so far escaped detection, growing attention has been posed in the recent years on probing the nucleosynthetic patterns of extremely metal-poor stars, with the hope that these objects are born from gas polluted purely by metal-free SN. Our study shows that these *second generation stars* are no less elusive than their predecessors, having number frequencies that are so low to be zero even in the largest available sample, independently of the assumed Z_{cr} and m_{popIII} values. In the observed Galactic halo MDF only 1-2 stars (at best) could retain such metal-free nucleosynthetic imprint. Hence the small abundance scatter of halo stars observed by Cayrel et al. (2004) is naturally explained in these mature stellar populations as a result of several re-processing cycles of the gas. Unfortunately, this implies that it will be extremely difficult to infer the yields of metal-free stars by directly using the available sample.

The spatial distribution of metal-poor halo stars

The age and metallicity distribution of metal-poor stars is investigated at different Galactocentric radii by combining our semi-analytical model with N-body simulations by Scannapieco et al. (2006). Two physical processes determine the spatial distribution of stars with different metallicities: (i) the virialization epoch of the star-forming haloes and (ii) the metal enrichment history of the MW environment. The oldest stars populate the innermost region, while extremely metal-poor stars are more concentrated within $r < 60$ kpc. Beyond this radius the concentration of EMP stars is maximum in dwarf satellite galaxies, which are mostly associated to density fluctuations $< 2\sigma$. We found that *the MDF of [Fe/H]< -2 stars varies only weakly through the central 50 kpc*. Furthermore the all-radii MDF satisfactory matches the data once normalized to the number of observed stars implying that semi-analytical models, which are lacking of spatial information, can nevertheless be compared with the observations.

The quest for very metal-poor stars

Our model shows that old, [Fe/H]< -2 stars, are intrinsically rare in the Galaxy, representing only $\leq 1\%$ (*i.e.* $\approx 5 \times 10^8 M_\odot$) of the total stellar mass. This confirms that the selection of metal-poor stars is one of the major issues of the stellar surveys devoted to their investigation. The model, however, allows to identify the best region to search for such elusive stellar populations. In fact our results show that: (i) the radial distribution of $-2 <$[Fe/H]< -1 stars is very steep, following a power-law, $r^{-\gamma}$, with $\gamma = 2.2$; on the contrary (ii) VMP stars exhibit a central core for $r < r_c = 35$ kpc, closely following a β-function, $[(1 + (r/r_c)^2]^{-3\beta/2}$, with $\beta = 1$. Hence, though both populations are *more concentrated* toward the center, (iii) the relative contribution of [Fe/H]< -2 stars *increases* from 16% in the inner halo ($r < 20$ kpc) to $> 40\%$ in the outer halo. The last finding, combined with the higher concentration of VMP stars within $r < 35$ kpc, and the reduced capability of magnitude limited survey at increasing distances, allows to conclude that *the outer halo between 20 kpc $\lesssim r \lesssim 40$ kpc is the most promising region to search for very metal-poor stars.*

The puzzling origin of the ^{6}Li plateau

The production of ^{6}Li via cosmic ray spallation is investigated within our data-constrained framework for the MW formation, as a possible mechanism to provide the ^{6}Li plateau observed in metal-poor halo stars. In this scenario ^{6}Li is synthesized by the fusion reaction $\alpha + \alpha \rightarrow ^6$Li when high energy cosmic rays, accelerated by supernovae shocks along the build-up of the Galaxy, collide with the α particles residing in the MW environment. Contrary to previous findings, *neither the level* *nor the flatness of the ^{6}Li distribution can be reproduced under the most favorable conditions*. We conclude that this scenario has to be ruled-out. Similarly models involving shocks associated with structure formation to produce ^{6}Li can be excluded; indeed they require to form [Fe/H]> -3 stars when $z < 2 - 3$, while according to our results $[\mathrm{Fe/H}]_{GM} > -1.5$ at that time. More exotic scenarios involving either suitable modifications of BBN or some yet unknown production mechanism *unrelated* to cosmic SF history have to be invoked in order to solve the problem.

The dSph pre-enrichment

Motivated by the puzzling lack of [Fe/H]< -3 stars in classical dSphs (Helmi et al. 2006) we investigated the origin and evolution of these MW satellites within the cosmological framework provided by our semi-analytical model. DSph candidates are selected among newly virializing haloes corresponding to density fluctuations $< 2\sigma$, the probability of becoming satellites predicted by N-body simulations being higher for these objects. The effect of reionization photoheating on the MW environment is take into account by suppressing the formation of galaxies with circular velocity $v_c = 30$km s^{-1} after the end of reionization, fixed at $z_{rei} = 6$. Classical dSphs typically virialize at $z \sim 7$, when the MW environment has been already iron-polluted up to [Fe/H] $\gtrsim -3$. Hence *the lack of [Fe/H]< -3 stars in classical dSphs is naturally explained by the formation of these MW satellites in their natural birth environment, the Galactic medium.*

Classical dSphs

The evolution of typical Sculptor-like classical dSph of total mass $M = 1.6 \pm 0.7 M_\odot$ is investigated by following its formation in isolation (no further merging nor accretion) after the virialization epoch $z = 7.2 \pm 0.7$. The dSph evolution is strongly regulated by mechanical feedback processes causing the complete blow-away of the gas only after ~ 100 Myr from its birth. The 99% of the present-day stellar mass, $M_* = (3 \pm 0.7) \times 10^6 M_\odot$, is formed during this phase; its stellar content is therefore dominated by an ancient stellar population, > 10 Gyr old. After the blow away the galaxy remains gas-free and the SF is stopped. However fresh gas returned by evolved stars allows to re-start the SF after ~ 150 Myr and the cycle can start again. This yields an intermittent SF activity, proceeding until the present day with a rapidly decreasing rate because of the paucity of the returned gas. At $z = 0$ the dSph gas content is $M_g = (2.68 \pm 0.97) \times 10^4 M_\odot$. Such evolutionary scenario is strongly supported by the simultaneous match of several observed properties of Sculptor: (i) the metallicity distribution function; (ii) the color-magnitude diagram; (iii) the decrement of the stellar [O/Fe] for [Fe/H]> -1.5; (iv) the DM content and the mass-to-light ratio; (v) the HI mass content.

Ultra faint dSphs

The nature of UFs ($L_{tot} < 10^5 L_\odot$) is investigated by including the presence of star-forming minihaloes and an heuristic prescription to account for the effects of radiative feedback. These ingredients are fundamental in order to reproduce the observed Fe-Luminosity relation and *explain the existence of* $L_{tot} < 10^5 L_\odot$ *dSphs*. UFs are the oldest and most dark matter ($M/L > 100$) dominated dSphs in the MW system with a total mass $M = 10^{7-8} M_\odot$ and $L_{tot} = 10^{3-5} L_\odot$. They are left-overs of H_2 cooling minihaloes formed before reionization, when $z > 8.5$. Because of radiative feedback processes, strongly affecting the cooling of H_2, these systems are very ineffectively star-forming, turning into stars only $< 3\%$ of the potential available baryons.

Ultra faint vs classical dwarfs

The MDF of ultra faint dSphs is broader and more biased toward lower [Fe/H] values than that of classical dSphs, reflecting a different evolutionary pattern. The first feature is a consequence of the reduced SF activity in H_2 cooling minihaloes: UFs proceed to quietly form stars up to ~ 1 Gyr from their birth, gradually enriching the star-forming gas without the occurrence of violent blow-aways. The second feature reflects the earlier formation epoch of UFs, virializing from the MW environment when its gas metallicity was lower, but still high enough to form low-mass stars according to the critical metallicity scenario. We conclude that UFs are potentially powerful benchmark to validate this criterion, which would exclude the presence of stars with *total* metallicity below Z_{cr}. More generally, the high fraction of extremely metal-poor stars in UFs ($\approx 25\%$ of the total) along with their high formation redshift $z > 8.5$, make these galaxies the best candidates to investigate the early cosmic star formation.

Final outlook

The previous results provide a coherent physical scenario for the formation of the Milky Way and its dwarf satellite galaxies in a cosmological context. From this picture it emerges the crucial role played by feedback processes, affecting the properties of the newly forming haloes virializing out of the MW environment. The gradual enhancement of the GM metallicity driven by mechanical feedback imprints: (i) the formation of [Fe/H]< -2.5 stars; (ii) the spatial distribution of very/extremely metal-poor stars; (iii) the pre-enrichment of classical dSphs. It follows that a complete investigation of Galactic halo stars and dwarf galaxies in terms of their metal content requires a gradual enrichment of the MW environment. In our picture dSph candidates are selected in a broad redshift range $z \approx (1 - 12)$, their hosting halo mass increasing with decreasing redshifts from $M = 10^7 M_\odot$ to $M = 10^9 M_\odot$; only the most luminous and massive (Fornax-like) dSphs form the bulk of their stars when $z < 6$, the other galaxies accomplishing their formation before the end of reionization $z_{rei} = 6$. Our findings do not support the idea of a universal DM halo for dSphs but rather they suggest the existence of a minimum halo mass to form star, set by radiative feedback processes ($v_c > 10\text{km s}^{-1}$). The model is strengthened by simultaneously matching: (i) the global properties of the MW (stellar/gas mass and metallicity) and the stellar Age-Metallicity relation; (ii) the Galactic halo MDF; (iii) the Fe-Luminosity relation of dSphs; (iv) the properties of Sculptor, including the observed MDF; (v) the MDF of UFs.

Open questions

In spite of all the successes of the model there are several challenging issues that require a more in-depth study and further work. The first one has to do with our perfect mixing approximation. Our results are only marginally affected by this assumption since: (i) the stochastic nature of the hierarchical merger histories induces a GM metallicity spread similar to that found by sophisticated simulations of metal mixing in individual galaxies; (ii) at all the Galactocentric radii the MDFs by a simple inhomogeneous random mixing model are consistent with those obtained by using the perfect mixing approximation. However our assumption likely accelerates the extinction of metal-free stars. A more realistic study, accounting for the evolution of the metal bubbles produced by SN-driven winds in our N-body model, will allow to clarify this point and to robustly determine the implications for the non detection of metal-free stars *in the halo region currently explored*.

The semi-analytical model we used to investigate the nature of UFs prevents us from making specific predictions on the actual number of satellites. Although our findings agree with the results by Madau et al. (2009), which determine the SF efficiency of minihaloes by matching the luminosity function of the MW satellites in the SDSS, a crucial difference between the two models consists in the assumed redshift of reionization. Recently Alvarez et al. (2009) have used cosmological simulations in order to investigate the reionization history of MW-size galaxies. According to their results reionization in these galaxies is driven by external sources, inducing a large spread in the reionization epoch, on average equal to $\langle z_{rei} \rangle \approx 7-8$. By coupling radiative transfer codes with N-body simulations it will be possible to self-consistently follow the reionization and metal enrichment history of the MW environment, *simultaneously* investigating the impact of z_{rei} on the number of $z = 0$ satellites and on the properties of Galactic halo stars and dSphs.

A puzzling problem that cannot be explained by our model pertains to the origin of the metallicity desert and the three UMP/HMP stars, the issue being particularly challenging if the low [Fe/H] value of these stars is not a result of some peculiar nucleosynthetic history. Dust produced by Pop III stars can allow to solve the problem by *temporarily* decreasing the critical metallicity threshold to form low-mass stars (see Sec. 3.6). By implementing dust production in our semi-analytical model it will be possible to explore this solution and make predictions for the number of UMP/HMP stars in UFs. If this idea is correct, indeed, these old galaxies are expected to be the best candidates for hosting [Fe/H] $\lesssim -5$, as they virialized at

$z > 8.5$ when the GM metal enrichment was still dominated by Pop III stars.

Finally, by following the chemical evolution of different elements along the build-up of the Milky Way, it will be possible to *simultaneously* investigate several challenging questions: the origin of carbon-enhanced metal-poor stars and the Pop III IMF; the abundance patterns of metal-poor stars in the Galactic halo and in dSphs. In particular, it will be possible to make predictions for the fascinating but poorly understood Ultra Faint dwarf spheroidals.

Bibliography

Abel T., Anninos P., Norman M. L. & Zhang Y., 1998, ApJ, 508, 518

Abel T., Bryan G. L. & Norman M. L., 2000, ApJ, 540, 39

Ahn K. & Shapiro P. R., 2007, MNRAS, 375, 881

Alvarez M. A. et al. 2009, Busha M. T., Abel T. & Wechsler R. H., 2009, prepreint (ArXiv:0812.3405)

Anders E. & Grevesse N. 1989, Geochimica et Cosmochimica Acta, 53, 197.

Anninos P. & Norman M. L., 1996, ApJ, 460, 556

Aoki W., et al., 2006, ApJ, 639, 897

Aparicio A. & Gallart C., 2004, AJ, 128, 1465

Asplund M., Grevesse N., Sauval A. J., 2005, in *Cosmic Abundances as Records of Stellar Evolution and Nucleosynthesis*, Conf.Ser. 336

Asplund M., Lambert D. L., Nissen P. E., Primas, F. & Smith V. V., 2006, ApJ, 644, 229

Bardeen J. M., Bond J. R., Kaiser N. & Szalay A. S., 1986, ApJ, 304, 15

Barkana R. & Loeb A., 2001, Phys. Rep., 349, 125

Barkat Z., Rakavy G. & Sack, 1967, Phys. Rev. Lett., 18, 379

Barnes J. & Hut P., 1986, Nature, 324, 446

Battaglia G., et al., 2005, MNRAS, 364, 433

Battaglia G. et al., 2006, A&A, 459, 423

Battaglia G., 2007, Phd Thesis, University of Groningen, The Netherlands

Battaglia G. et al., 2008, ApJL, 681, L13

Battaglia G., Helmi A., Tolstoy E. & Irwin M. J., 2008b, in *The Galaxy disk in Cosmological Context*, Proceedings IAU Symposium No.254 (arXive:0807.2334v1)

Beers T. C., Preston G. W. & Schectman S. A., 1985, AJ, 90, 2089

Beers T. C., Rossi S., Norris J. E., Ryan S. G. & Shefler T., 1999, AJ, 117, 981

Beers T. C., Preston G. W. & Schectman S. A., 1992, AJ, 103, 1987

Beers T. C. et al., 2005, in *From Lithium to Uranium: Elemental Tracers of Early Cosmic Evolution*, IAUS 228, 175

Beers T. C. & Christlieb N., 2005, ARA&A, 43, 531

Beers T. C., 2009, IAU Symposium conference proceeding, 254, 461

Bertelli G., Bressan A., Chiosi C., Fagotto F. & Nasi E., 1994, A&A, 106, 275

Bertschinger E., 2001, ApJS, 137, 1

Bessell M. S., Christlieb N. & Gustafsson B., 2004, ApJ, 612, L61

Binney J., Merrifield M., 1998, *Galactic Astronomy*, Princeton Univ. Press , Princeton

Blandford R. & Eichler D., 1987, Phys. Rep., 154, 1

Bond J. R., Cole S., Efstathiou G. & Kaiser N., 1991, ApJ, 379, 440

Bond J. R., Arnett W. D. & Carr B. J., 1984, ApJ, 280, 825

Bonifacio P. et al., 2002, A&A, 390, 91

Bonifacio P., Limongi M., Chieffi A., 2003, Nature, 422, 834

Bonifacio P. et al., 2007, A&A, 462, 851

Bovill M. S. & Ricotti M., 2009, ApJ, 693, 1859

Bromm V., Ferrara A., Coppi P. S. & Larson R. B., 2001, MNRAS, 328, 969

Bromm V., Coppi P. S. & Larson R. B., 2002, ApJ, 564, 23

Bromm V., Yoshida N. & Hernquist L., 2003, ApJ, 596, L135

Bromm V. & Loeb A., 2004, New Astron., 9, 353

Brown A. G. A., Velásquez H. M. & Aguilar L. A., 2005, MNRAS, 359, 287

Bryan G. L. & Norman M., 1998, ApJ, 495, 80

Bullock J. S., Kravtsov A. V. & Weinberg D. H., 2001, ApJ, 548, 33

Buonanno R., Corsi C. E., Castellani M., Marconi G., Fusi Pecci F. & Zinn R., 1999, AJ, 118, 1671

Calura F., Menci N., 2009, preprint (ArXiv:0907.3729)

Carignan C., Beaulieu S., Cote S., Demers S. & Meteo M., 1998, ApJ, 116, 1690

Carney B. W., Laird J. B., Latham D. W. & Aguilar L. A., 1996, AJ, 112, 2

Carollo D. et al, 2007, Nature, 450, 1020

Carroll S. M., Press W. H. & Turner E. L., 1992, Rev. A&A, 30, 499

Cayrel R. et al., 1999, A&A, 343, 923

Cayrel R. et al., 2001, Nature, 409, 691

Cayrel R. et al., 2004, A&A, 416, 1117

Chiappini C. et al., 2005, Nucl. Phys. A, 758, 217

Choudury T. R. & Ferrara A., 2006, MNRAS, 371, L55

Christlieb N., et al., 2002, Nat, 419, 904

Christlieb N., Wisotzki L., Grasshoff G., 2002, A&A, 391, 397

Christlieb N., 2003, Rev. Mod. Astron., 16, 191

Christlieb N. et al., 2004, ApJ, 603, 708

Christlieb N. et al., 2008, in *First Stars III*, AIP Conference Proceedings, 990, 109

Ciardi B., Ferrara A. & Abel T., 2000, ApJ, 533, 594

Ciardi B., Ferrara A., Governato F. & Jenkins A., 2000, MNRAS, 314, 611

Ciardi B., Ferrara A., 2005, Space Sci. Rev., 116, 625

Coc A., Vangioni-Flam E., Descouvemont P., Adahchour A. & Angulo C., 2004, ApJ, 600, 544

Cohen J. G., Christlieb N., McWilliam A. & Shectman S. A., 2004, ApJ, 612, 1107

Cohen J. G., et al., 2005, ApJ, 633, L109

Cole S., Lacey C. G., Baugh C. M. & Frenk C. S., 2000, MNRAS, 319, 168

Cox T. J., Primack J., Jonsson P. & Sommerville R. S., 2004, ApJ, 607, L87

Cumberbatch D., et al., 2007, Phys. Rev., D76, 123005

Cuoco A., Iocco F., Mangano G., Miele G., Pisanti O. & Serpico P. D., 2004, International Journal of Modern Physics A, 19, 4431

Cyburt R. H., 2004, Phys. Rev. D, 70, 023505

Daigne F., Olive K. A., Silk J., Stoehr F. & Vangioni E., 2006, ApJ, 647, 773

Davis M., Efstathiou G., Frenk C. S. & White S., 1985, ApJ, 292, 371

Dehnen W. & Binney J., 1998, MNRAS, 294, 429

de Jong J. T. A. et al., 2008, ApJ, 680, 1112

De Lucia G. & Helmi A., 2008, MNRAS, 391, 14

Diemand J., Madau P. & Moore B., 2005, MNRAS, 364, 367

Dijkstra M., Haiman Z., Rees M. J. & Weinberg D. H., 2004, ApJ, 601, 666

Dolphin A. E., Weisz D.R., Skillman E.D. & Holtzman J.A., 2005, in *Resolved Stellar Populations*, ASP Conf. Ser. (arXiv:0506430)

D'Onghia E., Besla G., Cox T. J. & Hernquist L., 2009, preprint (ArXiv:0907.2442)

Evoli C., Salvadori S. & Ferrara A., 2008, MNRAS, 390, L14

Fenner Y., Gibson B. K., Gallino R. & Lugaro M., 2006, ApJ, 646, 184

Ferrara A., 1998, ApJ, 499, 17L

Ferrara A., Tolstoy E., 2000, MNRAS, 313, 291

Fields B. D. & Olive K. A., 2006, Nuc. Physics A, 777, 208

Frebel A., Christlieb N., Norris J. E., Aoki W., Asplund M., 2005, Nature, 434, 871

Frebel A. et al. 2007, ApJ, 660, L117

Frebel A., Simon J. D., Geha M. & Willman B., 2009, preprint (ArXive:0902.2395)

Freeman K. & Bland-Hawthorn J., 2002, ARA&A, 40, 487

Fryer C. L., Woosley S. E. & Heger A., 2001, ApJ, 550, 372

Fujita A., Mac Low M. M., Ferrara A. & Meiksin A., 2004, ApJ, 613, 159

Fuller T. M. & Couchman H. M. P., 2000, ApJ, 544, 6

Ganguly R., Sembach K. R., Todd T. M. & Savage B. D., 2005, ApJS, 157, 251

Geisler D., Smith V. V., Wallerstein G., Gonzales G. & Charbonnel C., 2005, AJ, 129, 1428

Geha M. et al., 2009, ApJ, 692, 1464

Gilmore G. et al. 2007, Nucl. Phys. B, 173, 15

Glover S. C. O., Brand P. W. J. L., 2001, MNRAS, 321, 385

Gnedin N. Y., 2000, ApJ, 542, 535

Gnedin N. Y. & Kravtsov A. V., 2006, ApJ, 645, 1054

Grebel E. K., Gallagher III J. S., 2004, ApJ, 610, L89

Haiman Z., Rees M. J. & Loeb A., 1996, ApJ, 467, 522

Haiman Z., Rees M. J. & Loeb A., 1997, ApJ, 476, 458

Haiman Z., Abel T. & Rees M. J., 2000, ApJ, 534, 11

Heger A. & Woosley S. E., 2002, ApJ, 567, 532

Heinbach U. & Simon M., 1995, ApJ, 441, 209

Helmi A. et al., 2006, ApJ, 651, L121

Helmi A., 2008, A&AR, 15, 145

Hernandez H. & Ferrara A., 2001, MNRAS, 324, 484

Hill V. et al., 2002, A&A, 387, 560

van den Hoek L. B. & Groenewegen M. A. T., 1997, A&A, 123, 305

Hopkins A. M., 2004, ApJ, 615, 209

Hurley-Keller D., Mateo M. & Nemec J., 1998, AJ, 115, 1840

Ibata R. A., Lewis G. F., Irwin M., Totten E. & Quinn T., 2001, ApJ, 551, 295

Ikuta C. & Arimoto N., 2002, A&A, 391, 55

Ivezic Z., et al. 2008, ApJ, 684, 287

Iwamoto N., Umeda H., Tominaga N., Nomoto K. & Maeda K., 2005, Sci, 309, 451

Jeans J. H., 1928, *Astronomy and cosmogony*, U.K., Cambridge University Press.

Jedamzik K., Choi K.-Y., Roszkowski L. & Ruiz de Austri R., 2006, JCAP, 7, 7

Johnson J. L., Greif T. H., Bromm V., 2007, ApJ, 665, 85

Jubelgas M., Springel V., Ensslin T. & Pfrommer C., 2008, A&A, 481, 33

Karlsson N., 2006, ApJ, 641, 41

Kawasaki M., Kohri K. & Moroi T., 2005, Phys. Rev. D, 71, 083502

Kawata D. & Gibson B. K., 2003a, MNRAS, 340, 908

Kawata D. & Gibson B. K., 2003b, MNRAS, 346, 135

Kawata D., Mulchaey J. S., Gibson B. K. & Sanchez-Blazquez P., 2006, ApJ, 648, 969

Kereš D., Katz N., Weinberg D. H. & Davé R., 2005, MNRAS, 363, 2

Keshet U., Waxman E., Loeb A., Springel V. & Hernquist L., 2003, ApJ, 585, 128

Kirby E. N., Simon J. D., Geha M., Guhathakurta P. & Frebel A., 2008, ApJ, 685, L43

Kitayama T., Tajiri Y., Umemura M., Susa H. & Ikeuci S., 2000, MNRAS, 315, 1

Kleyna J. T., Wilkinson M. I., Evans N. W. & Gilmore G., 2005, ApJ, 630, L141

Klimentowski J., Lokas E. L., Kazantzidis S., Mayer L. & Mamon G., 2009, MNRAS, tmp986

Knapp G. R., Kerr F. J. & Bowers P. F., 1978, AJ, 83, 360

Koch Y., et al. 2008a, AJ, 135, 1580

Koch A., et al. 2008b, ApJ, 688, L13

Komiya Y., Suda T. & Fujimoto M. Y., 2009, ApJ, 696, L79

Komiya Y., Habe A., Suda T. & Fujimoto M. Y., 2009, ApJ, 694, 1577

Koposov S. E. et al., 2009, ApJ, 696, 2179

Korn A. J. et al., 2006, Nature, 442, 657

Kravtsov A. V., Gnedin O. Y. & Klypin A. A., 2004, ApJ, 609, 482

Kravtsov A. V., 2009, preprint (ArXiv:0906.3295)

Kusakabe M., Kajino T., Boyd R. N., Yoshida T. & Mathews G. J., 2007, Phys. Rev. D, 76, 121302

Lacey C., Cole S., 1993, MNRAS, 262, 627

Lagage P. O. & Cesarsky C. J., 1983, A&A, 125, 249

Lanfranchi G. & Matteucci F., 2007, A&A, 468, 927

Larson R. B., 1974, MNRAS, 169, 229

Larson R. B., 1998, MNRAS, 301, 569

Lejeune Th., Cuisinier F. & Buser R., 1997, A&A, 125, 229

Li Y.-S., Helmi A., De Lucia G. & Felix S., 2009, MNRAS, 397, L87

Lucatello S. et al., 2006, ApJ, 652, L37

Macciò A. V. et al., 2009, pre-print (ArXiv:0903.4681)

Machacek M. E., Bryan G. & Abel T., 2001, ApJ, 548, 509

Mackey J., Bromm V. & Hernquist L., 2003, ApJ, 586, 1

Mac Low M.-M. & Ferrara A., 1999, ApJ, 513, 1421

Madau P. et al., 2008, ApJ, 689, L41

Madau P., Ferrara A. & Rees M. J., 2001, ApJ, 555, 92

Mannucci F., Della Valle M. & Panagia N., 2006, MNRAS, 370, 773

Marcolini A., Brighenti F. & D'Ercole A., 2004, MNRAS, 352, 363

Marcolini A., D'Ercole A., Battaglia G. & Gibson K. B., 2008, MNRAS, 386, 2173

Marigo P., Girardi L., Chiosi C. & Wood P. R., 2001, A&A, 371, 152

Martin C. L., Kobulniky H. A. & Heckman T. M., 2002, ApJ, 574, 663

Martin N. F., de Jong J. T. A. & Rix H.-W., 2008, ApJ, 684, 1075

Mateo M., 1994, in *Dwarf Galaxies*, eds. G. Meylan, P. Prugniel

Mateo M., 1998, ARA&A, 36, 435

Mayer L., Moore B., Quinn T., Governato F. & Stadel J., 2002, MNRAS, 336, 119

Mayer L., Mastropietro C., Wadsley J. & Stadel J., & Moore B., 2006, MNRAS, 369, 1021

Mayer L., Kazantzidis S., Mastropietro C. & Wadsley J., 2007, Nature, 445, 738

McKee C. F. & Tan J. C., 2008, pre-print (ArXiv:0711.1377)

Meneguzzi M., Audouze J. & Reeves H., 1971, A&A, 15, 337

Mercer D. J. et al., 2001, Phys. Rev. C, 63, 065805

Mets M. & Kroupa P., 2007, MNRAS, 376, 387

Meynet G., Ekström S., Maeder A., 2006, A&A, 447, 623

Mihos J. C. & Hernquist L., 1996, ApJ, 464, 641

Miniati F., Ryu D., Kang H., Jones T. W., Cen R. & Ostriker J. P., 2000, ApJ, 542, 608

Monaco L., et al. 2005, A&A, 441, 141

Montmerle T., 1977, ApJ, 216, 177

Moore B., Diemand J., Madau P., Zemp M. & Stadel J, 2006, MNRAS, 368, 563

Mori M., Ferrara A. & Madau P., 2002, ApJ, 571, 40

Mori M. & Umemura M., 2006, Nature, 440, 644

Muñoz R. R, et al. 2005, ApJ, 631, L137

Muñoz J. A, Madau P., Loeb A. & Diemand J., 2009, pre-print (ArXiv:0905.4744)

Nakamura F. & Umemura M., 2001, ApJ, 548, 19

Nakamura F. & Umemura M., 2002, ApJ, 569, 549

Navarro J. F., Frenk C. S. & White S., 1996, ApJ, 462, 563

Navarro J. F., Frenk C. S. & White S., 1997, ApJ, 490, 493

Nishi R. & Susa H., 1999, ApJ, 523, L103

Nishi R. & Tashiro M., 2000, ApJ, 537, 50

Nissen P. E, Lambert D. L., Primas F., & Smith V. V., 1999, A&A, 415, 993

Oey M. S., 2003, MNRAS, 339, 849

Oh S. P. & Haiman Z., 2002, ApJ, 569, 558

Okamoto T., Gao L. & Theuns T., 2008, MNRAS, 390, 920

Olszewski E. W., 1998, in *Galactic Halos* ed. D. Zaritsky, vol. 136 of Astronomical Society of the Pacific Conference Series

Omukai K., Nishi R., 1999, ApJ, 518, 64

Omukai K., 2000, ApJ, 534, 809

Omukai K. & Palla F., 2003, ApJ, 589, 677

Omukai K., Tsuribe T., Schneider R. & Ferrara A., 2005, ApJ, 626, 627

O'Shea B. W. & Norman M. L. 2007, ApJ, 654, 66

Padmanabhan, T., 1993, *Structure formation in the universe*, Cambridge University Press.

Peacock J. A., 1993, *Cosmological physics*, Cambridge University Press.

Peebles P. J. E., 1993, *Principles of physical cosmology*, Princeton University Press.

Peñarrubia J., Navarro J. F & McConnachie A. W., 2008, ApJ, 673, 226

Pinsonneault M. H., Steigman G., Walker T. P. & Narayanan, V. K., 2002, ApJ, 574, 398

Pont F., Zinn R., Gallart C., Hardy E. & Winnick R., 2004, ApJ, 1247, 840

Pospelov M., 2007, Phys. Rev. Lett., 98, 231301

Prantzos N., 2003, A&A, 404, 211

Prantzos N., 2006, A&A, 448, 665

Prantzos N., 2008, A&A, 489, 525

Press W. H., 2002, *Numerical recipes in C++ : the art of scientific computing.* Numerical recipes in C++ : the art of scientific computing by William H. Press. xxviii, 1,002 p. : ill. ; 26 cm. Includes bibliographical references and index. ISBN : 0521750334

Press W. H. & Schechter P., 1974, ApJ, 187, 425

Reed D. S. et al., 2005, MNRAS, 363, 393

Read J. I., Pontzen A. P. & Viel M., 2006, MNRAS, 371, 885

Revaz Y. et al., 2009, A& A, 501, 189

Ricotti M., Gnedin N. Y. & Shull J. M., 2001, ApJ, 560, 580

Ricotti M., Gnedin N. Y. & Shull J. M., 2002, ApJ, 575, 49

Ricotti, M. & Gnedin N. Y., 2005, ApJ, 629, 259

Ripamonti E., Haardt F., Ferrara A. & Colpi M., 2002, MNRAS, 334, 401

Ripamonti E., Tolstoy E., Helmi A., Battaglia G. & Abel T., 2007, *EAS Publications Series*, 24, 15

Rollinde E., Vangioni E. & Olive K., 2005, ApJ, 627, 666

Rollinde E., Vangioni E. & Olive K. A., 2006, ApJ, 651, 658

Ryan S. G. & Norris J. E., 1991, AJ, 101, 5

Ryan S. G., Norris J. E., Beers T. C., 1999, ApJ, 523, 654

Salucci P. & Burkert A., 2000, ApJ, 537, L9

Salvadori S., Schneider R. & Ferrara A., 2007, MNRAS, 381, 647

Salvadori S., Ferrara A., Schneider R., 2008, MNRAS, 386, 348

Salvadori S. & Ferrara A., 2009, MNRAS, 395, L6

Salvadori S., Ferrara A., Schneider R., Scannapieco E., Kawata D., 2009, accepted for publication in MNRAS *letter*, (ArXiv:0908.4279)

Salvaterra R., et al., 2009, preprint (ArXiv:0906.1578)

Sawala T., Scannapieco C. & White S., 2009, preprint (ArXiv:0902.1754)

Sbordone L., et al., 2007, A&A, 465, 815

Scannapieco E., Ferrara A. Broadhurst T., 2000, ApJ, 536L, 11S

Scannapieco E. et al., 2006, ApJ, 653, 285

Schneider R., Ferrara A., Natrajan P. & Omukai K., 2002, ApJ, 571, 30

Schneider R., Ferrara A., Salvaterra R., Omukai K. & Bromm V., 2003, Nature, 422, 869

Schneider R., Ferrara A., & Salvaterra R., 2004, MNRAS, 351, 1379

Schneider R., Omukai K., Inoue A. K. & Ferrara A., 2006, MNRAS, 369, 1437

Schneider R., Salvaterra R., Choudhury T. R., Ferrara A., Burigana C. & Popa L. A., 2008, MNRAS, 384, 1525

Schoerck T. et al., submitted to A&A (ArXive:0809.1172v)

Sheltrone M., Venn K., Tolstoy E., Primas F., Hill V. & Kaufer A., 2003, AJ, 125, 684

Shigeyama T., Tsujimoto T. & Yoshii Y., 2003, ApJ, 586, 57

Simon J. D. & Geha M. 2007, ApJ, 670, 313

Smecker-Hane T. A., Stetson P. B., Hesser J. E. & Lehnert M. D., 1994, AJ, 108, 507

Smith V. V., Lambert D. L. & Nissen P. E., 1993, ApJ, 408, 262

Smith V. V., Lambert D. L. & Nissen P. E., 1998, ApJ, 506, 405

Somerville R. S., Kolatt T. S., 1999, MNRAS, 305, 1

Spergel D. N., et al. 2007, ApJS, 170, 377

Spite F. & Spite M., 1982, A&A, 115, 357

Spite F., Spite M., Maillard J. P., 1984, A&A, 141, 56

Springel V., Hernquist L., 2003, MNRAS, 339, 289

Stahler W. S., Palla F., 2004, *The Formation of Stars*, WILEY-VCH Verlag Gmb & Co.KGaA, Weinheim.

Starkenburg E., Hill V., Irwin M., Battaglia G., 2008, poster contribution to GARCON08, *http://www.mpa-garching.mpg.de/mpa/conferences/garcon08/Posters/Sterkenburg.pdf*

Stetson P. B., Hesser J. E. & Smecker-Hane T. A., 1998, Astronomical Society of the Pacific, 110, 533

Stinson G. S., Dalcanton J. J., Quinn T., Kaufmann T. & Wadsley J., 2007, ApJ, 667, 170

Stoehr F., 2006, MNRAS, 365, 147

Strigari L. E. et al. 2008, Nature, 454, 1096

Strong A. W. & Moskalenko I. V., 1998, ApJ, 509, 212

Suda T., Aikawa M., Machida M. N., Fujimoto M. Y. & Iben I. Jr., 2004, ApJ, 611, 476

Sugiyama N., 1995, ApJ, 100, 281

Susa H., Umemura M., 2004, ApJ, 610, L5

Suzuki T. K. & Inoue S., 2002, ApJ, 573, 168

Tan J. C., McKee C. F., 2004, ApJ, 603, 383

Tanvir N. R., et al., 2009, preprint, (ArXiv:0906.1577)

Tassis K., Abel T., Bryan G. L. & Norman M. L., 2003, ApJ, 587, 13

Tatischeff V. & Thibaud J.-P., 2007, A&A, 469, 265

Tatischeff V., 2008, preprint (ArXiv:0804.1004)

Tegmark M., Silk J., Rees M. J., Blanchard A., Abel T. & Palla F., 1997, ApJ, 474, 1

Tinsley B. M., 1980, *Evolution of Stars and Gas in Galaxies*, Fundamentals of cosmic physics, 5, 287

Tolstoy E. et al., 2001, MNRAS, 327, 918

Tolstoy E. et al., 2004, ApJ, 617, L119

Tolstoy E. et al., 2006, The Messenger, 123, 33

Tolstoy E., Hill V. & Tosi M., 2009, preprint (ArXiv:0904.4505)

Tornatore L., Ferrara A. & Schneider R., 2007, MNRAS, 382, 945

Tsuribe T., Omukai K., 2006, ApJ, 642, L61

Tumlinson J., 2006, ApJ, 641, 1

Umeda H., Nomoto K., 2002, ApJ, 565, 385

Umeda H., Nomoto K., 2003, Nature, 422, 871

Vader J. P., 1986, ApJ, 305, 669

Valcke S., De Rijcke S., Dejonghe H., 2008, MNRAS, 389, 1111

Venn K. et al., 2004, AJ, 128, 1177

Volonteri M., Haardt F. & Madau P., 2003, ApJ, 582, 559

Wada K. & Venkatesan A., 2003, ApJ, 591, 38

Walker M. G. et al. 2006a, ApJ, 131, 2114

Walker M. G. et al. 2006b, ApJ, 642, L41

Walker M. G. et al. 2007, ApJ, 667, L53

Walsh S., Willman B., Jerjen H., 2009, AJ, 137, 450

Wilkinson M. I. et al., 2004, ApJ, 611, L21

Wilkinson M. I. et al., 2006, The Messenger, 124, 25

Wise J. H. & Abel T., 2008, ApJ, 685, 40

Wisotzki L. et al., 2000, A&A, 358, 77

Woosley S. E., Weaver T. A., 1995, ApJ, 101, 181

Yao W.-M. et al., 2006, J. Phys. G:Nucl. Phys., 33, 1

York D. G. et al., 2000, AJ, 120, 1579

Yoshida N., Abel T., Hernquist L. & Sugiyama N., 2003, ApJ, 592, 645

Yoshida N., Omukai K., Hernquist L., Abel T. 2006, ApJ, 652, 6

Zhao D. H., Mo H. J., Jing Y. P. & Börner G., 2003, MNRAS, 339, 12

Citations to previously published studies

Part of the content of this Thesis has already appeared in the following publications:

Refereed papers

S. Salvadori, R. Schneider & A. Ferrara, 2007, *Cosmic Stellar Relics in the Galactic Halo*, MNRAS, 381, 647
S. Salvadori, A. Ferrara & R. Schneider, 2008, *Life and Times of dwarf spheroidal galaxies*, MNRAS, 386, 348
C. Evoli, S. Salvadori & A. Ferrara, 2008, *The puzzling origin of the* ^{6}*Li plateau*, MNRAS, 390, L14
S. Salvadori & A. Ferrara, 2009, *Ultra faint dwarfs: probing early cosmic star formation*, MNRAS, 395, L6

Accepted papers

S. Salvadori, A. Ferrara, R. Schneider, E. Scannapieco, D. Kawata, 2009, *Mining the Galactic Halo for Very Metal-Poor Stars*, accepted for publication in MNRAS *letter*, ArXive:0908.4279

Conference proceedings

S. Salvadori, R. Schneider & A. Ferrara, 2008, *Cosmic Stellar Relics in the Galactic Halo*, in First Stars III AIP Conference Proceedings, vol. 990, pp. 459
S. Salvadori, A. Ferrara & R. Schneider, 2008, *Dwarf spheroidal evolution: global view*, in Proceedings of the International Astronomical Union, IAU Symposium, vol. 255, pp. 341

THANKS TO

My Super-Supervisor Andrea Ferrara, for the long discussions in front of the blackboard and for those in front of a Ceres; Raffaella Schneider, however present during these years of migration; all the DAVID members, so much scientist, so little scientist; Daisuke Kawata, for the beautiful figure; the astrophysics sector of SISSA, which let me meet so many stimulating people from abroad.

All the friends I run into in Trieste, which make this city so different everytime: Manu and Simo, for the unforgettable first year of dance, madness and philosophical discussions; Annalisa, Marco, Angela, Giacomo and Riccardo, for the alcoholic ARCI nights and the table football matches; Lisa, really discovered at Trst; Fabio and the psychedelic nights; Joana, for her mind; Marcos and Paco, for being so "Curros"; Valeria, Luca and Paolo, for tango, theater and mozzarella; Elena, my Tina Modotti; Stefano, which came back again; Mimmo, Tiziano and the ad-libbed nights; all my Neapolitan friends and their aggregate, for having colored my last months at Trst becoming my everyday family: Ciro, Ilenia, Mariateresa, Francesco, Enzo, Gyannet, Claudia and Goffredo; "mi primo-pischello", untiring partner of dance and adventures.

All my other friends, so far so close: Claudia, Costanza and my Cousin, for having found them again; Antonia, looking for her again; Antonella, for her wonderful lightness; Francesca, for her madness; the Spanish friends from Bruxelles, unbelievable enthusiastic; Giulia and Cristina, that make me see other possible lifes; John Tur, for keeping calling me, receiving no answers; Iacopo, for his hugs, once more so intense; Cosimo and Elena, for being so bohemienne; Erminio, for his SMS, wooden creations and irony; Cecilia, for her words, so complicate so clear; Linda, my faithful partner of imaginary trips.

My widen family, for being always there, coloured and funny. My mother and my father, for the fight, the support, the snuggle, the cynicism, the freedom, the music and the yellow.

Andrea, for his sweetness, calm and craziness; for evolving so rapidly, always surprising me.